

Feasibility study of a flexible floating solar concept as energy supply for Sleipnir during operations

Focused on the hydrodynamic behaviour

Master Thesis

Stefan Hulsbos

Feasibility study of a flexible floating solar concept as energy supply for Sleipnir during operations

Focused on the hydrodynamic behaviour

by

Stefan Hulsbos

to obtain the degree of Master of Science
at the Delft University of Technology,
to be defended publicly on Monday June 13, 2022 at 01:30 PM.

Student number:	4307801	
Thesis committee:	Dr.-Ing. S. Schreier,	TU Delft, supervisor
	Dr. ir. I. Akkerman,	TU Delft
	Dr. A. Laskari,	TU Delft
	V. Doedee MSc,	Heerema Marine Contractors
	ing. C. Dijkhuizen,	Heerema Marine Contractors

An electronic version of this thesis is available at <http://repository.tudelft.nl/>.

Preface

With a proud and huge smile, I present my graduation thesis focused on the design of a floating solar concept. It marks the end of my time at the Delft University of Technology where I developed myself both professionally and personally. From the first year where you have no clue why all these mathematics and physics actually matter, to the last year where you see how well these understandings help to think of technical challenges. Especially if you are looking into an innovative concept design of an immature technology called floating solar. Immature? Yes, since implementing floating solar into the day-to-day operations of Sleipnir is a new way for Heerema Marine Contractors (HMC) to reduce their carbon emissions.

This road to this final moment started a few years ago when I met Vincent Doedee or better known as 'Mister Sustainability'. Vincent laid out the carbon neutral roadmap for HMC where floating solar was indicated as a promising technology. He is always in for a chat about how to decarbonize the world, especially regarding technologies aimed at the maritime industry. Probably ascribed to our mutual interest for everything that floats, sails or stands in the oceanic waters.

Even though floating solar is a promising technology, this does not mean that the journey toward designing a concept was easy. Probably this is what makes engineering innovative technologies fun. There is no perfect, it is all about learning and moving closer step by step.

Guidance along the way steepens the learning curve. But I could not have finalized this without some of that guidance. I would like to thank my supervisor Sebastian Schreier for his endless support and to get me acquainted with the theory. Thanks to Cees Dijkhuizen who really helped to steer this research into a relevant direction for Heerema from a practical perspective. I would like to thank Ido Akkerman to help me zoom out from time to time to grasp the bigger picture of the research and thanks to Angeliki Laskari for the outside view during the last stage of this study. Nevertheless, huge thanks to Heerema Marine Contractors for trusting me and giving me the opportunity to dive into this interesting topic.

And last but not least, I want to thank my close family and friends for freeing their time to listen to my stories about structural theories, trends in floating solar and model tests. Many thanks for your patience.

Enjoy reading!

Abstract

The electricity demand increases globally and requires a shift toward renewable sources to prevent the exhaustion of the planet. The shipping industry is responsible for 2-3 % of the global Greenhouse Gas emissions and Heerema Marine Contractors (HMC) identified floating solar as a promising solution to reduce the emissions, of their crane vessel Sleipnir, during operations. This study is the starting point of a technical feasibility study as a temporary energy supply for Sleipnir. The design is strongly focused on the temporary deployment and limited occupied deckspace during transit. Current floating solar systems are commonly designed for permanent deployment as supporting structure for rigid glass photovoltaic (PV) panels. Furthermore, modular constructions are used to limit the transportation costs however they are not designed for temporary deployment. A new PV innovation is flexible lightweight films which allow a more flexible supporting structure. A flexible thin sheet can be spooled on a drum to make temporary deployment possible. The influence of the wave loading on the coupled hydrodynamic behaviour is evaluated since wind and current loading are predictable based on previous research.

The structural design parameters of the thin sheet and drum are designed to mimic the excitation motion since wave structure interaction has been minimized to reduce the mooring force. Therefore, the draft must be low and the characteristic length related to the bending stiffness of the sheet should be smaller than the excitation wavelength. The draft of the drum should be low to have a natural heave frequency higher than the excitation frequency.

The coupled hydrodynamic response for head loading is evaluated with model tests in a towing tank. The concept is scaled according to Froude to ensure the surface waves, which are gravity driven, are properly scaled. Regular waves are chosen based on the workability wave spectrum of Sleipnir. The roll and heave response over the frequency domain is indicated by analyzing the stable response at certain frequencies. The motions of the drum are obtained with use of object tracking based on video recordings. The force within the connection of the system was measured with a force transducer where the mooring force was measured with a newly developed 3D-sensor.

It turns out that the heave motion of the system mimics the excitation motion over the wavelengths resulting in small drift forces. Significant rotations of the drum were observed for the longer wavelengths leading to water pumping over the sheet. The overturning moment is driven by the dynamic pressure over the drum diameter and the measured force in the connection generates a counteracting moment. The connection force is proportional to the buoyancy required to submerge the sheet and the acceleration of the free-floating sheet.

The feasibility of an OFPV concept for Sleipnir is demonstrated but the rotations have to be reduced by lowering the natural roll frequency. The drum dominates the coupled hydrodynamic behaviour compared to the sheet. Either the dimensions of the drum should be lowered or the thickness of the sheet must be increased. Decreasing the drum diameter is favourable over a thicker sheet since that would increase the characteristic length. Another option is to adjust the geometry of the drum to a shape where increased water displacement is required for the roll motion.

Contents

1	Introduction	1
1.1	Heerema Marine Contractors aims to be carbon neutral	1
1.1.1	Solar energy potential	1
1.2	Potential supporting structures	2
1.3	Research focus	3
1.4	Thesis structure	5
2	Hydrodynamic behaviour of VFFS	6
2.1	Hydroelasticity	6
2.1.1	Hydroelastic dispersion relation	7
2.2	Metocean conditions	8
3	Functional description of concept	10
3.1	Flexible thin sheet	10
3.1.1	Realistic cross section	11
3.2	Drum	12
3.2.1	Design properties	13
3.3	Connection	14
4	Scaling concept to model scale	15
4.1	Construction of scale model	16
4.1.1	Influence of design parameters	17
4.1.2	Validate properties of scale model	18
4.2	Wave loading	19
5	Experimental setup	21
5.1	Properties of the setup	21
5.1.1	Mooring system	22
5.2	Data acquisition	24
5.3	Test procedure	24
5.4	Calibration	25
5.4.1	Mooring force	25
5.4.2	Connection force	27
5.4.3	Wave probes	28
6	Data processing	34
6.1	Drum motions	34
6.1.1	Object tracking	35
6.2	Measurements synchronization	37
6.3	Mooring force	43
6.3.1	Measurement validation	44
7	Results	47
7.1	Coupled hydrodynamic response	47
7.2	Mooring force	51
8	Discussion	53
8.1	Understanding the coupled hydrodynamic behaviour	54
8.1.1	Drum without the sheet	54
8.1.2	Influence of the sheet	55
8.1.3	Evaluating effects on the motions	55
8.2	Link with measurements	60

8.2.1	Wave 2	61
8.2.2	Wave 3	63
8.2.3	Wave 4	64
8.2.4	Wave 5	65
8.2.5	Manually adjusted - wave 1	66
8.3	Tuning the coupled hydrodynamic response	66
8.3.1	Connection	66
8.3.2	Moment of inertia	67
8.3.3	Mooring	67
8.3.4	Metacentric height	67
8.4	Feasibility of the designed concept	67
8.4.1	Adjusting the coupled hydrodynamic response	67
8.4.2	Interpretation of the mooring force	68
9	Conclusion	70
10	Recommendations	73
10.1	Future research	73
10.2	Model test improvements	73
10.3	The future success of OFPV	74
A	Structural evaluation during transport	78
A.1	Loading	78
A.2	Stress in the drum	78
A.3	Draft	79
A.4	Natural frequencies	80
A.4.1	Heave	80
A.4.2	Roll	80
B	Experimental determination of structural properties	81
B.1	Center of Gravity	81
B.2	Moment of inertia	81
B.2.1	Working principle experimental setup	82
B.2.2	Accuracy method	82
B.3	Moment of inertia of model scale	84
C	Calibration sensors	86
C.1	3D-sensor	86
C.1.1	Calibration setup	88
C.1.2	Calibration procedure	88
C.1.3	Accuracy	89
C.2	Connection force	90
C.2.1	Calibration setup	91
C.2.2	Accuracy	91

Introduction

International environmental agreements have been made to reduce the total environmental impact on the planet globally. The global energy mix of 2050 shows an increase in electricity demand due to electrification and a shift in supply chain toward renewable energy [13]. Therefore, energy production must rapidly increase and offshore (floating) wind and solar are seen as major contributors. World-bank predicts that by 2030, over 4000 GWp photovoltaics (PV) is installed globally, which is six times the current installed solar power worldwide [20]. Currently, floating photovoltaics (FPV) contribute for just 2.6 GWp to the energy production [35] and these systems are mainly operational at locations with mild metocean conditions such as inland waters [45]. Innovative concepts must be designed to be able to move to locations with rougher sea states and unlock the potential space located offshore [49]. However, offshore floating solar (OFPV) gains an increasing amount of interest which enhances the importance of research and development.

The shipping industry is responsible for 2-3 % of all global GHG (Greenhouse Gas) emissions. Extrapolation shows that GHG emissions double by 2050 [19]. The International Maritime Organization (IMO) initiated a strategy to reduce GHG emissions by introducing a tax on emissions. The shipping industry seems to represent only a small part of the global GHG problem. However, the fuel used in the shipping industry belongs to the most harmful of its kind by emitting CO_2 , NO_x , SO_x and particulate matter.

1.1. Heerema Marine Contractors aims to be carbon neutral

Heerema Marine Contractors (HMC) is a Dutch contractor and most notable for operating four of the largest crane vessels in the offshore industry. The objective of HMC is to be the top marine contractor by delivering sustainable value for customers and stakeholders. In 2020, HMC announced to be carbon neutral and by the end of 2020, they managed by offsetting 100 % of its existing carbon footprint by investing in carbon positive projects. New technologies are being investigated with the focus on reducing, compensating and preventing carbon emissions and by implementing various technologies, HMC aims to be completely carbon neutral within five years. SSCV Sleipnir is a semi-submersible crane vessel (SSCV) shown in Figure 1.1 and has the longest remaining lifetime (operating since 2019). Operations last on average two weeks at a more or less stationary location offshore where solar energy could be used as the electricity supply. HMC indicates floating solar as a promising option which will be evaluated in this study.

1.1.1. Solar energy potential

PV cells are made of semiconductive material which becomes conductive and converts the energy of the incoming light to electricity [39]. The efficiency - the percentage of the incoming energy converted into electricity - depends on the radiation of the incoming light and the PV properties [49]. PV can be constructed either using a crystalline (arranged) or an amorph (randomly oriented) structure. Amorph structures tend to have around 50 % lower efficiency of 100 Wp/m^2 under Standard Test Conditions (STC) compared to the efficiency of crystalline panels of 225 Wp/m^2 . Due to the limited ambient air

cooling of land-based PV, the operating temperature of the cells often doubles or triples with respect to the 25 °C in STC. The power output decreases with 0.4 % per degree centigrade for rigid crystalline panels [17] and 0.14 % for amorph PV. The yearly radiation is expressed in equivalent sun hours (ESH) which indicates the hours of radiation equal to the STC conditions. ESH ranges from 6.0 ESH daily around the equator (Gulf of Mexico) up to 2.5 ESH towards the pole (Norway) [1].

An estimation of the dimensions of the desired OFPV system help to determine the feasibility. Sleipnir requires around 250 MWh energy daily during operations. Based on a PV cell with 100 Wp/m², assuming 4 ESH daily, accounting for 20 % internal losses, show less than one square kilometer suffices for the energy supply of Sleipnir according to Equation 1.1. Equal to 40 times Sleipnir its own horizontal surface (200 m · 100 m) which is challenging but not unrealistic.

$$A = \frac{250 \times 10^6 \text{ Wh}}{100 \text{ W} \cdot 4 \text{ ESH} \cdot 0.8} \approx 900 \text{ m} \cdot 900 \text{ m} \quad (1.1)$$



Figure 1.1: Impression of SSCV Sleipnir owned by HMC

1.2. Potential supporting structures

To make a floating solar design, the first step is to create a supporting structure for PV cells on the water surface. Most operating systems are designed based on PV glass panels and therefore require a rigid supporting platform. Common systems designed for inland waters consist of single (Figure 1.2a) or multiple interlinked rigid floaters (Figure 1.2b) with a corresponding supporting frame on top [9]. Considering various supporting structures, Oceans of Energy reduced the structural height by connecting modular rigid plates with panels on top aimed for offshore application (Figure 1.2c). The systems of SolarDuck (Figure 1.3a) and Moss Maritime create an air gap between the supporting frame and water surface with several floaters (height to width ratio » 1) per module [11]. The area subjected to the free water surface is lowered to reduce the wave structure interaction. Ocean Sun pilots with a thin flexible membrane under tension due to the rigid circular enclosure (Figure 1.3b). All systems discussed above are designed for permanent deployment and modular construction is used to limit transportation costs. HMC requires an OFPV system for Sleipnir focused on temporary deployment with limited deckspace occupied during transit. The current OFPV systems, as mentioned above, are deemed unfit for HMC to embed in their day-to-day operations based on these requirements.

New innovations in PV technology make flexible lightweight solutions possible, demonstrated by the flexible thin film of HyET Solar. The thin film of HyET Solar is just 0.5 mm thin and has a mass of 0.7 kg/m², however the efficiency is lower (100 Wp/m²) than average conventional glass panels (225 Wp/m²). The thin film of HyET Solar is designed for curvatures up to a radius of 0.15 m and therefore allows a flexible supporting structure. The Joint Industry Project (JIP) Solar@Sea II designed an inflatable mattress as supporting structure based on the thin film PV of HyET (Figure 1.3c) [3].



Figure 1.2: Visualization of operation FPV systems

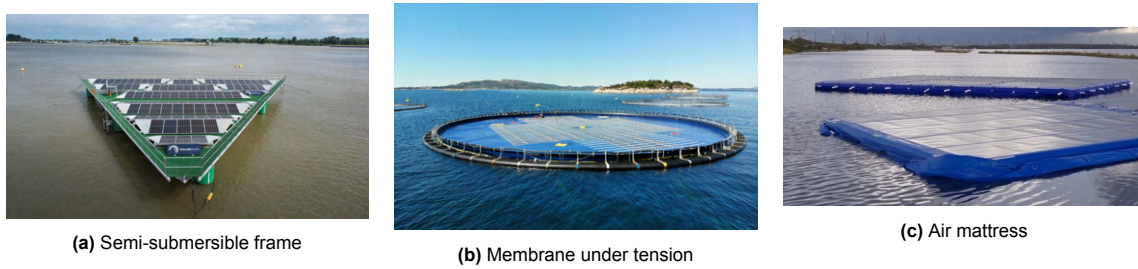


Figure 1.3: Visualization of operation OFPV systems

Using an inflatable mattress could be a disadvantage for HMC since one of the requirements considered is to use limited deckspace, this will therefore require deflating the system every time when the operations offshore are finalized. Hence, a thin sheet made of a flexible material could be an interesting option for HMC. Another design idea could be to spool a flexible sheet on a drum, this could timewise be easier to deploy and retract than an inflatable mattress as a supporting structure. However, either an inflatable mattress or a thin sheet is characterized as a flexible structure and due to the large horizontal dimensions compared to the height both are classified as Very Flexible Floating Structures (VFFS). The bending stiffness of both options can be adjusted either by varying the pressure of the air mattress or the composition of the thin sheet cross section. The overall idea of the floating solar design for Sleipnir is to deploy the structure next to Sleipnir as shown in Figure 1.4. The generated energy is transferred from the OFPV system via an umbilical to Sleipnir.

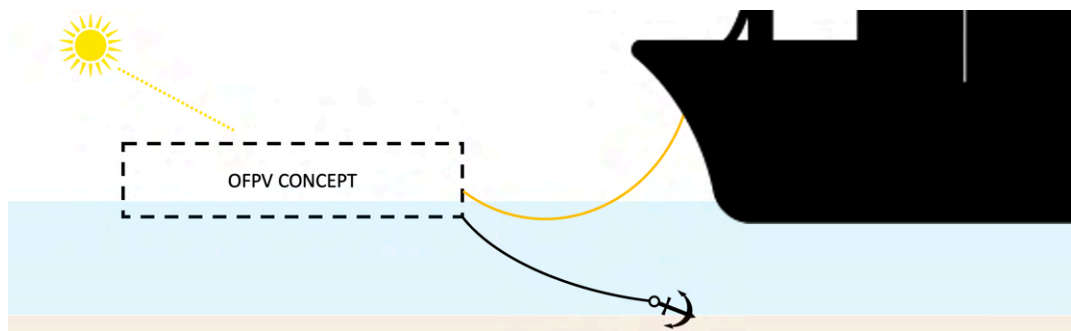


Figure 1.4: Visualization of the concept idea where the orange line represents the umbilical for energy transfer to Sleipnir.

1.3. Research focus

This starting point of this technical feasibility study is the question from HMC about how OFPV could be realized for Sleipnir. The research focuses mainly on temporary deployment which therefore requires a relatively simple mooring system and hence the aim should be to limit the mooring forces. This requires a system that is expected to mimic the wave motions instead of strong interference with the waves. The capabilities of Sleipnir should be minimally affected and therefore as already mentioned above,

the requirement from HMC is to use limited deckspace of the OFPV system during transit. Conversely, the area subjected to direct sunlight of the OFPV system during deployment should be maximized. As mentioned above, spooling the flexible supporting structure on a drum could be a convenient option for temporary deployment. For this feasibility study, the concept consists of a flexible thin sheet and a drum, where the connection between the flexible sheet and the drum is still unknown. A more elaborated idea of the design of the concept for HMC is shown in 1.5. As shown in the Figure below, the OFPV concept has its own mooring system and transfers the generated energy via an umbilical to the Sleipnir.

The gap within this study is the coupled hydrodynamic interaction between a rigid and a flexible structure, where the drum is classified as a rigid structure and the sheet stands for the flexible structure. The drum itself can be described by extensively researched rigid body dynamics, however, flexible structures are relatively new and therefore less researched. To be able to determine the feasibility of OFPV for HMC, the influence of the motions regarding the drum on the thin sheet response have to be understood and therefore be researched. The structural properties of both elements should be discussed in relation to the hydrodynamic behaviour. Eventually, the hydrodynamic response of the concept will be evaluated while taking the operating metocean conditions of Sleipnir into consideration.

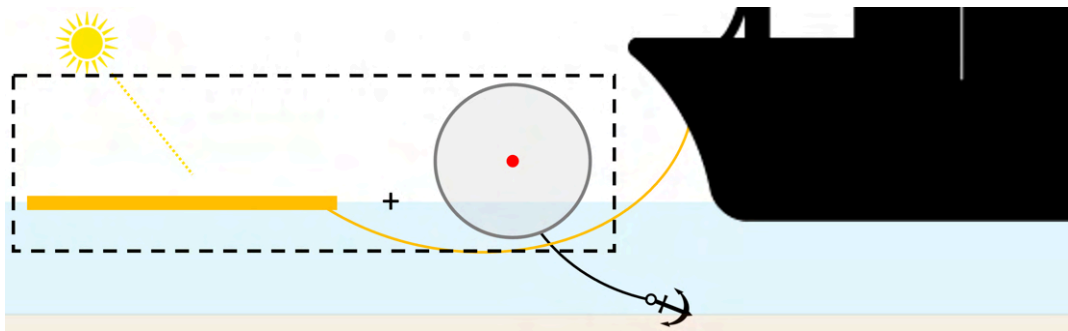


Figure 1.5: The elaborated concept consists of a flexible sheet (orange rectangle) and a drum (gray). How these are connected, is still unknown and schematized as +.)

Hence, the research goal can be summarized as,

a feasibility study of a flexible floating solar concept as energy supply for Sleipnir during operations focused on the hydrodynamic behaviour.

This research goal is divided into the following objectives:

- *The influence of the structural design parameters of both elements (drum and sheet) separately;*
- *The coupled hydrodynamic response by connecting the drum and the sheet;*
- *The mooring forces of the coupled system.*

The concept is subjected to wind, current and wave loading during deployment as schematized in Figure 1.6. The current and wind velocity results in a skin friction force F_{skin} proportional to the horizontal dimensions of the structure and can be approximated with empirical formulas as shown in [18]. The coupled motions of the system lead to a negligible change in the horizontal structural area and therefore negligible change in F_{skin} . Wind loading results in a lift force F_{lift} which is proportional to the horizontal dimensions of the structure and a drag force $F_{drag} \sim 2$ which is related to the structural area perpendicular to the wind direction. The lift force can be approximated with empirical formulas as shown in [18]. The drag contribution is strongly dependent on the deflection of the sheet due to the wave excitation and can be approximated with simulations as shown by Trapani [46]. The inertia $F_{inertia}$ and drag force F_{drag} on the drum can be obtained using the Morison equation related to the velocities and structural area perpendicular to the loading. The (unknown) drum motions will have negligible influence on the magnitude of these forces due to wind and current. The drag force due to wave loading depends on the structural design which influences the coupled hydrodynamic response to waves. Therefore, this study focuses on the influence of wave loading of the system consisting of a rigid drum and a flexible sheet, focused on coupled hydrodynamic behaviour.

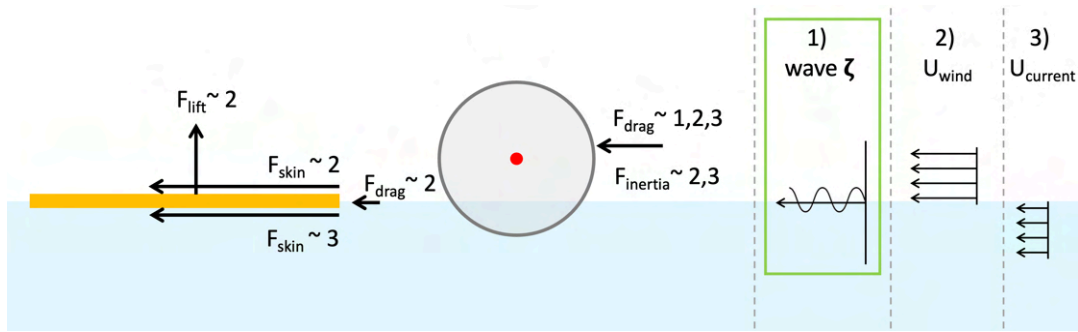


Figure 1.6: Free body diagram of the forces on the thin sheet (orange) and drum (gray) due to the loading of the waves (1), wind (2) and current (3).

To determine the influence of wave loading, either a numeric or experimental approach could be chosen. Generally, structural parameters are easily adjustable for a numeric model compared to model tests and the contradictory holds for adjusting the wave loading. A numeric model requires to solve the coupled problem of the structural properties as well as the fluid loading. Available Computational Fluid Dynamics (CFD) software solves those problems for rigid structures and (complex) fluid loading. For this study, a new numeric model could be constructed to reflect the flexible structural properties [41]. Several methods described [51, 30, 23] are available to solve the coupled fluid structure problem numerically. Each with its own advantages and disadvantages related to included effects and efficiency (computational time) as evaluated in [6, 40, 50, 43]. There is always a trade-off regarding which effects will be or will not be included in the numeric model (for example added mass, different types of damping and structural nonlinearities) and the important effects are hard to determine at this stage since the coupled behaviour is unknown. When comparing numeric modeling to experimental testing, the advantage seems to be that for model testing, it is not required to choose certain effects upfront since all effects will be taken into consideration. However, the right scaling should be chosen to reflect the desired effects, gravity forces are scaled well according to Froude whereas scaling of viscous effects is obtained using Reynolds [22]. Froude scaling is a convenient choice if the hydrodynamic response due to gravity-driven surface waves is of interest. Therefore, experimental testing is a suitable first step to evaluate the feasibility of this concept for HMC and meanwhile determine the governing effects. Thereafter, a numerical model with the emphasis on the governing effects following the model tests is a reasonable next step to vary certain structural parameters to optimize the concept.

1.4. Thesis structure

The build-up of this study is shown below.

- Chapter 1: States the relevance of this research and introduces the concept.
- Chapter 2: Discusses relevant theory related to the hydrodynamic behaviour of the concept.
- Chapter 3: Discusses reasonable structural properties of the concept design to obtain the desired hydrodynamic behaviour.
- Chapter 4: Evaluate the scaling from the full scale properties to model scale.
- Chapter 5: Description of the used experimental setup in the towing tank.
- Chapter 6: Shows how the data is gathered and processed by, among other things, the use of object tracking.
- Chapter 7 + 8: States the results and the discussion of the results.
- Chapter 9 + 10: Drawn up the conclusion and recommendations of this feasibility study.

2

Hydrodynamic behaviour of VLFS

Within this chapter, the hydrodynamic behaviour of Very Large Floating Structures (VLFS) will be discussed and the conditions of the operating spectrum of Sleipnir are taken into consideration. Wave loading results in a first-order force that is similar to the wave frequency and wave loading also results in a slowly varying second-order drift force [6]. Research has been performed in predicting the mooring loads of VLFS by the use of numerical simulations based on the wave-induced pressure on VLFS [51]. The drift force contributes in the horizontal direction to the mooring force and is proportional to the reflected wave amplitude ζ_r [18].

The formula derived by Maruo stated in Equation 2.1 is an often used indication of the drift force, where improved accuracy can be obtained with the methods derived by Newman, Namba, and Shimada [24]. The Maruo formula is slightly adapted to model tests [28] by estimating C_{wd} for rectangular shapes (between 0.8 and 1.0 dependent on the excitation wavelength λ).

$$F_{drift} = \frac{1}{2} \rho_w g C_{wd} \zeta_r^2 L B \quad (2.1)$$

$\rho_w, g, C_{wd}, \zeta_r, L, B$ represent the water density (kg/m^3), gravitational constant (m/s^2), the shape factor (-), the reflected wave height (m), structural length (m) and width (m). The amount of reflected energy is proportional to the hydrodynamic response of a structure which is discussed in Section 2.1.

2.1. Hydroelasticity

A floating structure can respond either as a rigid body or in an elastic way (deflecting locally) to wave loading. The motion response of the structure depends on the excitation load, structural dimensions and properties [41]. The characteristic length λ_c (m) stated in Equation 2.2 introduced by Suzuki and Yoshida [42] for a 2D-beam helps to distinguish between the two responses,

$$\lambda_c = 2\pi \left(\frac{EI}{\rho_w g B} \right)^{\frac{1}{4}} \quad (2.2)$$

where E represents the Young's Modulus (N/m^2), I the moment of inertia of the cross section (m^2) and h the structural height (m). The characteristic length λ_c describes the influence zone of a static concentrated load where deflections occur for a 2D beam, visualized in Figure 2.1.

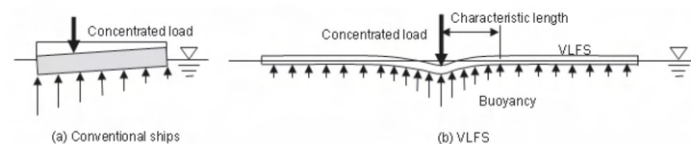


Figure 2.1: Visualization of the characteristic length [41]

VLFS are characterized by the large horizontal dimensions compared to the structural height and excitation wavelength λ . Therefore, the structural properties of VLFS are approximated by an elastic plate [8] with bending stiffness indicated according to Equation 2.3,

$$D = \frac{Eh^3}{12(1-\nu^2)} \quad (2.3)$$

where ν represents the Poisson's ratio of the material (-). The characteristic length stated in Equation 2.2 should be adjusted for a 3D structure by replacing the bending stiffness per structure length $\frac{EI}{B}$ for D resulting in Equation 2.4. The characteristic length combined with the excitation wavelength λ and structural length L determines the response type as shown in Figure 2.2 [41]. Figure 2.2 can be extended to include Very Flexible Floating Structures (VFFS) structures which entirely mimic the excitation wave loading for $\frac{L}{\lambda_c} \gg 1$ and $\frac{L}{\lambda} \gg 1$.

$$\lambda_c = 2\pi \left(\frac{D}{\rho_w g} \right)^{\frac{1}{4}} \quad (2.4)$$

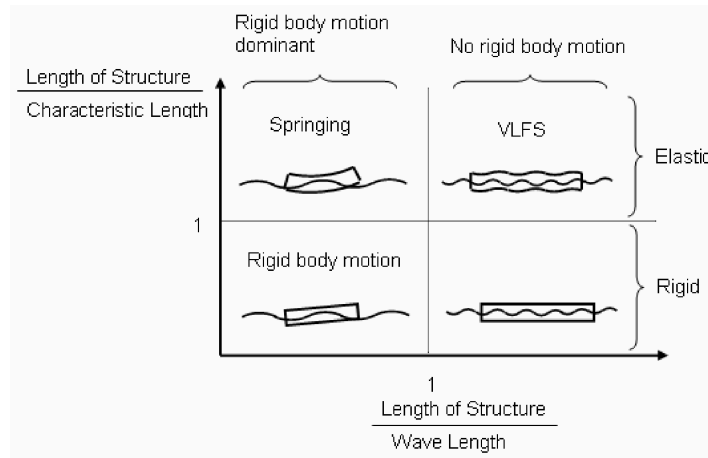


Figure 2.2: Indicating the expected response of floating structures [41]

2.1.1. Hydroelastic dispersion relation

VFFS experiments performed by Schreier and Jacobi [37] show deviation in amplitude along the structure centerline for wavelengths approaching λ_c . This observation is explained by the balance of energy over the structure. The wave energy E (J/m^2) per perpendicular area to the excitation direction consists of a kinetic K and a potential energy P part as shown in Equation 2.5. K is derived based on the velocity in both directions and P are driven by the wave elevation ζ_a above mean water level $z = 0$ [16].

$$E = K + P = \frac{1}{4}\rho g\zeta_a^2 + \frac{1}{4}\rho g\zeta_a^2 = \frac{1}{2}\rho g\zeta_a^2 \quad (2.5)$$

The energy flux P ($\text{J}/(\text{m}^2 \text{ s})$) states the rate of energy transfer per unit perpendicular area shown in Equation 2.6, derived based on the average work done over one wave period [22]. The group velocity c_g (m/s) represents the velocity at which the energy of the entire wave train propagates and the phase velocity c (m/s) states the velocity of one single wave within the wave train.

$$P = E \cdot \frac{c}{2} \left(1 + \frac{2kh}{\sinh(2kh)} \right) = E \cdot c_g \quad (2.6)$$

If energy dissipation and energy transfer from the wave to the structure are negligible, the energy flux should remain equal while the wave propagates along the structure: $\frac{\delta P}{\delta x} = 0$ [22]. Hence, the observed decrease in amplitude ζ_a translates to a decrease in energy density over the wavelength E which requires an increase in phase velocity c in order to satisfy the constant energy flux. The wave period T (s) remains constant over time and therefore the increase in c translates to an increase in

wavelength according to $c = \frac{\lambda}{T}$. This finding of Schreier and Jacobi [37] is in line with the hydroelastic dispersion relation found by Tsubogo in [47] and is widely applied for VLFS (relatively stiff compared to VFFS). The hydroelastic dispersion relation stated in Equation 2.7 is derived by solving potential theory with an adjusted boundary condition at the free surface while incorporating the properties of the flexible plate.

$$\frac{\omega^2}{g} = kQ \tanh(kh) \quad (2.7)$$

$$Q = 1 + \left(\frac{k}{k_p}\right)^4 - \left(\frac{\omega}{\omega_0}\right)^2$$

$$k_p = \left(\frac{\rho_w g B}{EI}\right)^{\frac{1}{4}}, \quad \omega_0 = \sqrt{\frac{g}{d_0}}$$

The magnitude of both terms related to the properties of the excitation wave ($k = \frac{2\pi}{\lambda}$ and ω) determine the hydroelastic transfer factor Q to the general dispersion relation stated in Equation 2.1.1. k_p can be rewritten with the use of the discussed characteristic wavelength λ_c for a flexible plate as shown in Equation 2.8. This term is influenced by the bending stiffness of the structure D . The dry natural frequency of the structure ω_0 (neglecting added mass) is influenced by the structural mass m via the initial draft $d_0 = \frac{m}{\rho_w B L}$ and shifts towards the lower frequencies with increasing mass as shown in Equation 2.8. The influence of the hydroelastic transfer function Q , to the wavelength λ , is clearly visible in the rewritten form of the hydroelastic dispersion relation stated in Equation 2.9.

$$k_p = \left(\frac{\rho_w g}{D}\right)^{\frac{1}{4}} = \frac{2\pi}{\lambda_c}, \quad \omega_0 = \sqrt{\frac{\rho_w g B L}{m}} \quad (2.8)$$

$$\lambda = \frac{g T^2}{2\pi} Q \quad (2.9)$$

$$Q = 1 + \left(\frac{\lambda_c}{\lambda}\right)^4 - \frac{\omega^2 m}{\rho_w g B L}$$

The flexural rigidity and draft can be determined during the design process and relate to the response of the wave loading. The expected wave loading is assessed in the next Section to determine the influence on the hydrodynamic response in relation to characteristic length.

2.2. Metocean conditions

A sea state characterized by its irregularity can be described by a superposition of multiple regular waves leading to a so-called spectrum [4]. This is important to take into consideration since the Sleipnir mostly operates at diverse locations around the world where the expected metocean conditions are described with a wave spectrum, which describes the energy distribution over the frequency range. Wind-generated waves are heavily dependent on the fetch length, the parameter γ accounts for the stage of development of a sea. Fully developed seas (theoretical unlimited fetch) are described by a Pierson Moskowitz spectrum whereas young seas are well modeled by a JONSWAP spectrum (North Sea locations for example). The more mature a sea gets, the more equally the energy distribution spreads over the frequencies (peakness factor $\gamma = 1$). A mean JONSWAP wave spectrum for limited fetch described in Equation 2.10 is generally used for offshore engineering with $\gamma = 3.3$. A reliable wave spectrum for a location can be generated based on the significant wave height H_s (m) and peak period T_p (m) [22]. With increasing peak periods the energy peak shifts to the lower frequencies as shown in Figure 2.3.

$$S_\zeta(\omega) = \frac{320 \cdot H_s^2}{T_p^4} \cdot \omega^{-5} \cdot \exp\left\{\frac{-1950}{T_p^4} \cdot \omega^{-4}\right\} \cdot \gamma^{\exp\left\{-\left(\frac{\omega}{\omega_p} - 1\right)^2\right\}}, \quad \text{with } \sigma = \begin{cases} 0.07 & \omega < \omega_p \\ 0.09 & \omega > \omega_p \end{cases} \quad (2.10)$$

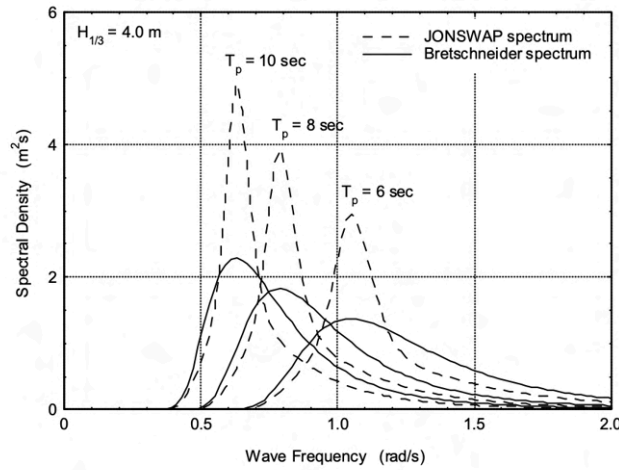


Figure 2.3: Influence of T_p on energy distribution [22]

HMC uses an empirical formula based on the significant wave height and peak period to get an indication of the workability of Sleipnir as shown in Equation 2.11.

$$H_s \cdot T_p^2 < 250 - 300 \tag{2.11}$$

Based on the wave scatter diagrams presented in [14] the lower limit spectrum is determined for worldwide conditions by $T_p = 3.5$ s, $H_s = 0.5$ m. A reasonable spectrum with maximum peak period satisfying the condition of HMC stated in Equation 2.11 is described by $T_p = 10.5$ s, $H_s = 2.5$ m. In Figure 2.4 the spectral density based on JONSWAP stated in Equation 2.10 is plotted for both outer cases and two reasonable spectra in between, to give an indication of the energy distribution over the frequencies. Wave frequencies between $\omega = 0.4$ rad/s and $\omega = 1.9$ rad/s may be expected within the operational spectrum of Sleipnir. These frequencies translate to a wavelengths of 17 m – 385 m with use of the dispersion relation (Equation 2.7 with $Q=1$).

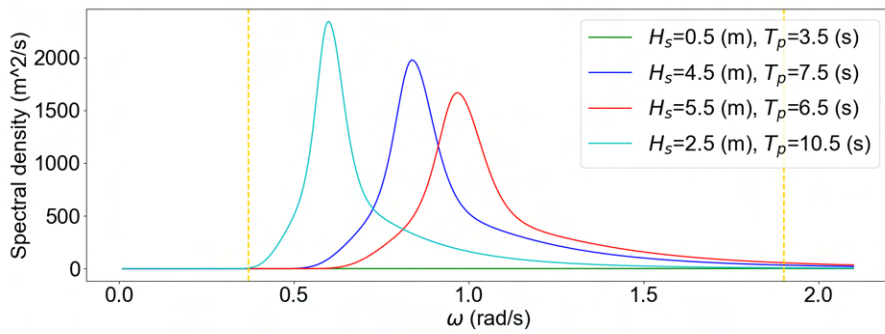


Figure 2.4: Spectral density of reasonable spectra within the workability range of Sleipnir stated by Equation 2.11. The vertical orange lines indicate the boundaries of the expected excitation frequency range.

3

Functional description of concept

An OFPV concept design for Sleipnir consists of a thin flexible sheet as a supporting structure for the HyET PV linked via a yet-to-defined connection to the drum. To be more precise, the thin flexible sheet is connected via an umbilical to Sleipnir to be able to transfer the generated electricity, while the drum has its own mooring system. All three components are discussed in this chapter to determine a reasonable concept.

3.1. Flexible thin sheet

The draft and bending stiffness of the floating structure determine the influence on the excitation wave properties. Both parameters are correlated since they both follow the cross section design. The influence of adjusting the structural height h will be discussed before a reasonable cross section is determined.

Wave shortening occurs if $(\frac{\omega}{\omega_0})^2 > (\frac{\lambda_c}{\lambda})^4$ and wave stretching appear for the opposite relation. Elastomers are suitable materials to construct the thin sheet characterized by a low density and low Young's Modulus E . For instance, the density of open foam is around 40 kg/m^3 and $E = 1 \text{ MPa}$. Subsequently, The sheet thickness h can be freely chosen and relates to the bending stiffness of the structure. The magnitude of both terms to the transfer factor Q are visualized for four structural heights over the wave frequencies in Figure 3.1 ($h = 0.05, 0.30, 0.50, 0.80 \text{ m}$), assuming an uniform cross section which is made of open foam.

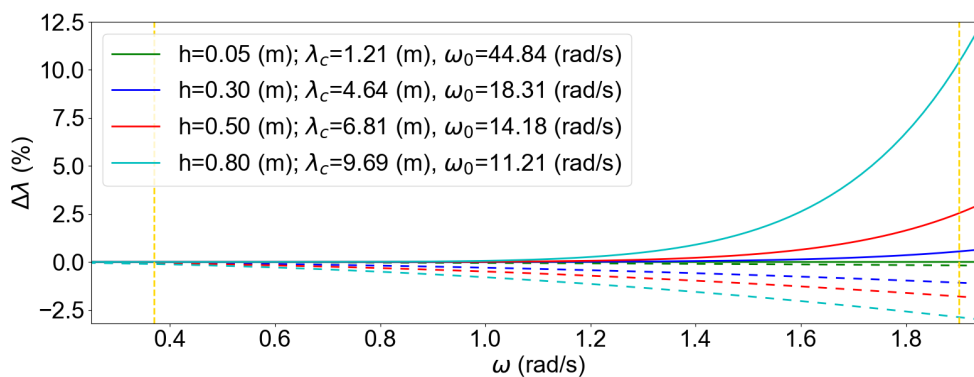


Figure 3.1: Magnitude of the hydroelastic terms stated in Equation 2.7 for four thicknesses of the sheet. The continuous line represents $(\frac{\lambda_c}{\lambda})^4$ and the dashed line represents $(\frac{\omega}{\omega_0})^2$. The orange dashed vertical lines bound the interval of expected wave frequencies during operations.

The term related to the bending stiffness $\frac{\lambda_c}{\lambda}$ becomes dominant at the higher wave frequencies while wave stretching is expected to arise as shown in Figure 3.1. However, little energy exists at

these frequencies as shown in Figure 2.4 and the absolute wave stretching will be small as a consequence of the short wavelengths. Furthermore, the characteristic length approaches the wavelength with increasing structural height and therefore the ratio $\frac{\lambda_c}{\lambda} \ll 1$ to limit the stiffness term to transfer factor Q . Up to $\omega = 1.4$ rad/s the term of Q related to the draft is slightly bigger than the stiffness term, nonetheless, the combined influence is within 1%. Notwithstanding, all considered thicknesses result in very low flexural rigidities compared to common VLFS applications [?] and therefore negligible wave structure interaction is expected. To give an example, a steel sandwich structure of $h = 0.50$ m with $D = 2.6 \times 10^9$ Nm does barely deflect as response to the excitation wave (motivated with $\lambda_c \approx 142$ m) since Q goes to infinity beyond $\omega = 0.7$ rad/s.

3.1.1. Realistic cross section

HyET foil is chosen as the conductive PV layer for the OFPV design. Elastomers are characterized by its large strain behaviour although the HyET PV foil mounted on top is incapable of handling those strains. A (stiff) substrate between the supporting structure and therefore PV foil is used to shift the neutral axis of the cross section towards the stiffer materials and reduce the strain in the PV foil due to bending [34]. Hence, the shear stress is neglected since the layers are assumed to be connected stiffly [32]. Accordingly, Kirchoff-Love theory for thin plates (neglecting shear effects) stated in Equation 3.1 may be used to determine the flexural rigidity D of a cross section consisting of n layers [44].

$$D = \frac{1}{3} \sum_{k=1}^n e_k (\tilde{z}_k^3 - \tilde{z}_{k-1}^3); \quad a = \frac{1}{2} \sum_{k=1}^n e_k (z_k^2 - z_{k-1}^2) \left(\sum_{k=1}^n e_k h_k \right)^{-1} \quad (3.1)$$

$$z_0 = 0, \quad z_k = \sum_{i=1}^k h_i, \quad k = 1, \dots, n, \quad e_k = \frac{E_k}{1 - \nu_k^2}, \quad \tilde{z}_k = z_k - a$$

where a represents the height of the neutral axis above $z = 0$ (bottom cross section), h the layer thickness, E the material Young's modulus and z the vertical midplane distance of a layer k .

As stated in Chapter 2, the hydrodynamic response is characterized by the draft and bending stiffness of the supporting structure. A variety of configurations are possible for the cross section design to end up with a characteristic length satisfying $\frac{\lambda_c}{\lambda} \ll 1$. The low draft of VFFS is automatically obtained by using low-density materials for building up the cross section. The supporting structure should be able to withstand a load of a walking person and the mass of the HyET PV of 0.7 kg/m². The person load is schematized by $m_{person} = 90$ kg transferred by the contact area of the feet approximated as two circles with area $A_{feet} = (\pi \cdot (0.25 \text{ m})^2)$ to the thin sheet. The difference in density between the foam ρ_{foam} and water ρ_w combined with the structural height h determines the bearing capacity per horizontal area (HyET PV mass negligible compared to m_{person}).

$$h = \frac{\frac{1}{2} \cdot m_{person}}{A_{feet} \cdot (\rho_w - \rho_{foam})} = \frac{45 \text{ kg}}{(\pi \cdot 0.25 \text{ m}^2) \cdot (1025 - 40 \text{ kg/m}^3)} \approx 0.23 \text{ m} \quad (3.2)$$

A reasonable supporting structure designed during this research is composed of a core consisting of open-cell foam, sealed at the bottom by 5 mm closed-cell neoprene, to prevent fluid from draining into the pores of the foam. Furthermore, a thin layer of steel as substrate is added to reduce the strains in PV. The 0.5 mm HyET PV is constructed of three layers: Polyethylene terephthalate (PET), Fluorinated Ethylene Propylene (FEP) and steel. The cross section is visualized in Figure 3.2 and the material properties are listed in Table 3.1.

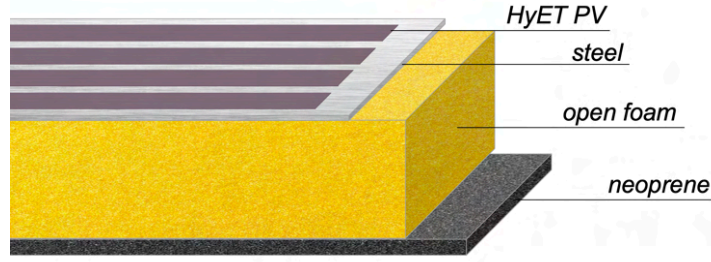


Figure 3.2: Visualization of the thin sheet cross section composed of different layers

		ρ (kg/m ³)	E (MPa)	ν (-)	σ_{yield} (N/mm ²)	h_k (mm)
HyET PV	FEP	100	600	0.44	23	0.2
	steel	7850	210000	0.3	235	0.004
	PET	135	3150	0.43	55	0.2
Substrate	steel	7850	210000	0.3	235	0.5
	foam	40	0.93	0.5	0.7	230
Core	neoprene	1350	2.5	0.5	10	5

Table 3.1: Properties of used materials for the thin sheet cross section chosen for this study

The chosen composition of the cross section results in a structural height $h = 0.2359$ m and a flexural rigidity $D = 5940$ Nm according to Equation 3.1, where the neutral axis lays within the steel substrate at $z = 0.2349$ m. The mass of 20.57 kg/m² leads to a draft $d = 0.020$ m, which is 8% of the structural height. The thin sheet is expected to mimic the wave motions as a result of the high natural frequency $\omega_0 = 20.54$ rad/s and the characteristic length $\lambda_c = 5.51$ m which serves the condition $\frac{5.51 \text{ m}}{17 \text{ m}} \approx 0.32 \ll 1$. This condition is illustrated within Figure 3.3 where the influence of the structure on the wavelength falls within 1% over the entire frequency range (red line).

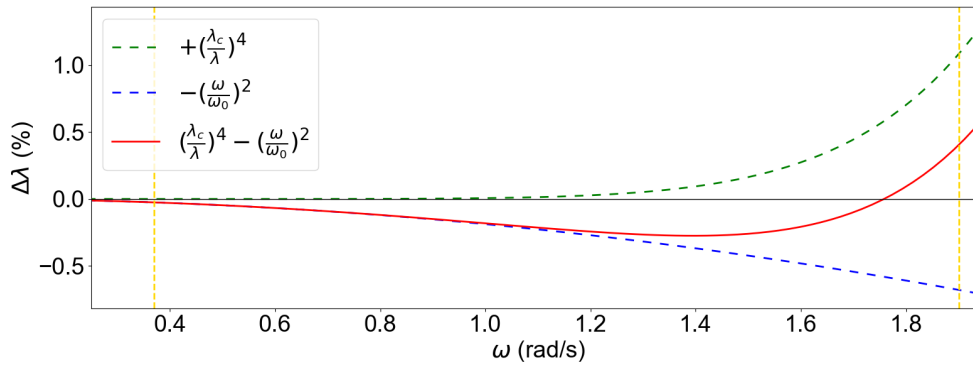


Figure 3.3: Magnitude of the hydroelastic terms stated in Equation 2.7 for the chosen cross section over the wave frequencies. The continuous line represents $(\frac{\lambda_c}{\lambda})^4$ and the dashed line represents $(\frac{\omega}{\omega_0})^2$. The orange dashed vertical lines bound the interval of expected wave frequencies during operations.

3.2. Drum

The design of the steel depends on the chosen diameter ϕ_{drum} and wall thickness t_{drum} . The length of the drum should equal the width of the sheet B to be able to spool the sheet on the drum. The parameters above combined, determine the hydrodynamic response to wave loading of the rigid body. Heave z_{drum} (vertical displacement) and roll ϕ (rotation along drum centroidal axis) are governing while assessing head loading. The natural frequencies ω_0 of both motions are conditioned to understand the influence of ϕ_{drum} and t_{drum} on the hydrodynamic response [7]. The motions will mimic the excitation frequency ω if $\omega_0 > \omega$, implying the (restoring) stiffness term dominates over the mass term [22].

The heave natural frequency $\omega_{0,z_{drum}}$ depends on the total mass (structural mass m_{drum} and added mass a_3) and the hydrostatic restoring force of the fluid, proportional to the waterplane area A_{wl} as shown in Equation A.16. The roll natural frequency $\omega_{0,\phi}$ depends on the total moment of inertia around the center of gravity CoG , and also depends on the shift in horizontal position of CoG during a rotation which determines the restoring moment as shown in Equation A.17.

The total moment of inertia consists of the moment of inertia of the drum around the centroidal axis I_{yy} and the additional moment of inertia due to the surrounding fluid which must be displaced during a rotation δI_{yy} . The horizontal shift of CoG depends on the vertical distance between CoG and the rotation point, which is known as the metacentric height GM . For a circular cross section, the point of rotation lies within the circle center and therefore GM is independent of the rotation angle [29].

$$\omega_{0,z_{drum}} = \sqrt{\frac{A_{wl}\rho_w g}{m_{drum} + a_3}} \quad (3.3)$$

$$\omega_{0,\phi} = \sqrt{\frac{GM m_{drum} g}{I_{yy} + \delta I_{yy}}} \quad (3.4)$$

3.2.1. Design properties

To look at the design properties, the drum is functional both during deployment as well as during transport.

- During transport the thin sheet is spooled on the drum to limit the occupied deckspace.
- During deployment the mooring lines are connected to the drum and the stiff drum functions as (horizontal) spreader bar at the front of the thin sheet.

From a structural point of view, this implies that the drum design should be able to withstand the load of the sheet during transport. The chosen \varnothing_{drum} determines the imposed curvature of the thin sheet which should be bigger than 0.3 m to prevent damage to the PV. The bending stress within the drum and thin sheet decrease with increasing diameter due to the lower curvature. The stress should not exceed the yield stress σ_{yield} of the used materials for the thin sheet cross section stated in Table 3.1.

To reduce the reflected energy and resulting drift forcer from a hydrodynamic perspective, the wave structure interference should be minimized. This requires the natural frequencies to be bigger than the excitation frequency ω . Both natural frequencies for heave and roll should be aimed to be at the higher side of the workability spectrum of Sleipnir ($\omega = 0.4 - 1.9$ rad/s).

The heave natural frequency can be influenced by adjusting the draft which is related to A_{wl} and indirect to \varnothing_{drum} . The water displacement, required to provide sufficient buoyancy, determines the required draft (dependent on the structural geometry). Therefore, \varnothing_{drum} in combination with the mass, determines the draft. The structural mass m_{drum} can be influenced by adjusting the wall thickness t_{drum} .

The roll natural frequency can be influenced by the structural mass m_{drum} , can be influenced by the distribution of the mass over the cross section $I_{yy,drum}$ and can be influenced by the cross section geometry represented as δI_{yy} . The natural frequencies are also dependent on the connection design since the mass and location of the connection, along the circumference of the drum, determine the influence on the moment of inertia and CoG position of the combined structure. Hence, first the connection will be discussed and thereafter the natural frequencies of the drum are evaluated. The parallel axis theorem is used to determine the total I_{yy} around CoG for n elements as stated in Equation 3.5. The contribution of n elements depends on its own moment of inertia $I_{yy,i}$, the element mass m_i and the distance perpendicular to the force direction from the elements CoG to the drum CoG indicated by r_i .

$$I_{yy} = \sum_{i=1}^n I_{yy,i} + m_i \cdot r_i^2 \quad (3.5)$$

For the feasibility study of Sleipnir a drum constructed of steel (type S235) with $\varnothing_{drum} = 4.8$ m and $t_{drum} = 20$ mm is chosen. This design does not exceed σ_{yield} of the materials as evaluated in

Appendix A. The drum is enclosed on both sides by a steel plate of 2 cm to make the drum watertight. The diameter and wall thickness are correlated by reason of the stated minimum wall thickness by the manufacturer for monopiles. Hence, different configurations are possible for the drum design and during the preparations of the model tests, the influence of design parameters (mass and C_{oG} position) was evaluated to improve the design on model scale.

3.3. Connection

The connection links the thin sheet to the drum and has an important roll in the coupled motions. The connection design should allow for a smooth transition from the spooled situation to the deployed situation to prevent exceeding the yield stress due to excessive curvatures of the sheet.

The thin sheet can be either clamped or hinged connected to the drum as schematized in Figure 3.4, the differences can be explained by understanding physics. A transition of the sheet is required to align with the horizontal free-floating sheet from the connection located underwater. The curvature of the sheet represents the bending moment at that location [34]. However, a hinged connection is not able to transfer the bending moment of the sheet to the drum, whereas a clamped connection restrains the sheet in a certain direction and is able to transfer the moment to the drum. The bending moment is depending on the curvature at the connection location combined with the bending stiffness of the thin sheet.

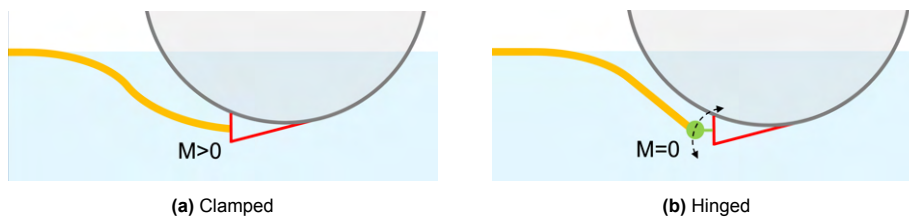
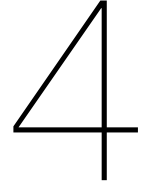


Figure 3.4: Different options for the design of the connection

For this study, a clamped connection is chosen because this generates a counteracting moment to the roll motion of the coupled system. The detailed connection design must be made in the next design phase. For now, the connection is approximated as a mass $m_{connection}$ which is positioned vertically below the drum center. To give an example, a reasonable connection can be made of a steel plate with a width of 2 m and a wall thickness of 3 cm over the entire length of the drum. $m_{connection}$ changes the C_{oG} position of the drum and leads to an increase in roll moment of inertia which is determined by using Equation 3.5.

The total mass of the drum depends on the drum combined with mass of the connection and steel enclosure at both sides. It turns out that the natural heave frequency of the designed drum is $\omega_{0,z_{drum}} = 2.22$ rad/s and the natural roll frequency is $\omega_{0,\phi} = 18.9$ rad/s as evaluated in Appendix A.

$$m_{drum,tot} = m_{drum} + m_{connection} + m_{enclosure} \approx 84 \times 10^3 \text{ kg} \quad (3.6)$$



Scaling concept to model scale

Scaling laws ensure the full scale geometry and/or kinematics related to the velocities are similar on model scale. For this experiment, the hydrodynamic interaction due to the surface waves is of most importance. Hence, scaling should be aimed to have dynamic similarity where the ratios between the forces and accelerations on real scale and model scale are the same [22]. Scaling based on dimensionless numbers are useful since properties can be related to each other without accounting for time varying dependencies such as temperature and pressure. Surface waves are gravity driven and Froude scaling ensures that the gravity forces are well scaled. The viscosity will not be scaled well while using Froude (water is used on full and model scale). This results in wrong scaling of friction effects whereas proper scaling could be obtained by scaling according to Reynolds instead of Froude. The dimensionless Froude number,

$$Fr = \frac{F_{inertia}}{F_{gravity}} = \frac{\rho u^2 L^2}{\rho g L^3} = \frac{u^2}{gL} \quad (4.1)$$

where u is the fluid velocity and L the structural length. The Froude number should be ideally the same for model scale (subscript m) and real scale (subscript r),

$$\frac{u_m^2}{gL_m} = \frac{u_r^2}{gL_r} \rightarrow u_m = u_r \sqrt{\frac{L_m}{L_r}} = u_r \cdot \alpha \quad (4.2)$$

both cases are related to each other by geometric scaling factor α . The scale model must fit in the towing tank and therefore α is chosen as $\frac{1}{30}$, resulting in $L_m = 5.00$ m and $W_m = 1.00$ mm which is smaller than the towing tank width of 2.75 m. The other relations are obtained from the physical dimensions and are summarized in Table 4.1 [12]. The water density of ocean water on full scale $\rho_{w,r} = 1025$ kg/m³ differs from the water in the towing tank $\rho_{w,m} = 1000$ kg/m³ which will be taken into consideration for the scaling.

Parameter	Dimension	Scale factor
Length	m	α
Mass	kg	$\alpha^3 \frac{\rho_{w,m}}{\rho_{w,r}}$
Force	N	$\alpha^3 \frac{\rho_{w,m}}{\rho_{w,r}}$
Moment	Nm	$\alpha^4 \frac{\rho_{w,m}}{\rho_{w,r}}$
Acceleration	m/s ²	1
Time	s	$\sqrt{(\alpha)}$
Pressure	N/m ²	$\alpha \frac{\rho_{w,m}}{\rho_{w,r}}$

Table 4.1: Multiplication factors to scale parameters from real to model scale

Scaling the global structural rigidity is based on scaling the real case deflection $\delta_r = \frac{FL_r^3}{EI_r}$ with $F \sim \rho u_r^2 L_r^2$ by scale factor α to obtain the deflection on model scale δ_m . The following relation should hold:

$$\frac{\delta_r}{L_r} = \frac{\delta_m}{L_m} \rightarrow \frac{\rho_{w,r} u_r^2 L_r^5}{L_r (EI)_r} = \frac{\rho_{w,m} u_m^2 L_m^5}{L_m (EI)_m} \rightarrow (EI)_m = (EI)_r \cdot \alpha^5 \cdot \frac{\rho_{w,m}}{\rho_{w,r}} \quad (4.3)$$

If geometric similarity is achieved, only $I \cdot \alpha^4$ is scaled correctly, which requires the material elasticity E to be scaled with α as well. Another approach could be that E remains similar, and to change the structural composition internally to achieve the scale the moment of inertia with α^5 . For this study and also VFFS in general, the global stiffness is not of main importance but the hydroelastic terms k_p and ω_0 (Equation 2.1.1) should be scaled well to ensure equal hydrodynamic response. k_p inversely depends on the characteristic length λ_c in relation to the structural length L , which should be scaled with α^4 as shown in Equation 4.4. The initial draft d_0 related to the structural height, must be the equal to scale the natural frequency of the sheet ω_0 well as shown in Equation 4.5. The initial draft depends on the structural mass $L^3 \rho_{sheet}$ and water volume is required to replace to have sufficient buoyancy on the horizontal area of the sheet L^2 .

$$\frac{\lambda_{c,r}}{L_r} = \frac{\lambda_{c,m}}{L_m} \rightarrow 2\pi \left(\frac{D_r B_r}{\rho_{w,r} g B_r} \right)^{\frac{1}{4}} = 2\pi \left(\frac{D_m B_m}{\rho_{w,m} g B_m} \right)^{\frac{1}{4}} \rightarrow D_m = D_r \cdot \alpha^4 \cdot \frac{\rho_{w,m}}{\rho_{w,r}} \quad (4.4)$$

$$\frac{L_r^3 \rho_{sheet}}{L_r^2 d_{0,r} \rho_{w,r}} = \frac{L_m^3 \rho_{sheet}}{L_m^2 d_{0,m} \rho_{w,m}} \rightarrow d_{0,m} = d_{0,r} \cdot \alpha \cdot \frac{\rho_{w,m}}{\rho_{w,r}} \quad (4.5)$$

In Table 4.2 the properties on full scale are related to model scale based on Froude scaling. The hydrodynamic parameters λ_c and d_0 are added to validate proper scaling of the hydroelasticity.

	Parameter	Scale factor	Real	Model	Unit
Thin sheet	Length	L	α	150	5 (m)
	Width	B	α	30	1 (m)
	Flexural rigidity	D	$\alpha^4 \frac{\rho_{w,m}}{\rho_{w,r}}$	5581	0.0069 (Nm)
	Characteristic length	λ_c	$\alpha \frac{\rho_{w,m}}{\rho_{w,r}}$	5.51	0.18 (m)
	Draft	d_0	$\alpha \frac{\rho_{w,r}}{\rho_{w,m}}$	20.49	0.67 (mm)
Drum	Diameter	\varnothing_{drum}	α	4.8	0.16 (m)
	Wall thickness	t	α	20	0.67 (mm)
	Mass	m_{drum}	$\alpha^3 \frac{\rho_{w,m}}{\rho_{w,r}}$	83832	3.03 (kg)

Table 4.2: Full scale properties scaled to model scale to have dynamic similarity with geometric scale factor $\alpha = \frac{1}{30}$.

4.1. Construction of scale model

For the thin sheet, a neoprene sheet with $h = 0.005$ m and density $\rho_{sheet} = 140$ kg/m³ is chosen. The horizontal dimensions of the used sheet with $L = 4.95$ m and $B = 1.02$ m differ slightly from the ideal theoretical scaling stated in Table 4.2. Due to dramatically impacted delivery times due to the COVID-19 virus around the world, this available sheet at the TU Delft was used. The flexural rigidity of the sheet $D = 6.9 \times 10^{-3}$ Nm is determined in a previous experiment with the use of a static deflection test with a localized load using Equation 2.3 [37], resulting in a Young's modulus $E = 560$ kPa while assuming a Poisson ratio $\nu = 0.4$. The hydroelasticity is equal for model scale as expected at full scale since the characteristic length $\lambda_c = 0.18$ m and draft $d_0 = 0.67$ mm of the thin sheet are scaled well.

For the drum a PVC cylinder with $\varnothing_{drum} = 0.16$ m, width $B = 1.01$ m and wall thickness $t = 4$ mm is chosen, resulting in $m_{drum} = 2.35$ kg. Geometrically the drum is scaled well but due to the use of different materials the mass had to be increased. A PVC lid at both sides $m_{lids} = 0.22$ kg is attached to prevent water from draining into the drum while deployed. The connection on model scale is constructed of two small aluminum profiles mounted to the drum to be able to attach the force transducers as shown in Figure 4.1. The thin sheet is connected to the force transducers on the other side. The thin sheet is clamped between two plastic strips screwed to a rigid aluminum profile. This prevents the generation of bending stresses along the width of the strip and makes sure the entire load of the thin sheet is transferred to the force transducers. The entire connection adds $m_{connection} = 0.26$ kg to the drum. However, the mass is still lower on the model scale than determined by scaling the designed real

properties as shown in Table 4.2. Nevertheless, the drum properties remain arbitrary choices and even on full scale the mass can be increased either permanent or temporary by ballasting with for example water.



Figure 4.1: Technical drawing of the connection and the constructed connection in x, z -plane.

4.1.1. Influence of design parameters

The magnitude of additional masses influences the draft of the drum, and the mounting location affects the position of CoG and the moment of inertia. The combination of the magnitude and location, changes the coupled hydrodynamic behaviour during deployment. Several configurations are tested statically in the towing tank to identify the influence of changing the design parameters and determine the most promising concept. Ideally, the heave and roll natural frequency of the model is chosen at the higher side of the workability wave spectrum of Sleipnir. This is preferred since the structure is expected to follow the excitation motion better, leading to negligible wave structure interaction. The natural heave and roll frequency is determined with a free decay test by averaging the time over four oscillations. A table made of wood while stiffened with an aluminum profile is mounted inside the drum to be able to place additional masses at different locations along with the geometry. Small blocks made of lead with $m \approx 0.245$ kg were used as additional masses.

The submerged part of the thin sheet generates an upward buoyant force due to the difference in density ($\rho_w - \rho_{sheet}$) leading to a moment exerted on the drum. This moment is counteracted by a moment that is proportional to the horizontal distance of CoG to the drum center. Positioning CoG close to the drum center leads to a small moment and therefore the connection moves towards the free surface in the undisturbed situation as shown in Figure 4.2a. An air gap is created above the water level because the curvature is limited by the flexural rigidity of the sheet. This can result in slamming during rotations which should be prevented. The connection remains straight below the drum center if CoG is positioned horizontally further away from the drum center shown in Figure 4.2b. The sheet departure angle of the sheet is horizontal, equal to the free-floating sheet. No bending moment is exerted on the drum by the sheet since the (horizontal) lever arm is close to zero. Thus, the sheet does not influence the roll motion and the heave natural frequency is slightly increased due to the increased hydrostatic stiffness of the submerged sheet (relative large submerged length). Increasing the draft of the drum to half the drum diameter results in a slow system shown in Figure 4.2c, lowering both natural frequencies which is unfavorable. The most promising configuration has four additional masses placed slightly off the drum centerline at the bottom of the drum shown in Figure 4.2d. Some curvature of the sheet is present at the connection resulting in a bending moment counteracting the roll motion, while the sheet is able to transition smoothly to the free-floating sheet without an air gap. The natural frequency of the chosen configuration is $\omega_{0,z_{drum}} = 10.8$ rad/s and $\omega_{0,\phi} = 7.1$ rad/s.

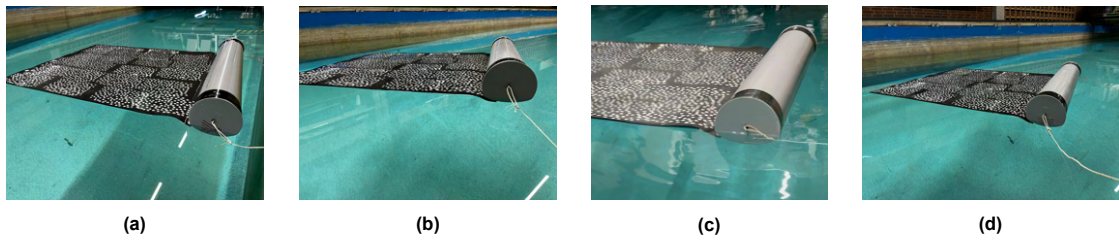


Figure 4.2: Visualization of the discussed configurations

4.1.2. Validate properties of scale model

The scale model is constructed of several elements as visualized in Figure 4.3. Table 4.3 list the elements with the corresponding colors.

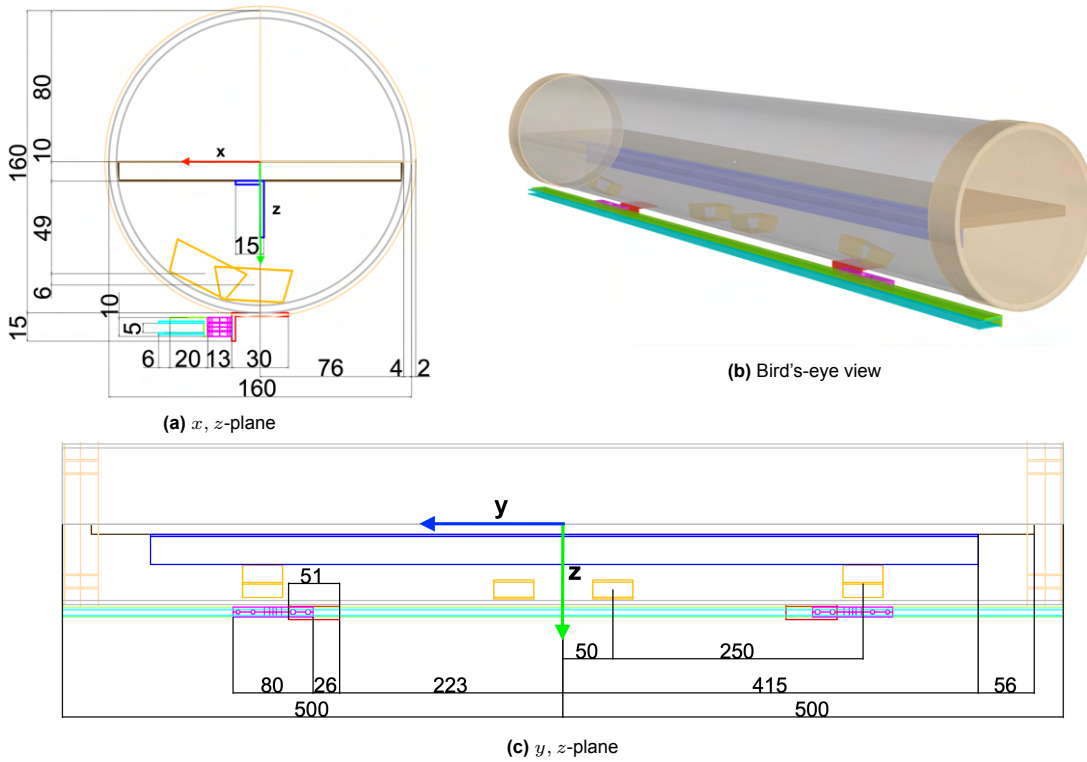


Figure 4.3: Technical drawing of the scale model

Element	Material	Thickness (mm)	Mass (g)
Drum	PVC	4	2350
Lid	PVC	2	220
Mass	Lead	14	972
Table	Wood	10	780
Table reinforcement	Aluminium	3	291
Drum mount	Aluminium	2	24
Force transducer	Aluminium	10	19
Sheet mount	Aluminium	2	151
Sheet clamping	Plastic	1	46
			4853

Table 4.3: Description of elements used to construct the scale model

The Center of Gravity CoG is experimentally determined in Appendix B and turns out to be positioned at coordinates $CoG_x = 5$ mm, $CoG_z = 18$ mm where $x = 0, z = 0$ lays within the drum center.

Sling theory is used in an experimental setup to determine the moment of inertia I of the scale model in all three directions in the workshop. This method has an accuracy of $\pm 2\%$ and is extensively discussed in Appendix B. The moments of inertia are listed in Table 4.4.

I_{zz}	3.97E+05	kgmm ²
I_{xx}	3.94E+05	kgmm ²
I_{yy}	2.21E+04	kgmm ²

Table 4.4: Moment of inertia of the scale model

4.2. Wave loading

As mentioned, the system will follow the excitation motion if the excitation frequency ω is smaller than the natural frequency of the structure ω_0 . Regular waves are used in the experiment since these are repeatable and ideal for analyzing the response at a certain frequency over successive periods. Relative significant wave structure interaction is expected at the higher frequencies for the thin sheet whereas little energy is present in the workability spectrum of Sleipnir. However, Sleipnir is vulnerable to large wavelengths tending towards the structural length of 200 m whereas the scale model is expected to mimic this kind of waves easily. Therefore, wave frequencies containing more energy in the workability spectrum should be used to indicate the response over the frequency domain. The chosen wave frequencies are listed in Table 4.5 and the corresponding wavelength λ is obtained via the dispersion relation. All wave frequencies are lower than the heave natural frequency $\omega_{0,z_{drum}} = 10.8$ rad/s and wave 2 is chosen around the roll natural frequency of the system $\omega_{0,\phi} = 7.1$ rad/s.

The wavelength λ combined with the wave steepness $H_{\bar{\lambda}}$, characterize a wave. The steepness of the different waves (waves 1,2,3 and 4) is chosen to be constant at 0.040, which is at the steeper side of the described average wave steepness range by DNV of $\frac{1}{50} - \frac{1}{20}$ [12]. Steeper waves result in larger curvatures of the sheet and contain more energy according to Equation 2.5. The effect of increasing the steepness even further is evaluated with the use of wave 5 which has an equal wavelength as wave 3 with a steepness of 0.065, still below the wave breaking limit of 0.071 [16]. The corresponding wave height H can be calculated with the use of the chosen steepness and frequency (with the use of the dispersion relation). Four waves are classified as Stokes second order and wave 5 as Stokes third-order according to Figure 4.4, where $d = 1.238$ m refers to the water depth in the tank.

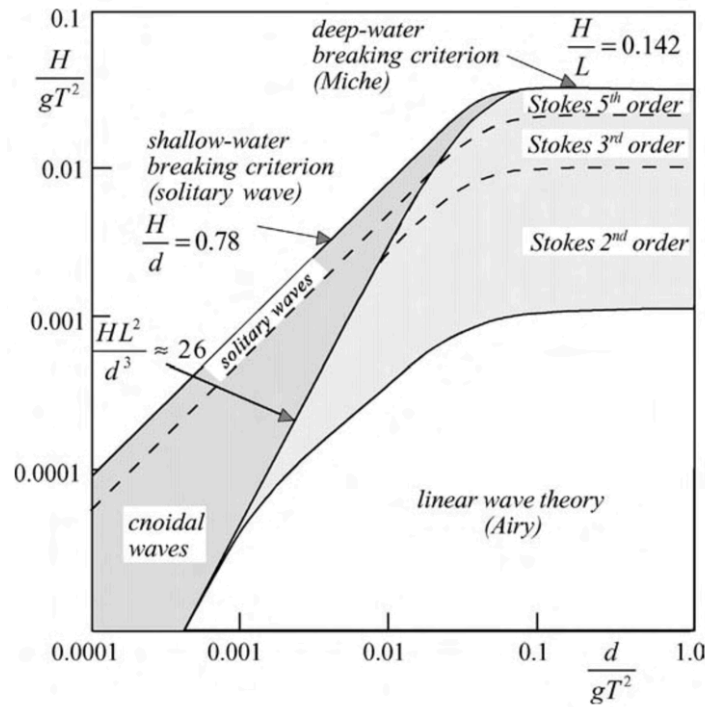


Figure 4.4: Applicability of wave theories [26]

All waves are nonlinear and do not entirely mimic a sinusoidal shape. Wave steepness is the main driver of nonlinearity and all average waves provided by DNV end up being Stokes second order. The contribution of the nonlinear terms in Stokes second order is small, simply stated, the troughs are less deep and the crests are a little higher. Therefore, linear wave theory (Airy) based on regular waves may be used to describe waves 1-4 [31] stated in Table 4.5.

	Full scale				Model scale				steepness (-)	$\frac{H}{gT^2}$ (-)
	ω (rad/s)	T (s)	λ (m)	H (m)	ω (rad/s)	T (s)	λ (m)	H (mm)		
wave 1	0.85	7.39	85.31	3.40	4.66	1.35	2.84	113	0.040	0.006
wave 2	1.28	4.91	37.62	1.50	7.01	0.90	1.25	50	0.040	0.006
wave 3	1.75	3.59	20.13	0.80	9.59	0.66	0.67	27	0.040	0.006
wave 4	2.00	3.14	15.41	0.61	10.95	0.57	0.51	20	0.040	0.006
wave 5	1.75	3.59	20.13	1.30	9.59	0.66	0.67	43	0.065	0.010

Table 4.5: Chosen waves based on the workability spectrum of Sleipnir and scaled to model scale according to Froude ($\omega \sim \sqrt{\alpha}$ and $H \sim \alpha$).

5

Experimental setup

The goal of the experimental approach is to gain an understanding of the hydrodynamic behaviour of the OFPV concept designed for HMC where the following three parameters are measured during the runs in the towing tank.

- Mooring force: this is a key driver for making temporary deployment possible since large mooring loads require an advanced mooring system.
- Connection force: the connection could be designed in different ways and influences the motions of the coupled system, an indication of the magnitude helps to understand the hydrodynamic behaviour of the concept.
- Drum motions: the hypothesis is that the drum mainly influences the coupled motions since the sheet is expected to mimic the excitation motion. The vertical and the horizontal displacement and the rotation of the drum are obtained in the xz -plane.

The experiments are carried out in Towing Tank No.2 of the Mechanical, Maritime and Materials Engineering Faculty at the Delft University of Technology, which has a length of 85 m, a width of 2.75 m and maximum water depth of 1.25 m. The water depth during the experiments was 1.238 m and the water temperature was 16.8 °C.

5.1. Properties of the setup

The piston-type wavemaker generates waves traveling to the wave dampening beach on the other side of the tank where a wave probe measures the surface elevation during the experiment. The model is positioned at 27.34 m from the wavemaker and two flexible mooring lines both at the front and aft hold the model in place. A camera mounted to the roof captures the top view of the model and a camera positioned beside the towing tank records the side view (xz -plane). A flickering light that is placed on top of the sidewall of the towing tank is used for time synchronization while processing the conducted data and video footage.

Two force transducers within the thin sheet and drum connection measure the connection force. One mooring line is connected to the 3D-sensor frame which is designed by Van der Voort [48] consists of three identical force transducers, to measure the line force. All force transducers are Zemic Type 1R1-K with a maximum load capacity of 20 N.

The wave probes are positioned in the middle of the towing tank supported by a 80 mm I-tem profile orthogonal aligned to the tank sidewalls. The first wave probe is located 21.70 m from the wavemaker and the distance between the two probes is 7.00 m. The second wave probe (2) in Figure 5.2 is used to determine the wave properties at the model location. The initial position of the model (front drum) is 6.64 m from the first wave probe.

One roof-mounted camera is used of type OptiTrack SlimX 13 recording with 240 fps. The field of view shown in Figure 5.3 ranges over the entire towing tank width and the length in x -direction is 2.2 m

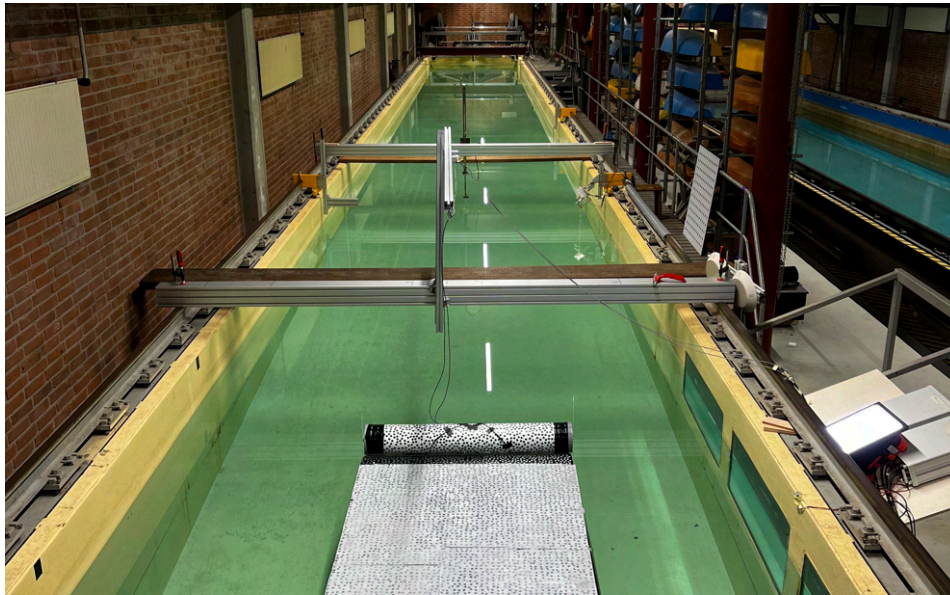


Figure 5.1: Overview of the real setup in the towing tank

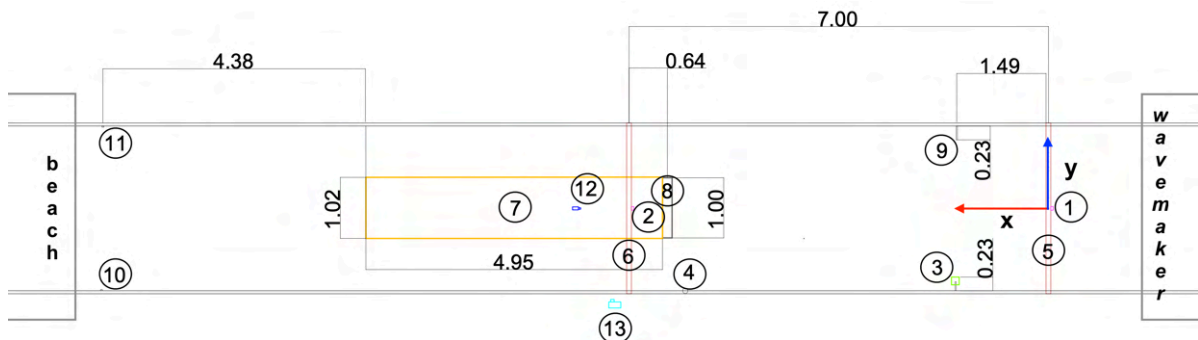


Figure 5.2: Overview of the experimental setup in meters. 1 and 2 represent the first and second wave probe, 3 represent the 3D-sensor used for the mooring force, 4 the light bulb, 5 and 6 the horizontal beams used to attach the wave probes, 7 the thin sheet, 8 the drum, 9 the (right) front mooring connection, 10 and 11 the (left and right) aft mooring connection, 12 the roof-mounted camera, 13 the camera besides the towing tank.

indicated by the black tapes on the wall in Figure 5.1. Initially, the drum is at the outer side of the field of view to be able to capture the front of the model and allows for a horizontal offset in positive x -direction (caused by the drift force).

The standalone camera is positioned next to the tank sidewall at the center height of the drum (z -direction) is a Nikon D7000 with a focal length of 28 mm recording in 24 fps. It is used to record the motions of the front of the model in the x, z -plane as shown in Figure 5.3.

5.1.1. Mooring system

Soft mooring lines are preferred instead of stiff lines to better replicate the real case. Flexible lines absorb the first order oscillating motions, due to the dynamic wave pressure, by elongation resulting in small forces due to the high elasticity, which is similar to the behaviour of a catenary mooring system. Stiff lines may result in snap loads if insufficient pretension is applied and lines fall slack.

The mooring lines at the front are connected at the center of each side of the drum and the aft lines are connected at the edges of the thin sheet. The aft mooring lines are connected to the sidewalls with magnets placed at the undisturbed water level height. As mentioned, one of the front mooring lines is connected to the 3D-sensor to measure the line force. The force transducers of the 3D-sensor should stay dry during the experiment and the connection point (small orange box in Figure 5.4) is placed 0.13 m above the undisturbed water level to have a safe margin with the highest expected wave



Figure 5.3: Impression of the field of view of the used cameras

amplitude of 0.056 m as shown in Table 4.5.

The soft mooring lines are made of sewing thread with diameters less than 1 mm and stiffness $\frac{\delta F(\epsilon)}{\delta \epsilon} = 0.475 \text{ N}$ determined in a previous experiment [38]. The chosen length l_{before} for all flexible mooring lines is 4.21 m (accuracy of 0.01 m), the front mooring lines are 0.15 m elongated with 1 mm diameter stiff Dyneema line l_{stiff} to be able to connect one line to the 3D-sensor. Pretension force F_{pre} is proportional to the elongation ϵ of the mooring lines as stated in Equation 5.1. The elongated line length in the tank l is obtained with Equation 5.2 from the dimensions shown in Figure 5.2 and visualized directions in Figure 5.4. Note that only the flexible line length is assessed and the additional stiff length (of the front lines) is subtracted.

$$F_{pre} = \frac{\delta F(\epsilon)}{\delta \epsilon} \epsilon \quad (5.1)$$

$$l = \sqrt{(\Delta x)^2 + (\Delta y)^2 + (\Delta z)^2} \quad (5.2)$$

$$\epsilon = \frac{(l - l_{stiff}) - l_{after}}{l_{after}} \quad (5.3)$$



Figure 5.4: Visualization of the geometry of the mooring system in undisturbed water, front left and right mooring line are visible

Furthermore, during the preparation of the experiment, it is observed that the model has a slight rotation in the x, y -plane after connecting the mooring lines. This is solved by shortening the left mooring line at the front (connected to the 3D-sensor) with 0.10 m to introduce additional pretension. The model is orthogonal aligned with the sidewalls of the tank where the model has an offset of -0.095 m in transverse y -direction. The rotation can be ascribed to the prestretch of the mooring lines caused by storing the lines on a spool before deployment. The line lengths measured after the experiment l_{after} show deviations compared to the initial lengths during preparation and these lengths are used to determine the elongation. It turns out the positive y -side aft mooring line is shorter than the other aft mooring line, this explains the required additional pretension at the opposite side at the front to prevent rotation. However, the front and aft pretension are not equal which implies a net force is present. This,

Mooring line		l_{before} (m)	l_{after} (m)	Δx (m)	Δy (m)	Δz (m)	l (m)	l_{stiff} (m)	ϵ (-)	F_{pre} (N)
Front	right	4.21	4.16	5.15	-0.74	-0.12	5.20	0.15	0.21	0.10
	left (3D-sensor)	4.10	4.11	5.15	0.55	-0.12	5.18	0.15	0.22	0.10
Aft	right	4.21	4.16	4.38	0.97	0.01	4.49	0.00	0.08	0.04
	left	4.21	4.26	4.38	-0.78	0.01	4.45	0.00	0.05	0.02

Table 5.1: Measurements of the used mooring lines and an estimation of the applied pretension F_{pre}

however, would result in a drift motion which is not observed. The additional required pretension can probably be ascribed to the horizontal component of the axial force in the free-hanging cable (of the force transducers) visible in Figure 5.3.

5.2. Data acquisition

All sensors (wave probes and force transducers) are powered by an amplifier and the analog output signal (in mV) is strengthened by the amplifier to ± 10 V. The analog signal is passed through a low-pass filter with a cutoff frequency of 100 Hz by connecting the equipment output cable to an input channel of the filter box. The filtered data is acquired on a PC with National Instruments PCI-6033EA/D converter card with a sampling frequency of 1000 Hz and 16-bit resolution (called the Data Acquisition PC). The ratio between sampling frequency and real signal frequency should be bigger than 2 to prevent aliasing. The Nyquist frequency states the maximum frequency which can be measured without the occurrence of aliasing, in this case 500 Hz. Enough data points must be acquired to properly convert the continuous analog signal to a non-continuous digital signal. Although the wavemaker and light require a steering signal sent from the Control PC, the output signals are measured using the same procedure as described for the sensors. All equipment continuously outputs a signal over time and the Data Acquisition PC is used to control when the signal is recorded.

The wavemaker is controlled by a harmonic signal with time steps of 0.01 s and an amplitude within ± 5 V. The output represents the horizontal displacement of the flap and the frequency is incorporated by the voltage change over a time step. Default ramp-up period of 5 s is used by the wave maker to prevent damage by gradually starting the flap motions, implying that the desired waves are not immediately generated. The piston-type wavemaker displaces a water column in horizontal direction over the entire depth. Wave theory states that the energy of long waves penetrates over a larger depth compared to waves with a shorter wavelength. Therefore, the shorter wavelengths require a longer settling distance before becoming reasonable harmonic and therefore a longer ramp-up period (10-15 s) is used.

The recordings of the camera besides the towing tank are stored on a local storage card. The roof-mounted camera is controlled from a separate PC with the program 'Motive', a software program tailor-made for the OptiTrack cameras by the manufacturer. The recordings are stored locally on the PC where Motive is installed. The light requires a 5 V TTL trigger signal to produce a beeping sound and flashing light, sent in a repeatable pattern like [3, 3, 0, 0] for four successive time steps of 0.01 s. The output signal is measured at the Data Acquisition PC in the same time frame as the other sensors. The light trigger is placed within the field of view of the roof-mounted camera and the camera beside the tank records audio to capture the beeping sound. The recordings are captured in a local time frame resulting in a time shift with respect to the other measurements, this illustrates the relevance of the light trigger within the camera view. Hence, the output signal, the flashing light and the beeping sound are used to synchronize measurements during post-processing.

5.3. Test procedure

The run is initiated from the Control PC and Data Acquisition PC located on the carriage car of the towing tank. The steering signal for the wavemaker and light bulb is sent from the Control PC and simultaneously the data measurements are started at the Data Acquisition PC by hand. Small timing errors do not matter because all output signals are acquired in the local time of the Data Acquisition

PC for both the used sensors and the steering signals. The wavemaker steering signal has a length of 120 s and the measurement recordings are stopped after 200 s.

The recording of the roof-mounted camera is started with the program 'Motive' directly after the measurements at the Data Acquisition PC are initiated. The recording of the camera besides the tank is manually started just before the first wave arrives at the model location to prevent unnecessary long recordings. In case the front of the model moves almost out of the field of view, the camera is rotated to record the motions in the shifted position.

Before a run is started a zero-measurement of 120 s is performed to indicate the surface elevation motions in the towing tank. A new run is started if the residual waves in the towing tank have an amplitude less than 0.5 mm. Generally, a waiting time of around 30 min is sufficient between successive runs.

5.4. Calibration

All sensors are calibrated as used during the experiment at the carriage car of the towing tank with the in-situ cable length. This prevents deviations due to changing the wiring or using different amplifiers during the real runs compared to the calibration.

5.4.1. Mooring force

The sensitivity of the three sensors is determined in Appendix C where the calibration procedure is described. The measured voltages of the three sensors are converted into forces in the three orthogonal directions by Equation 5.4 while using the obtained calibration parameters B_0 and B_1 .

$$[F_z \ F_y \ F_x] = [U_1 \ U_2 \ U_3] B_1 + B_0 \quad (5.4)$$

$$B_0 = (-0.8174 \ 1.6879 \ -1.2349); \quad B_1 = \begin{pmatrix} 2.4382 & 2.9596 & -0.1637 \\ 2.0912 & -1.4830 & 2.5995 \\ -2.3374 & 1.8679 & 2.7536 \end{pmatrix}$$

The calibration is performed with a certain angle of the 3D-sensor at the carriage car where the calibration setup is configured. The 3D-sensor is moved from the carriage car to the towing tank, where the angle and orientation in the towing tank must equal the angle during the calibration procedure to be able to use the obtained calibration. The angle is set equal manually by leveling in the towing tank.

The sensor is 180° rotated in the tank compared to the calibration setup, where the relative orientation of the sensors has not changed. The orientation and angle in the towing tank is checked by applying loads in all three orthogonal directions according to the towing tank axis, a load in one direction should not result in forces in the other two directions. In case a force is measured in the other two directions, this implies a rotation angle is introduced compared to the calibration setup. This error is predictable over all axis and can be accounted for in the force calculation using the rotation matrix proposed by Van der Voort in [48].

During this experiment, the orientation in the towing tank is checked by pulling the mooring line along the x - and y -axis of the tank. The orthogonality is measured using a tape measure and the line is pulled manually (not with an outlined supporting frame as used in the calibration setup) which may result in small deviations in the pulling direction. The x -direction is obtained by measuring the horizontal (y) distance from the wall to the connection point of the 3D-sensor and the vertical (z) distance from the water level to the connection point. For the validation of the y -direction, the mooring connection at the opposite wall is used which is aligned during the preparation of the experimental setup. This may result in a cosinus error of 1% for a pulling angle error of 8°, with a used line length of 2.75 m this translates to 38 mm deviation in the perpendicular direction. The actual measurement error of the manual procedure is within a few millimeters and should therefore not result in an error (forces measured in the other two directions). The general orientation and directions can be validated using this method. Higher accuracy can be obtained by precisely outlining the directions in the tank with for example an (orthogonal) calibration frame.

First, the line is pulled parallel to the towing tank wall in x -direction and thereafter orthogonal to the towing tank wall along the y -axis. With the use of the time signal of the voltage outputs of the sensors

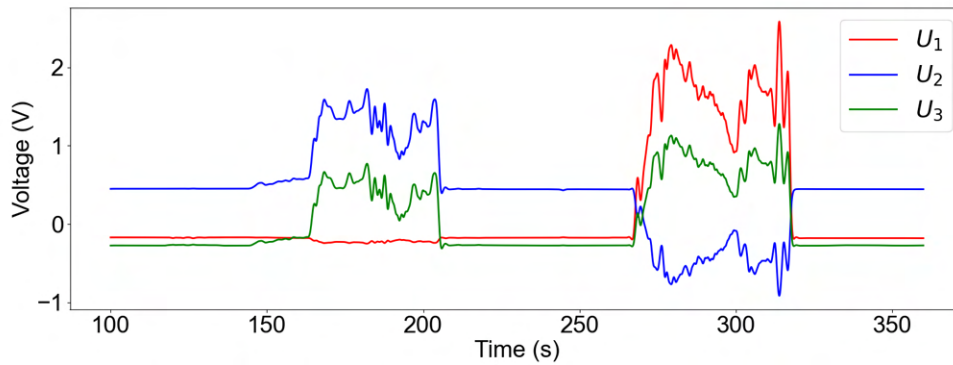


Figure 5.5: Validate 3D-sensor orientation in the towing tank. The output of the sensors by pulling in x - and y -direction, data is filtered with a 3-pole low pass filter with $0.001\times$ Nyquist frequency.

shown in Figure 5.5 and Equation 5.4, the forces are determined in the three directions.

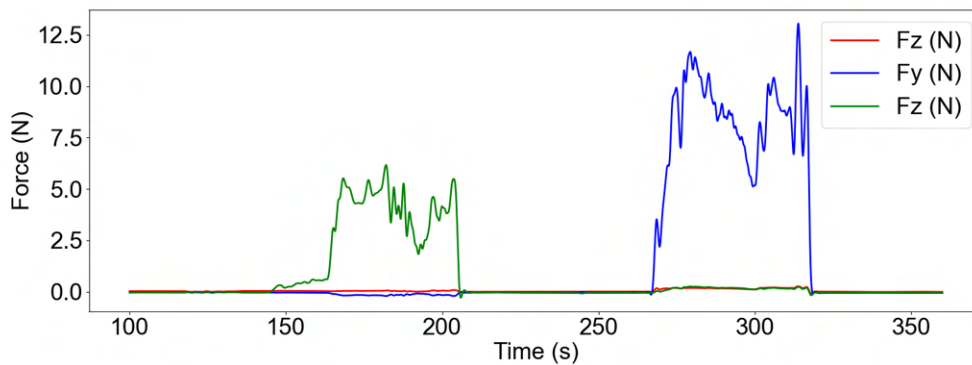


Figure 5.6: Validate 3D-sensor orientation in the towing tank. Initial offset is removed by subtracting the mean value over the first 125 s over the entire signal and data is filtered with a 3-pole low pass filter with $0.001\times$ Nyquist frequency

The calculated forces are shown in Figure 5.6 where the mean force of the undisturbed situation (0-125 s) is subtracted from the entire signal. The load peaks in the pulling direction and a small deviation from zero is visible in the other directions. This indicates a slight rotation of the sensor compared to the calibration setup. The contribution in the other directions is around 2.5 % of the pulling force for the x -axis and around 1.5 % for the y -axis, conducted from Figure 5.7. The small forces measured in the non-pulling direction should come from a rotation and can not be caused by manual pulling errors as motivated. For this study, the error in the forces due to contributions in the other directions is small enough, compared to the force measured in the desired direction to use the described setup. The goal is to determine the magnitude of the mooring force and therefore the $\pm 2.5\%$ accuracy is acceptable.

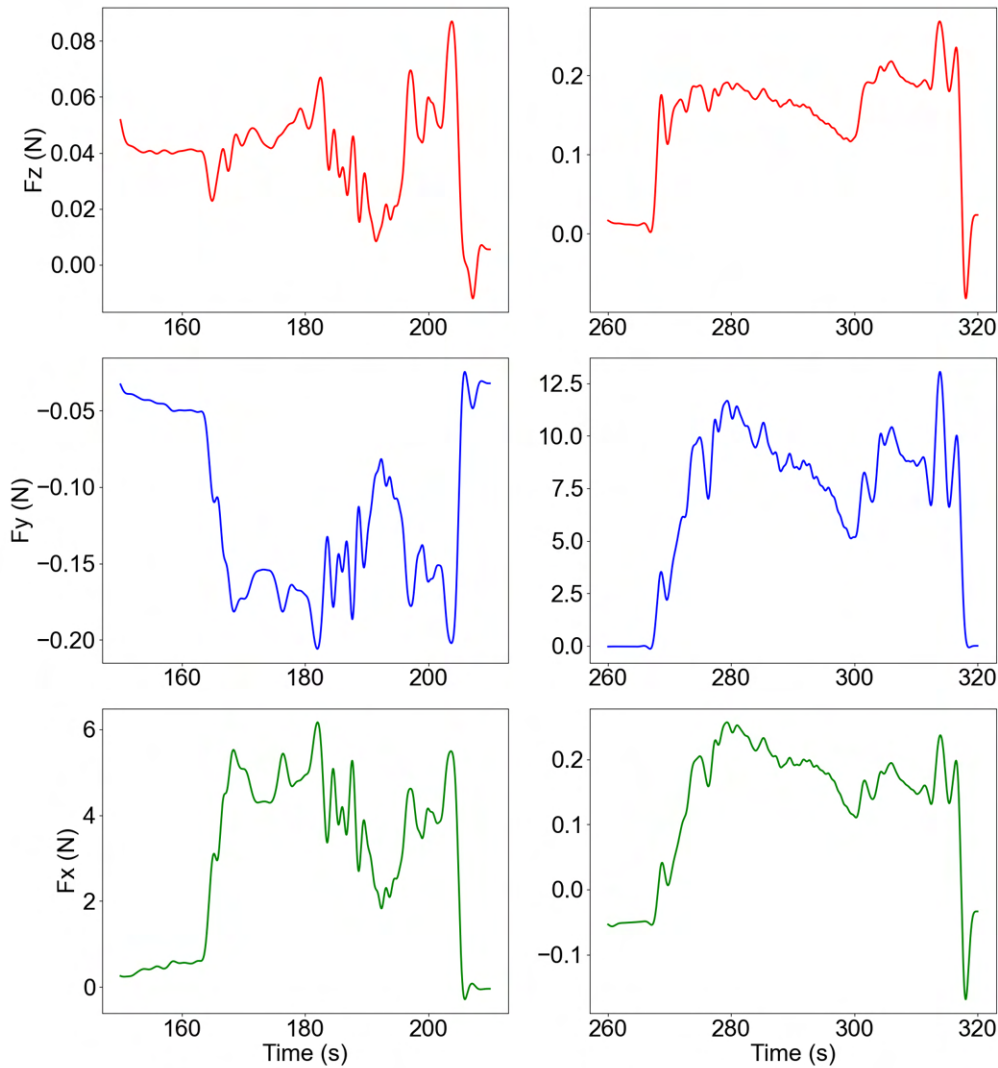


Figure 5.7: Visualization of the 3D-sensor accuracy. Left plots show the forces while pulling in the x -direction, and right plots show the forces while pulling in the y -direction. Oscillations are caused by frequently pulling and releasing the wire. Initial offset is removed by subtracting the mean value over the first 125 s over the entire signal and data is filtered with a 3-pole low pass filter with $0.001 \times$ Nyquist frequency.

5.4.2. Connection force

The calibration performed to obtain the sensitivity of the two force transducers used to measure the connection force is discussed in Appendix C. The measured voltages U (V) are converted to forces F (N) using Equation 5.5 and the regression parameters listed in Table 5.2 obtained in the calibration.

$$F = U\beta_1 + \beta_0 \quad (5.5)$$

	β_1 (N/V)	β_0 (N)
F_{right}	-3.371	-3.319
F_{left}	0.528	0.528

Table 5.2: Obtained values for relating the measured voltages to forces for both force transducers

The force transducers are mounted that a tensile force leads to a positive force as shown in the calibration and compression forces have a negative sign. The force transducer must be able to freely

bend in the working range of ± 1 mm. Therefore, two small strips (thickness of 2 mm) made of polyvinyl chloride are mounted between the strip and force transducer as shown in Figure 5.8.



Figure 5.8: Force transducers are installed to have a positive sign for tensile loads and a negative sign for compression loads

5.4.3. Wave probes

The working principle of the used wave probes is based on the magnitude of the current between the two vertical (stainless steel) wires which has a reasonable linear relation to the submerged height. The calibration factor states the sensitivity of the wave probe in mm/V to convert a measured voltage (V) into surface elevation (mm). The wave probe is calibrated in steps of 20 mm over the entire working range of 200 mm in a step-wise manner over time. The time signal consists of multiple steps of 30 s and is decomposed into discrete output values by averaging over 15 s within the stable interval as shown in Figure 5.9 (indicated in red).

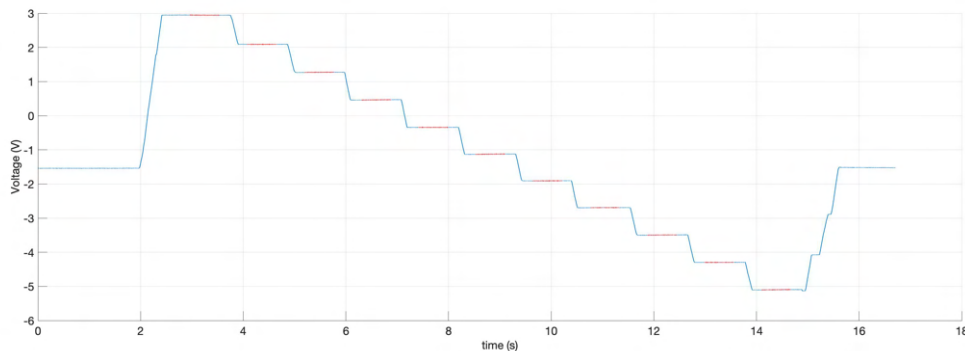


Figure 5.9: Wave probe calibration in steps of 20 mm (run 243, probe 1) and the voltage output of each step calculated by averaging over the stable interval shown in red

The average voltage output is determined during each step of -20 mm and is described by a linear relation,

$$y = \beta_1 \cdot x + \beta_0 \quad (5.6)$$

where y is the measured voltage (V), x is the vertical height (mm), β_1 represents the slope (V/mm) and β_0 represents the intercept at $x = 0$ (V). To obtain the calibration factor β_1 in (mm/V) the equation should be inverted,

$$x = \frac{y}{\beta_1} - \frac{\beta_0}{\beta_1} \quad (5.7)$$

The sensitivity (slope) of the wave probe is determined with linear regression with a similar procedure as described for the force transducers in Appendix C. The least-squares method is used for the regression based on the principle of minimizing the sum of the residuals squared. Over time, the sensitivity of the wave probe can slightly change, and therefore the calibration factor is determined at the start of each day before the starting of the runs (undisturbed water level) to account for deviations. The

wave probes are entirely lowered overnight to reduce differences in corrosion over the working height which affects the conductivity. The calibration factors shown in Table 5.3 identified by β_1 are based on all measurement steps.

Run nr.	200	205	243	249	270	
Date	14/02/22	15/02/22	16/02/22	17/02/22	18/02/22	
Wave Probe 1	β_1	25.83	25.06	25.02	25.49	24.93
	β_1^*	26.17	25.32	25.25	25.73	25.13
Wave Probe 2	β_1	31.11	29.95			
	β_1^*	30.56	30.15			

Table 5.3: Calibration factors (mm/V) are determined at the start of the day before the first run, β_1 states the calibration factor based on all measurements and β_1^* states the calibration factor optimized for the working height of the wave probe. Calibration of the waves is done on 15/02/22 and the actual runs were performed on 18/02/22

After the calibration procedure in the towing tank, the probe height is vertically adjusted so that the undisturbed water level is in the middle of the working range (100 mm). The usable working range during the runs is expected to deviate with ± 56 mm from the mean height of 100 mm based on the wave amplitudes ($= \frac{H}{2}$) stated in Table 4.5. The boundary heights of the wave probe are not used during the runs but these measurements have a significant influence on the regression to determine the calibration factor. Optimization of the calibration factor for the working range is possible by excluding measurements outside the working range. This is demonstrated for the calibration factor of wave probe 1 on Tuesday 15/02/2022 (run number 205). Solving Equation C.17 based on the measured voltage U and related vertical height Z of all 11 steps results in slope $\beta_1 = 25.06$ mm/V and intercept $\beta_0 = -70.91$ mm. As validation, the predicted heights \hat{Z} are calculated using Equation C.16 based on the determined regression parameters and measured voltages. The absolute residual $\epsilon = Z - \hat{Z}$ states the difference between the real and predicted height which is normalized by division of the total working height 200 mm $\epsilon_n = \frac{\epsilon}{Z_{total}}$. As shown in Table 5.4, the regression has a relatively low accuracy in the working range (-40 mm to -160 mm) and high accuracy at the boundaries. The calibration is improved by neglecting the measurements at the boundaries and only using the measurements within the working range for the regression. The results indicated with an asterisk, show increased accuracy within the working range and obviously more deviation at the boundaries, which is the trade-off that has to be made. This is illustrated with Figure 5.10, where the original residuals are shown in blue and the improved ones ϵ^* , represented in green have smaller deviations. The improved calibration factor β_1^* results in a higher accuracy of the surface elevation of 0.20 % instead of 0.43 % based on the entire probe height and an absolute error of 0.4 mm.

Relate wave probe to the model location

The wavemaker requires a harmonic steering signal, with a voltage as amplitude, to control the piston movement. The actual generated wave depends on the water depth z_ζ in the tank and steering input, unfortunately, a default mapping table of wave properties and steering input is not available. Wave frequency ω (and wavelength via the dispersion relation) is equal to the piston input frequency, while the wave height H depends on the horizontal displacement of the piston as a result of the received voltage. Iterations in the steering signal are required to generate the wave with the desired properties for the current setup.

During the calibration of the wave properties, both wave probes are installed. However, during the real runs, only the first probe is present. The second probe is used in the calibration to relate the measured elevation at wave probe one to the location of the model during the runs. The Item profile is moved towards the first wave probe after the calibration to be out of the field of view of the roof-mounted camera as shown in Figure 5.1.

During the calibration, the horizontal x -distance between the two wave probes is 7.00 m. A surface elevation ζ , measured at wave probe one ($wp1$), arrives Δt_ζ s later at the second probe ($wp2$), which is due to the linear wave group velocity c_g and the shift in horizontal x -position. The deep water assumption $\frac{\lambda}{2} < z_\zeta$ does not hold for wave 1 and therefore the group velocity is slightly bigger than $\frac{c}{2}$ based on Equation 2.6.

Step	Measurements		All steps			Steps within working range (4-8)		
	Z (mm)	U (V)	\hat{Z} (mm)	ϵ (mm)	ϵ (%)	\hat{Z}^* (mm)	ϵ^* (mm)	ϵ^* (%)
1	0	2.887	1.5			2.8		
2	-20	2.044	-19.7	-0.3	-0.16	-18.5	-1.5	-0.74
3	-40	1.210	-40.6	0.6	0.29	-39.6	-0.4	-0.18
4	-60	0.405	-60.8	0.8	0.38	-60.0	0.0	0.00
5	-80	-0.397	-80.9	0.9	0.43	-80.3	0.3	0.16
6	-100	-1.191	-100.8	0.8	0.38	-100.4	0.4	0.20
7	-120	-1.964	-120.1	0.1	0.06	-120.0	0.0	-0.01
8	-140	-2.747	-139.8	-0.2	-0.12	-139.8	-0.2	-0.10
9	-160	-3.540	-159.6	-0.4	-0.18	-159.9	-0.1	-0.06
10	-180	-4.340	-179.7	-0.3	-0.16	-180.1	0.1	0.06
11	-200	-5.135	-199.6	-0.4	-0.19	-200.3	0.3	0.13
				$\hat{\beta}_1$ (mm/V)	25.06	$\hat{\beta}_1^*$ (mm/V)	25.32	
				$\hat{\beta}_0$ (mm)	-70.91	$\hat{\beta}_0^*$ (mm)	-70.26	

Table 5.4: The measurement voltage U and corresponding height Z at each step are shown. Approximated values using linear regression based on all measurements are indicated by \hat{H} and improved regression within the working range is indicated with $*$. The normalized residuals ϵ_n is determined by dividing the absolute residuals ϵ by the working height 200 mm

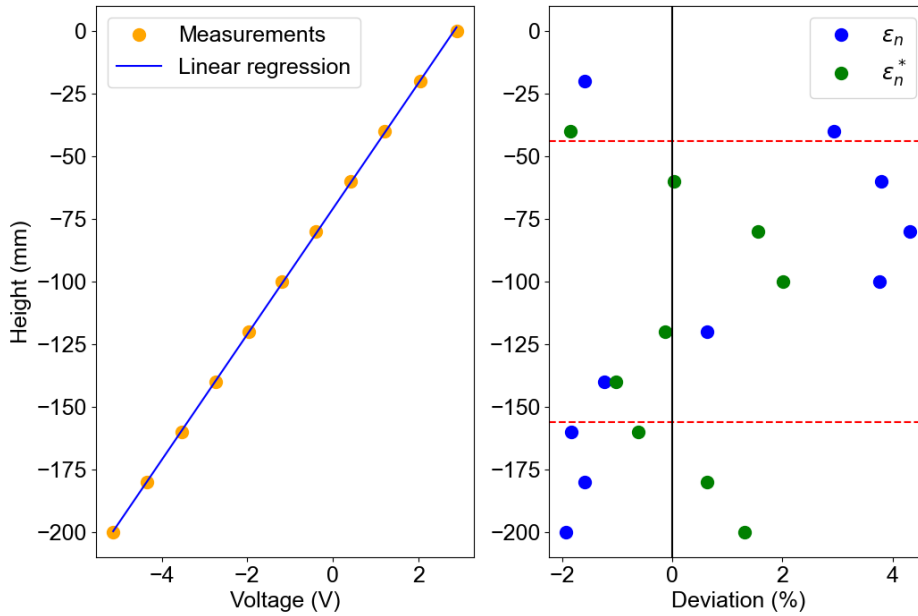


Figure 5.10: The left figure shows the linear regression with the blue line based on the measured values shown as orange dots. The right figure shows the normalized residuals ϵ_n for the regression based on all measurements in blue and the improved calibration within the working interval with the green dots. The dashed red lines indicate the vertical working height of the wave probe during the runs

$$\Delta t_\zeta = \frac{x_{probe_2} - x_{probe_1}}{c_g} \tag{5.8}$$

wave	Characteristics				Group velocity				Time shift			
	a_{wp1} (mm)	λ m	k (1/m)	steepness (-)	c_g (m/s)	$(ka_{wp1})^2$ (-)	c_g^* (m/s)	Δc_g (%)	Δt_{c_g} (s)	$\Delta t_{c_g^*}$ (s)	Δt_{manual} (s)	Δt_{ζ} (s)
1	0.057	2.845	2.21	0.040	1.107	0.016	1.116	0.7	6.32	-0.05	-0.27	6.00
2	0.024	1.264	4.97	0.039	0.703	0.015	0.710	1.0	9.96	-0.10	-0.29	9.57
3	0.012	0.681	9.22	0.035	0.516	0.012	0.522	1.2	13.57	-0.16	-0.01	13.40
4	0.010	0.509	12.36	0.039	0.446	0.015	0.453	1.7	15.71	-0.26	0.07	15.52
5	0.020	0.690	9.10	0.059	0.519	0.034	0.536	3.3	13.48	-0.43	-0.48	12.57

Table 5.5: Identified time shifts of the measured signal between wave probe 1 and 2 based on the measured amplitude a_{wp1} and frequency ω_{wp1} at wave probe 1 stated in Table 5.6

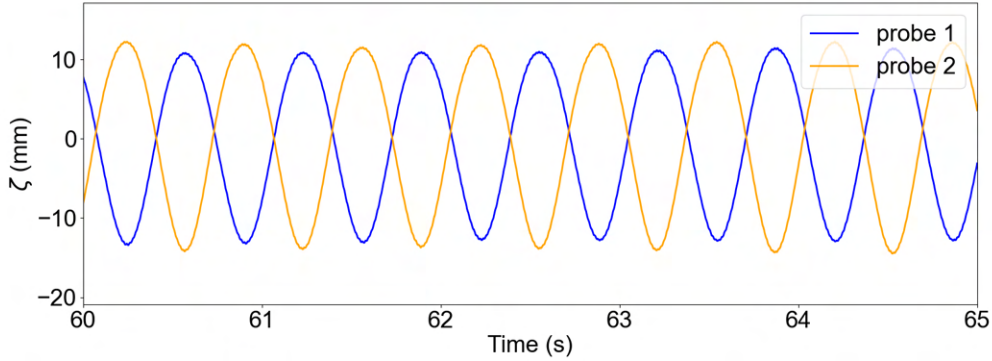


Figure 5.11: Surface elevation measured at both wave probes for wave 3 accounted for the calculated time shift Δt_{ζ} , still, an additional manual shift is required to have a zero phase shift indicated as Δt_{manual} in Table 5.6

This is a good indication of the time shift but there is still a phase difference visible between the two signals (for wave 3) in Figure 5.11. This phase difference is partly motivated by an extension of the group velocity. The used group velocity c_g stated in Equation 2.6 is valid for linear waves but the used waves in this experiment are classified as Stokes second order according to Figure 4.4. [21] states the group velocity for second-order Stokes results in a contribution of $O(k\zeta_a)^2$ compared to the linear wave celerity c . The nonlinear contribution increases the group velocity by a few % [15] as shown in Table 5.5 with c_g^* . The travel time between the two probes is reduced by $\Delta t_{c_g^*}$ and also the phase difference is reduced. However, still, a small phase difference is present and this is manually removed by introducing a small extra time shift Δt_{manual} .

This time-shifting procedure is necessary to properly compare equal parts of the signal at the two locations. The ramp-up is clearly visible in Figure 5.12 and the amplitude becomes more or less constant thereafter with respect to the absolute wave probe error of 0.4 mm. From the wave elevations measured at probes one and two, the amplitudes are determined by (sin) fitting the signal over an interval in the stable region indicated by the vertical green lines in Figure 5.12.

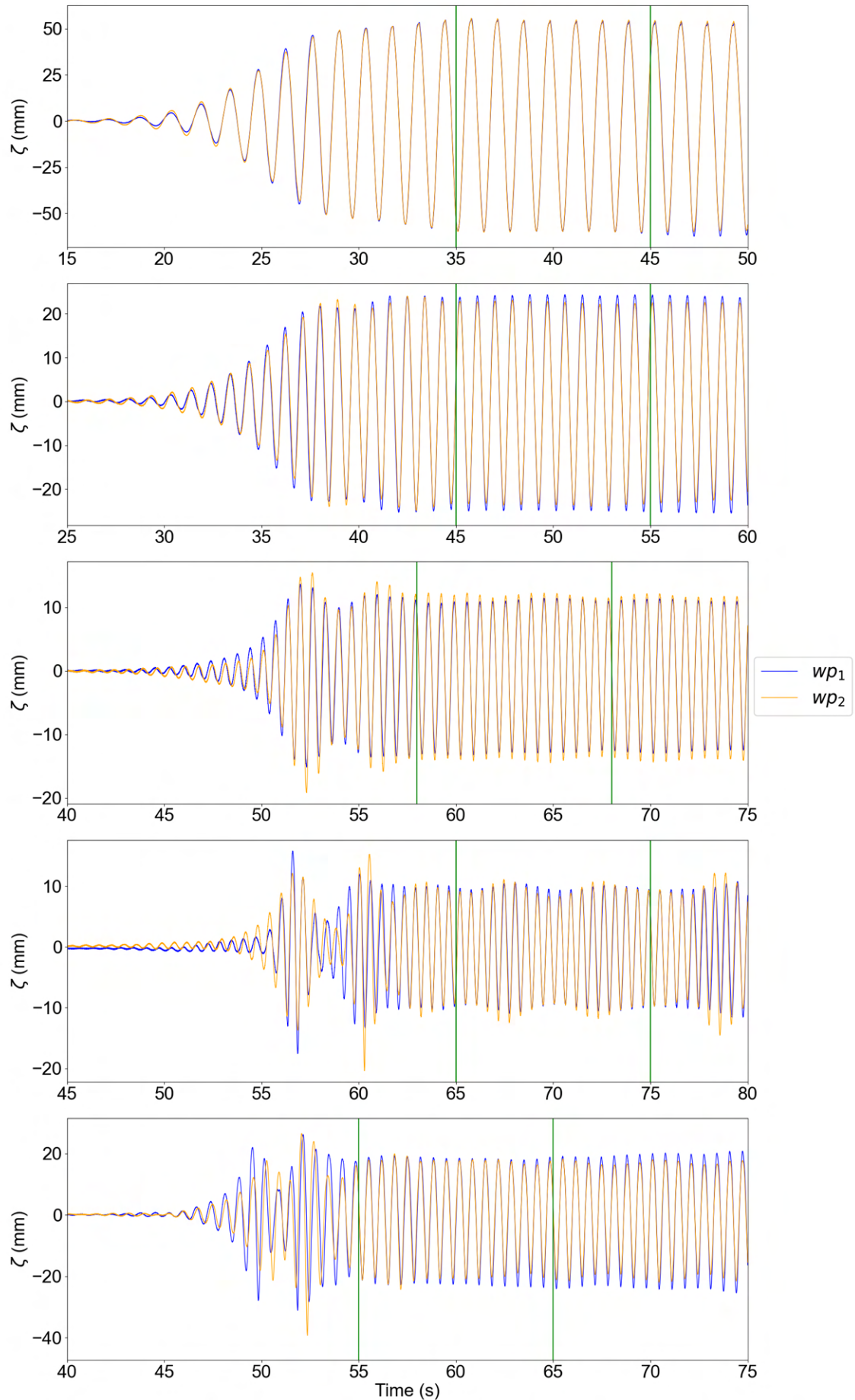


Figure 5.12: Surface elevation was measured at both wave probe locations from top to bottom: wave 1 - 5 where the blue line represents wave probe 1 and the orange line wave probe 2. The green vertical lines bound the interval where the amplitudes are fitted on

wave	Desired		Measured						
	a (mm)	ω (rad/s)	a_{wp1} (mm)	a_{wp2} (mm)	Δa		ω_{wp1} (rad/s)	ω_{wp2} (rad/s)	$\Delta\omega$ (%)
1	56.67	4.66	56.82	56.93	-0.11	-0.19	4.65	4.66	-0.06
2	25.00	7.01	24.38	22.90	1.47	6.04	6.98	6.99	-0.06
3	13.33	9.59	12.02	12.88	-0.86	-7.16	9.51	9.51	0.06
4	10.17	10.95	9.87	9.93	-0.06	-0.64	11.01	11.02	-0.07
5	21.67	9.59	20.37	19.04	1.33	6.53	9.45	9.42	0.32

Table 5.6: Desired wave properties are shown as well as the measured values at both probe locations

The amplitude measured at both probes deviates as shown in Table 5.6. This can not be ascribed to a wrong calibration factor because this should stretch the signal entirely (both peaks and troughs) which is not visible over the stable interval of the signals as shown in Figure 5.12. All runs are executed on the same day with an equal calibration factor over the runs determined at the start of the day. The calibration factor seems to be appropriate since wave 1 is fitted almost perfectly at both locations with a relative deviation of 0.19% and an absolute deviation of 0.19 mm which is within the absolute wave probe error margin of 0.4 mm. No clear trend can be extracted from the deviations over the two signals and therefore deviations can be ascribed to minor changes in wave characteristics that were developed during propagation from wave probe one to two. The elevations measured at probe one can be used at the location of probe two by taking the error present as $\pm\Delta a$ in Table 5.6 in account. For the next time, a third wave probe could have been used to validate. As noted, the wavemaker is more efficient in generating long waves such as wave 1 and less good at generating shorter waves such as wave 4. This is clearly motivated by the time signal of wave 4 where significant beating is visible within the 'stable' interval. The wavemaker is not able to produce entirely repeatable waves and this is in line with the expectations because $\lambda = 0.5$ m approaches the lower boundary of the wavemaker limit $\lambda = 0.4$ m.

6

Data processing

This Chapter describes how the different measurements are obtained and synchronized to be able to analyze the coupled hydrodynamic behaviour.

6.1. Drum motions

The motions of the drum in x, z -plane are captured by the camera placed beside the towing tank. No method or program ready to use is available to extract the displacement (x - and z -direction) and rotation (along the y -axis) from the recordings. Inspired by object tracking, a method is developed to determine the motions based on the videos. Markers are placed on the drum lid with a predetermined location during the experiment preparations. In contrast to the thin sheet, the drum is classified as a rigid body. Therefore, it is reasonable to assume the distance between points on the drum remains unchanged. Several locations on the drum lid should be simultaneously tracked in time to be able to determine the motions based on the known geometry between the markers.

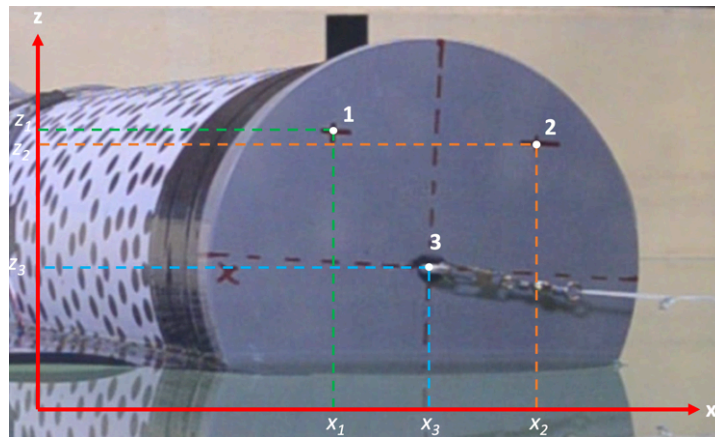


Figure 6.1: Markers 1, 2, 3 in the local defined camera axis system

The drum rotates around its center point (marker 3) which represents the horizontal (x) and vertical (z) displacement of the drum. Figure 6.2 visualizes the location difference of the markers in three frames during excitation. Markers 1 and 2 are used to determine the rotation ϕ , based on the difference Δ in x - and z - coordinates, using Equation 6.1. A left-turning rotation is positive according to Equation 6.1 where a right turning rotation has a negative sign.

$$\phi = \arctan \frac{z_2 - z_1}{x_2 - x_1} \quad (6.1)$$

The local coordinate system with incorporated distances (absolute difference in local coordinates) should be translated to real scale (mm). The measured distance between markers 1 and 2 is $l_{initial} =$

79 mm in reality. A scale factor is determined for every frame based on the length in the local coordinate system with the use of Equation 6.2. The time-dependent scale factor compensates for distortion of the frames, since the view angle changes when the drum moves within the local coordinate system.

$$scale = \frac{79 \text{ mm}}{\sqrt{(\Delta x)^2 + (\Delta z)^2}} \quad (6.2)$$

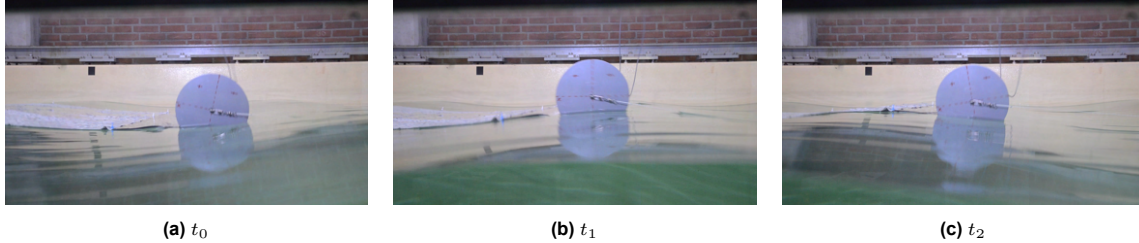


Figure 6.2: Visualization of change in location of markers on the drum lid shown for three (nonsuccessive) time steps

6.1.1. Object tracking

Hence, a program is developed based on the following requirements:

1. Track multiple predefined points over time with high accuracy
2. Allow partial occlusion of the object over successive frames
3. Handle large motions

To determine the location of objects from recordings, generally, either tracking or detection methods are used. In this case, tracking is preferred since it determines the location based on historical information, resulting in improved accuracy. It determines the location in the new frame with the knowledge of the previous locations, the traveling direction and the velocity. The user initializes the tracker by drawing a bounding box on the object which is treated as positive, automatically generated images outside the box are treated as false. The library 'Open Source Computer Vision' (OpenCV) available for Python, includes several methods to track objects such as BOOSTING, MIL, KCF, TLD, MEDIANFLOW, MOSSE and CRST [10]. The first tracker identifies the object in the new frame by evaluating pixels in the neighborhood of the previous frame, MIL and KCF are slightly optimized versions. TLD learns the object by the previous frames and is able to work with large motions and occlusion, but returns many false positives. MEDIANFLOW works only with small motions and no occlusion. MOSSE and CRST are both based on a correlation filter method where MOSSE is the fastest and CRST is slower but gains in accuracy [27]. Therefore, CRST turns out to be the best fit for tracking the points on the drum since it can handle unpredictable motions and some occlusion. The latter is important since not all frames have captured the markers sharply due to the high motions detected. Accuracy is of higher importance than speed since the analysis is only performed once instead of continuously. Especially for wave 1 the markers faded almost entirely in some frames as shown in Figure 6.3.

As previously mentioned, the written script allows multiple points to be tracked in a video initialized by drawing a rectangular box around the objects. If an object is lost during the tracking the script shows an error indicating the lost marker. The script allows initializing the tracker again by drawing a box around the object before proceeding. This is not preferred since manual re-initialization can lead to small errors in the tracked object. Except wave 1, all the other waves were tracked well without losing any of the three markers in time. Figure 6.4 is added to show the determined motions of the drum during the excitation of wave 2. The bottom sub-figure visualizes the scale factor, where the measurements in the local coordinate system are multiplied to determine the motions for the real scale. The orange line represents the ratio between the calculated length between markers 1 and 2 while using the scale factor and the initial length $l_{initial}$ (scaled by 0.5 for better visualization). This serves as a validation for the scale factor since the calculated length should not differ and be equal to $l_{initial}$ over time.

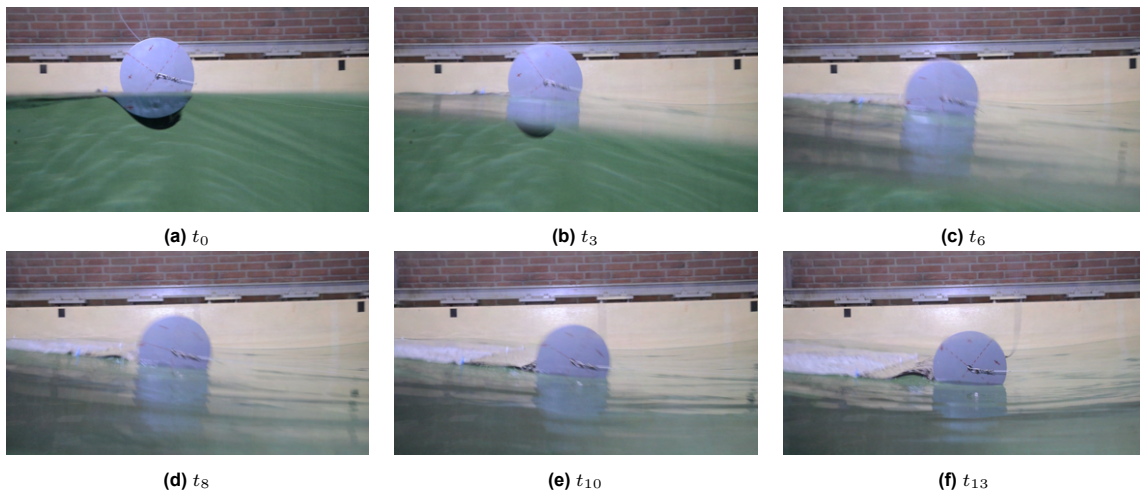


Figure 6.3: Example of occlusion of the markers in the frames of wave 1

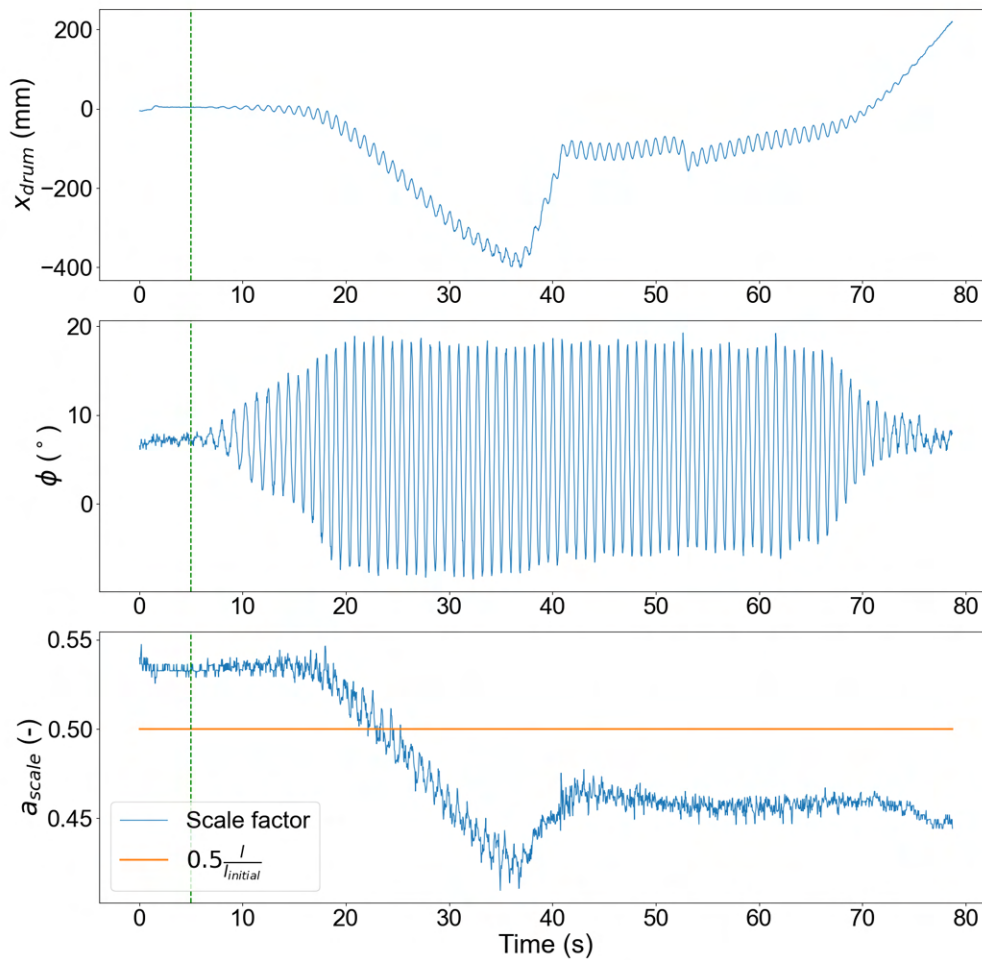


Figure 6.4: Motions are determined with the developed script based on object tracking. The bottom graph shows the required factor to scale the measurements to real scale, the orange line is added as a reference to show the calculated length between markers 1 and 2 in relation to the initial length

Due to the high velocities of wave 1, the markers become barely visible in some frames as mentioned before and is shown in Figure 6.3 where the tracker is not able to track the markers. This is tackled

by manually drawing markers at the points of interest in every frame with higher contrast as shown in Figure 6.5. The tracking performance is improved and this makes it possible to extract information about the motions of wave 1. Hence, the results are less accurate than for the other waves because manually drawing the markers in each frame is prone to slight errors in location (range of millimeters in the measurements). The magnitude and shape of the motions are well obtained which is important for the goal of this study to indicate the behaviour instead of determining the exact values.

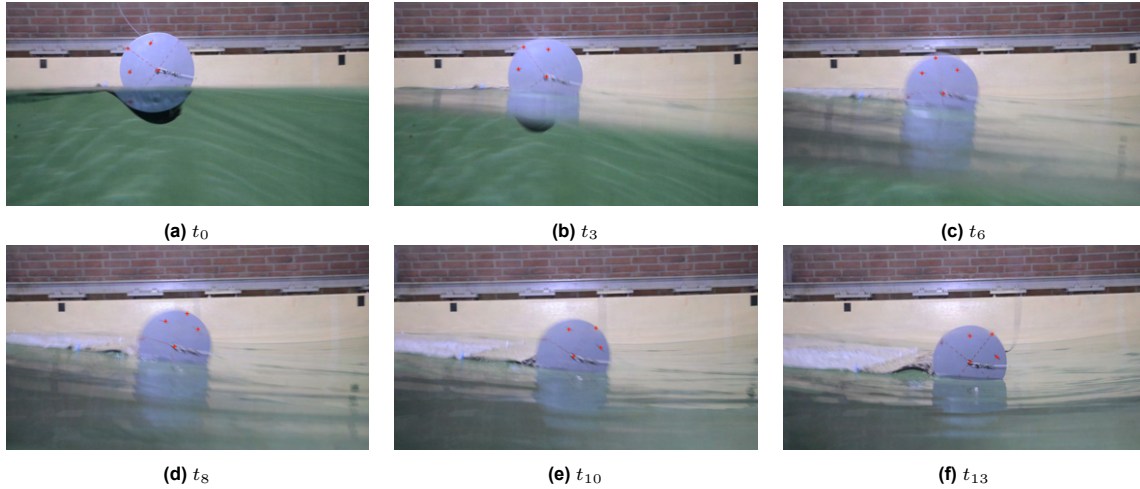


Figure 6.5: Occlusion of the markers for wave 1 is solved by manually drawing indicators (red crosses) on the points of interest

6.2. Measurements synchronization

Different equipment is used to measure the desired parameters, all with their own 'local' time frame. Mapping these signals into one timeframe is necessary to interpret the combined measurements at a time step. The flashing light and beeping sound of the light trigger are used to synchronize the different measurements in time. The time frame of the model t_{model} is a convenient choice as governing timeframe, since the end goal is to analyze the motions at the model location. For the remainder, 'wave probe' refers to the first wave probe since the second probe is removed after the calibration and is therefore not present during the runs. This implies that all measurements should be translated to the time frame at the model location.

- The force transducers located in the drum-sheet connection are measured in the governing time-frame t_{model} at the model location, with no translation required.
- The mooring force is measured at the center of the drum in the governing timeframe t_{model} at the model location, no translation is required.
- The surface elevation is measured at the location of the wave probe t_{wave} . The signal should be shifted in space to account for the difference in x -coordinate of the wave probe and model.
- The motions of the drum obtained from the recordings are measured in the local camera time frame t_{camera} . A timestamp present in both time frames should be used to map the local camera time frame into the governing one.

As mentioned above, the distance between the first wave probe and the initial location of the model is 6.64 m. A surface elevation ζ measured at the wave probe arrives Δt_{ζ} (s) later at the location of the model as introduced by Equation 5.8.

$$\Delta t_{\zeta} = \frac{x_{model} - x_{probe_1}}{c_g} \quad (6.3)$$

The synchronization of all measurements in different time frames to the governing time frame at the model location is demonstrated for wave 4. The surface elevation shown in Figure 6.6 is measured at the wave probe, and the orange line indicates the initiation of the light trigger in the governing time

frame t_{model} .

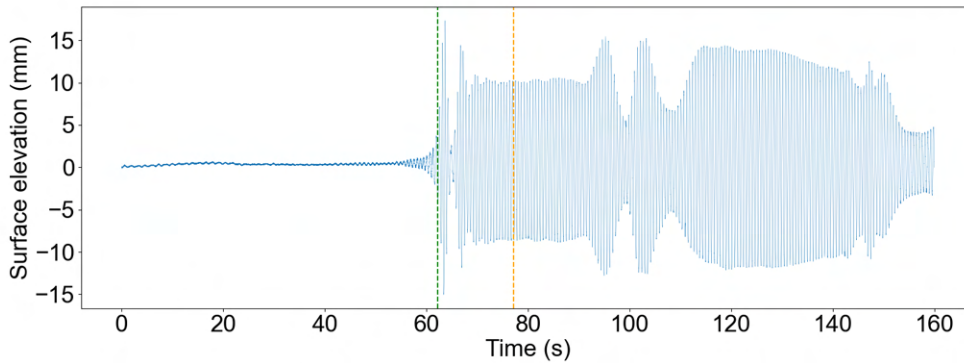


Figure 6.6: Surface elevation was measured by wave probe one over time. The orange line represents the initiation of the light bulb in t_{model} . The green line is the translated time of the wave probe signal to the initial model location by accounting for the difference in horizontal location Δt_ζ

The surface elevation measured by the wave probe should be shifted in time with Δt_ζ to translate the surface elevation to the undisturbed model location in the governing time frame t_{model} shown in Figure 6.7. Δt_ζ is the difference between the orange and green lines in Figure 6.6.

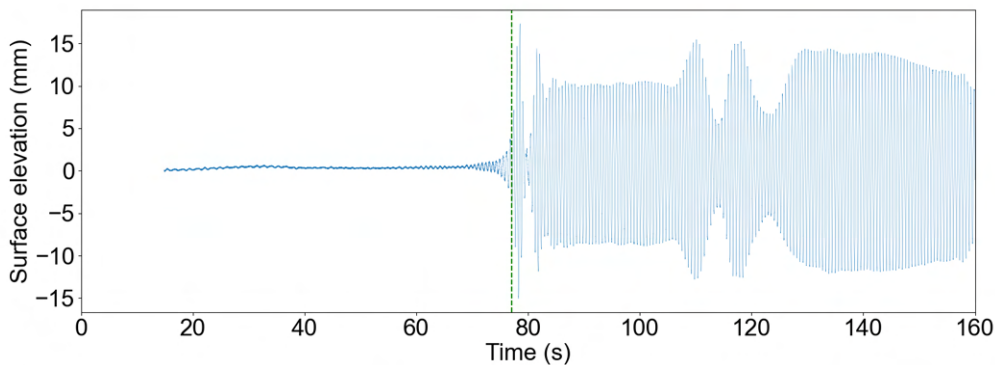


Figure 6.7: Surface elevation translated to t_{model} . The green line represents the initiation of the light trigger at the model location (and overlays the orange line in Figure 6.6)

The light trigger initiation time $t_{model,light}$ is known since the signal is received simultaneously with the wave probe signal at the data acquisition PC. The sound of the bulb is heard in the recordings made by the camera at the side of the towing tank at $t_{camera,light}$, which makes relating the local camera time t_{camera} to the governing time frame possible. This is done manually by detaching the audio signal from the video and indicating the time stamp of the frame where the trigger is initiated. The video is captured with 24 frames per second and the extracted time must be treated with an accuracy of $\frac{1}{2} \cdot \frac{1.00}{24} \approx \pm 0.02$ s. This is a reasonable error of 4% for the smallest period of the chosen wave of 0.57 s.

Stable interval

When the first wave excites the structure, the model starts to drift in a positive x -direction which further increases the distance between the wave probe and the model. Due to the velocity of the structure during the drift process, the period of the wave and measurement signal has slightly increased when looking from the model perspective (Doppler effect). This is checked by comparing the measurement signal of the force transducers (model perspective) during the drift process with the surface elevation measured at the fixed location of the wave probe. The slightly stretched period of the force transducer signal is visible in Figure 6.9, because the model has a horizontal velocity.

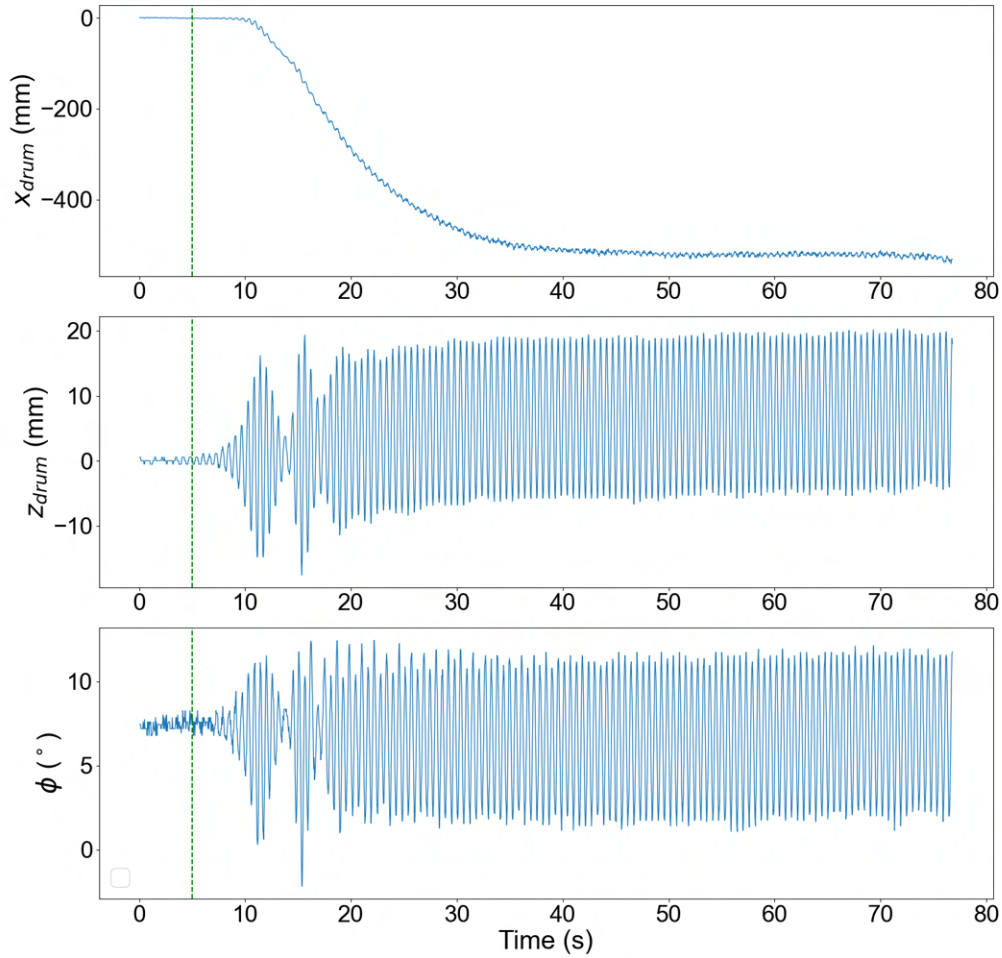


Figure 6.8: Motions of the drum in local camera timeframe t_{camera} with the green line indicating the start of the light trigger signal. From top to bottom: horizontal x -displacement, vertical z -displacement and rotation ϕ of the drum

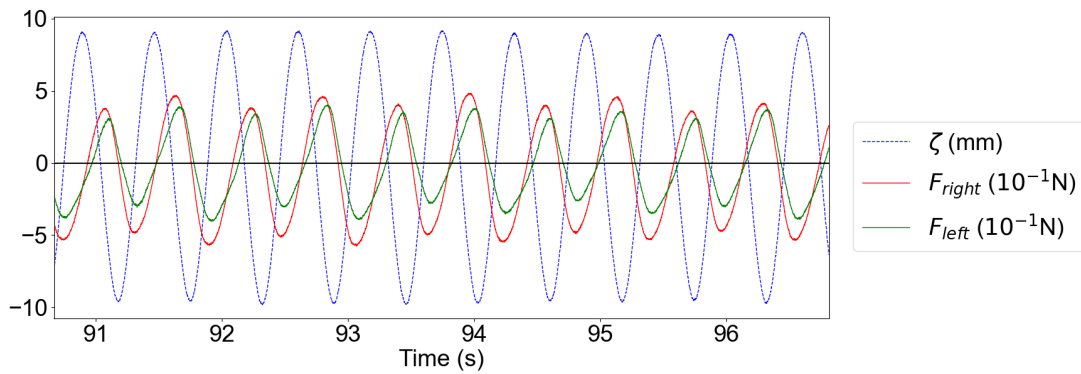


Figure 6.9: Slightly stretched period visible for the force transducers to the wave elevation

A few periods are sufficient to be able to analyze the structure's response, provided that the net structural horizontal velocity over one period equals 0 where the surface elevation is identical for a few successive oscillations. This motivates the importance of determining an interval, where the structure oscillates around a stable x -position. The structural response must be analyzed where the mean horizontal offset is stable over a time interval is shown in Figure 6.10 which is bounded by the orange lines. Not only the horizontal position must be stable, but the surface elevation should be approximately equal

over successive periods as well. The chosen interval $\Delta t_{plot} = 139 \text{ s} - 144 \text{ s}$ consists of regular waves according to Figure 6.11 and has a stable horizontal position according to Figure 6.10. The chosen interval for the hydrodynamic response analysis is visualized as the shaded area in Figure 6.11.

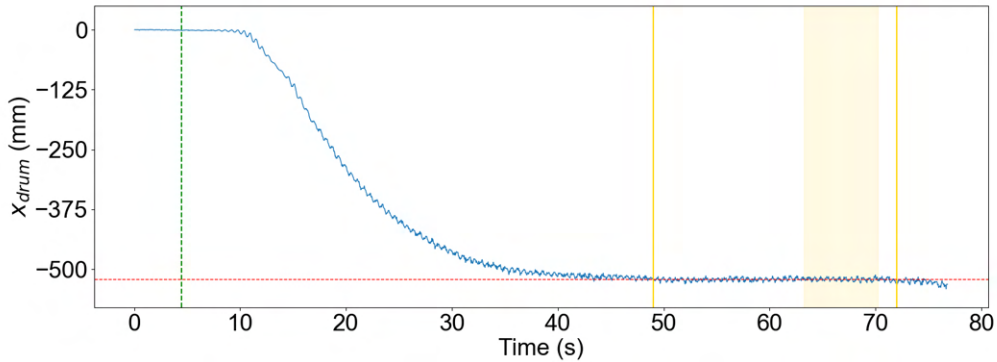


Figure 6.10: Horizontal x -displacement of the center point of the drum during excitation of wave 4 in the local camera time frame t_{camera} . The green line indicates the initiation of the light bulb. The orange line indicates the stable interval where the offset due to drift is constant. The shaded orange region represents the chosen interval for the analysis

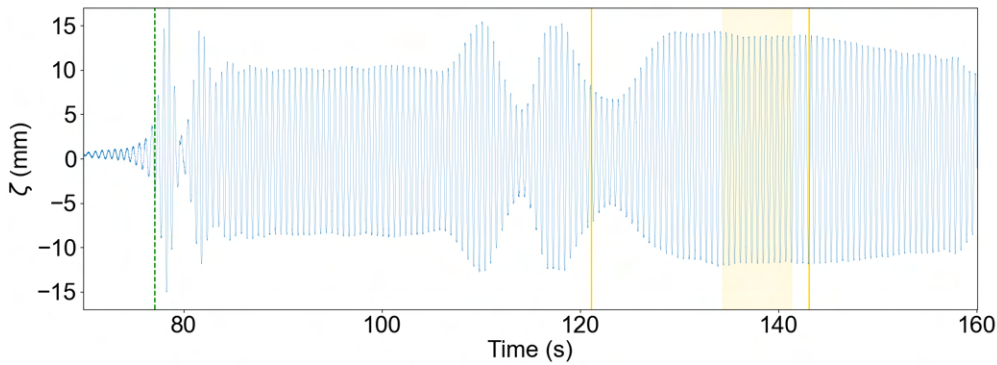


Figure 6.11: Surface elevation at the model location during excitation of wave 4 in the governing time frame t_{model} . The green line indicates the initiation of the light bulb. The orange line indicates the stable interval where the offset due to drift is constant. The shaded orange region represents the chosen interval for analysis

The change in x -coordinate of the model due to drift broadens the distance between the wave probe and the model as shown in Figure 6.12. It takes longer before measurements of the wave probe arrive at the model location. As stated in Figure 6.10 the shift in x -direction is 521 mm (horizontal red line) which introduces an extra time shift $\Delta t_{drift} = 1.2 \text{ s}$ according to Equation 6.3.

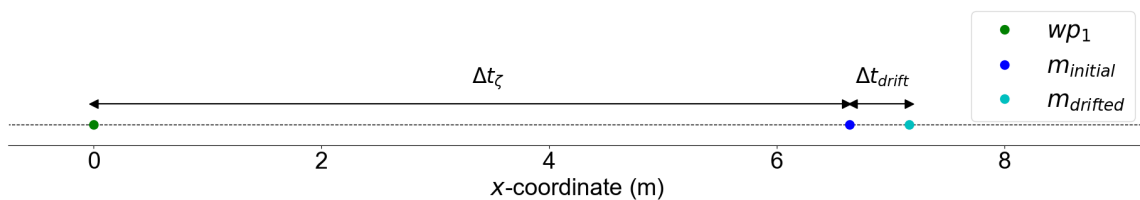


Figure 6.12: Visualization of the required time shifts to relate the measurements to t_{model} due to the difference in horizontal distance. $m_{initial}$ represents the initial location of the model, which is further increased due to drift indicated by $m_{drifted}$.

All three-time frames are visualized in Figure 6.13. A time measured in the local camera time frame t_{camera} can be translated to the governing time frame t_{model} using Equation 6.4. The corresponding surface elevation ζ should be translated with Equation 6.5 to match the model time frame t_{model} .

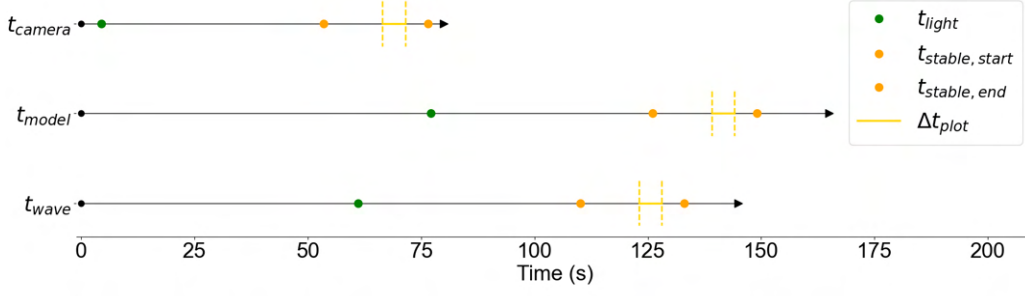


Figure 6.13: Visualization of timestamps in the different time frames demonstrated for wave 4. The interval where the drift force is stable is bounded by $t_{stable,start}$ and $t_{stable,end}$ as introduced in Figure 6.10, Δt_{plot} represents the chosen interval for the structure analysis.

$$t_{model} = t_{camera} - t_{camera,light} + t_{model,light} \quad (6.4)$$

$$t_{wave} = t_{model} - \Delta t_{\zeta} - \Delta t_{drift} \quad (6.5)$$

Mapping measurements within the interval

The wave properties may change during propagation and the model location could be slightly off compared to the calculations. Hence, the phase shift between the translated measurements based on the theoretically calculated time shifts does not perfectly match reality, as noted in the calibration of the waves (Section 5.4.3). The accuracy is further improved by manually identifying the phase shift of the different signals with the frames of the recordings. A manual time shift Δt_{phase} is introduced to align the measurements according to the manually determined phase shift. Figure 6.15 visualizes the surface elevation and structure motions over one period for wave 4 ($T = 0.57$ s). Time between successive time steps $\Delta t = t_{i+1} - t_i$ evolves with the step size of a frame 0.0417 s. In time step t_6 the surface elevation is maximal as well as the vertical displacement of the drum z_{drum} . A zero phase shift is determined based on the minimums in time step t_{13} . The accuracy of this method is proportional to the fps: $\pm \frac{1}{2} \Delta t$. This is illustrated for this case where the time of the maximum surface elevation t_{max} is determined in time step t_6 but the actual maximum can lay within $t_6 - \frac{1}{2} \Delta t < t_{max} < t_6 + \frac{1}{2} \Delta t$.

The vertical displacement of the drum is determined in the local camera time frame t_{camera} together with the rotation ϕ and horizontal x -displacement of the drum. Hence, the local phase difference between these parameters is included in the camera measurements. Either the measurements in the camera time frame or the measurements of the wave elevation should be shifted in time to align with the determined real phase shift. The translation from t_{camera} to the model time frame only depends on fixed times as shown in Equation 6.4 since both signals are obtained at the model location (no distance correction required). This implies that the measurements of the camera are related to the high accuracy (accuracy of $t_{model,light}$) which equals half the frame time step: $\frac{0.0417 \text{ s}}{2}$ to the model time frame with the phase shift incorporated. The biggest uncertainty is visible in the time shift Δt_{ζ} , since this shift depends on the difference in horizontal distance Δx and depends on the wave properties (c_g) as well. Hence, the extra time shift Δt_{phase} is introduced to the surface elevation signal t_{wave} to satisfy the (zero) phase shift obtained from the recordings, shown in Figure 6.14.

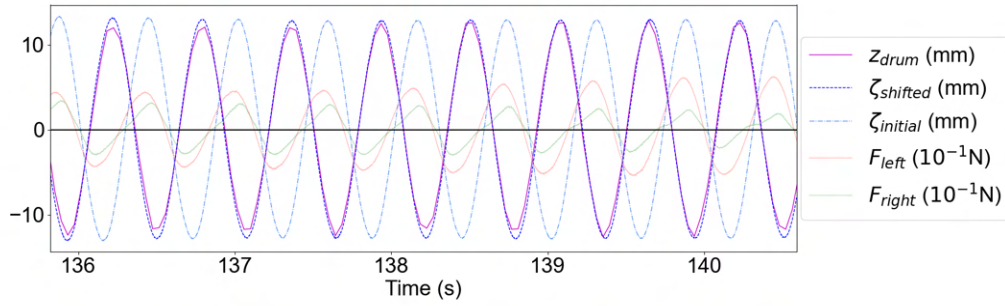


Figure 6.14: Initial signal of surface elevation $\zeta_{initial}$ and shifted signal $\zeta_{shifted}$ by $\Delta t_{phase} = -0.23$ s to mimic the real zero phase shift between ζ and z_{drum}

Due to the identified phase shift between z_{drum} and ζ and translating ζ by Δt_{phase} , all measurements in the local time frames are well mapped to the governing time frame t_{model} including phase shifts. The accuracy of the synchronized measurements is similar to the accuracy of the identified manual phase shift of $\pm \frac{0.0417 \text{ s}}{2}$. This suffices the goal of this study to indicate the behaviour and magnitude of the forces. Hence, it is less important what the exact values are as long as the relations between the measurements are well obtained. The synchronization procedure makes sure that all measurements are compared at the same time.



Figure 6.15: Visualization of wave and structure motion over one period excited by wave 4

6.3. Mooring force

For this study, the force in x -direction is the force of interest since the experimental setup represents a 2D-case with loading along the x -direction. The mooring design (angles) determines the contributions of the other directions to the line load. In the choice of the mooring configuration, the mooring lines are connected to the sidewalls of the towing tank where the model width does not equal the width of the tank. This results in angles with respect to the x -axis deviating from 90° as shown in the calculations below where $\theta_{x,y,z}$ is evaluated based on the mooring line geometry summarized in Table 5.1. The line force and direction are used to validate the measurements obtained with the 3D-sensor and the discussed calibration in Appendix C.

$$\theta_x = \arctan\left(\frac{\Delta y}{\Delta x}\right) = \arctan\left(\frac{0.55 \text{ m}}{5.15 \text{ m}}\right) = 6.1^\circ \quad (6.6)$$

$$\theta_z = \arctan\left(\frac{\Delta x}{\Delta z}\right) = \arctan\left(\frac{5.15 \text{ m}}{-0.12 \text{ m}}\right) = -88.7^\circ \quad (6.7)$$

$$\theta_y = 90^\circ - \theta_x = 83.9^\circ \quad (6.8)$$

The 3D-sensor generates a small voltage if no external load is applied which is considered as zero-measurement and is caused by gravity and pretension in the rods. This measurement is included in the calibration and therefore the predicted forces should equal to zero. The zero-measurement during the calibration without any applied load $F_z = 0.000 \text{ N}$, $F_y = 0.000 \text{ N}$, $F_x = 0.000 \text{ N}$ has output voltages $U_1 = -0.249 \text{ V}$, $U_2 = 0.541 \text{ V}$, $U_3 = -0.084 \text{ V}$ (run number 600) which corresponds to approximated forces $\hat{F}_z = -0.097 \text{ N}$, $\hat{F}_y = -0.009 \text{ N}$, $\hat{F}_x = -0.019 \text{ N}$. Hence, the zero-measurement changed slightly due to the movement of the sensor from the carriage car to the towing tank. The new offset in the towing tank is translated into forces and subtracted from the calculated forces during the runs to only visualize the contribution of the structure motions. During run 245 nothing was connected to the 3D-sensor placed in the tank and the mean output of the three sensors is used as offset. The output voltages are $U_1 = -0.205 \text{ V}$, $U_2 = 0.432 \text{ V}$, $U_3 = -0.320 \text{ V}$ and corresponding forces are $\hat{F}_z = 0.334 \text{ N}$, $\hat{F}_y = -0.159 \text{ N}$, $\hat{F}_x = -0.962 \text{ N}$. This offset is subtracted from the measurements, Figure 6.16 shows the measured forces during excitation of wave 1. In Figure 6.16 the static force F_{static} in the undisturbed situation ($\approx 0\text{-}30 \text{ s}$) is clearly distinguished from the drift force F_{drift} , visible as the plateau bounded by the two inclinations.

6.3.1. Measurement validation

During the calibration, loads are applied in similar directions as how the 3D-sensor is exposed during the runs, x, y -axis in a positive direction and z -axis in the negative direction. Therefore, the measured forces should be positive in the x, y -direction and should be negative in the z -direction. This contradicts the z -direction obtained from Figure 6.16, where the measured force F_z is positive in the undisturbed situation. During excitation (beyond 30 s) F_z declines whereas the force in x, y -direction increases over time. This is in line with the axis system since the mooring line pulls the 3D-sensor in a similar direction as during the calibration (negative z -axis and positive x, y -axis). This indicates that the static force is not measured well which is further motivated by the wrong direction of the line force.

The magnitude of the line force F_{line} is approximated with Pythagoras based on the contributions F_i in the three directions $i = x, y, z$.

$$F_{line} = \sqrt{\sum F_i^2} \quad (6.9)$$

The mooring line direction can be validated by calculating the angles based on the measured static forces in each direction and comparing these with the manually computed angles based on geometry. The mooring line angles are determined with Equation 6.10, this is based on the measured force contributions in each direction F_i and also in relation to the total line force F_{line} . These angles should be close to the angles of the initial mooring line geometry in the undisturbed situation $\theta_{x,y,z}$, since the change in angles during the runs is minimal. The maximal model displacement in x -direction is 1.24 m which results in small changes in angles ($\Delta\theta_x = -1.1^\circ$, $\Delta\theta_z = +0.2^\circ$, $\Delta\theta_y = +1.1^\circ$).

$$\theta_i = \arccos\left(\frac{F_i}{F_{line}}\right) \quad (6.10)$$

The angles based on the static forces visualized in Figure 6.16 $\theta_x = 42.0^\circ$, $\theta_z = 86.8^\circ$, $\theta_y = 48.0^\circ$ are not close to the initial angles. The direction of the static force F_{static} does not reflect reality and is not reliable. Hence, this force can not be obtained from the measurements. The (wrong) calculated static force is removed from the measurements by subtracting the mean F_i during the undisturbed situation (first 30 s for wave 1) to be able to only visualize the drift component $F_{i,drift} = F_i - F_{i,static}$ of the mooring force.

The drift force is validated based on the same principle as F_{static} in the opposite manner. The contribution of each direction to F_{line} is calculated based on the initial angles of the mooring configuration θ_i by accounting for the angle changes $\Delta\theta_i$ due to horizontal displacement. The magnitude of the line force is determined based on the angles shown in Equation 6.11 and should equal to F_{line} based on the three measurements without taking the direction in account as stated in Equation 6.11.

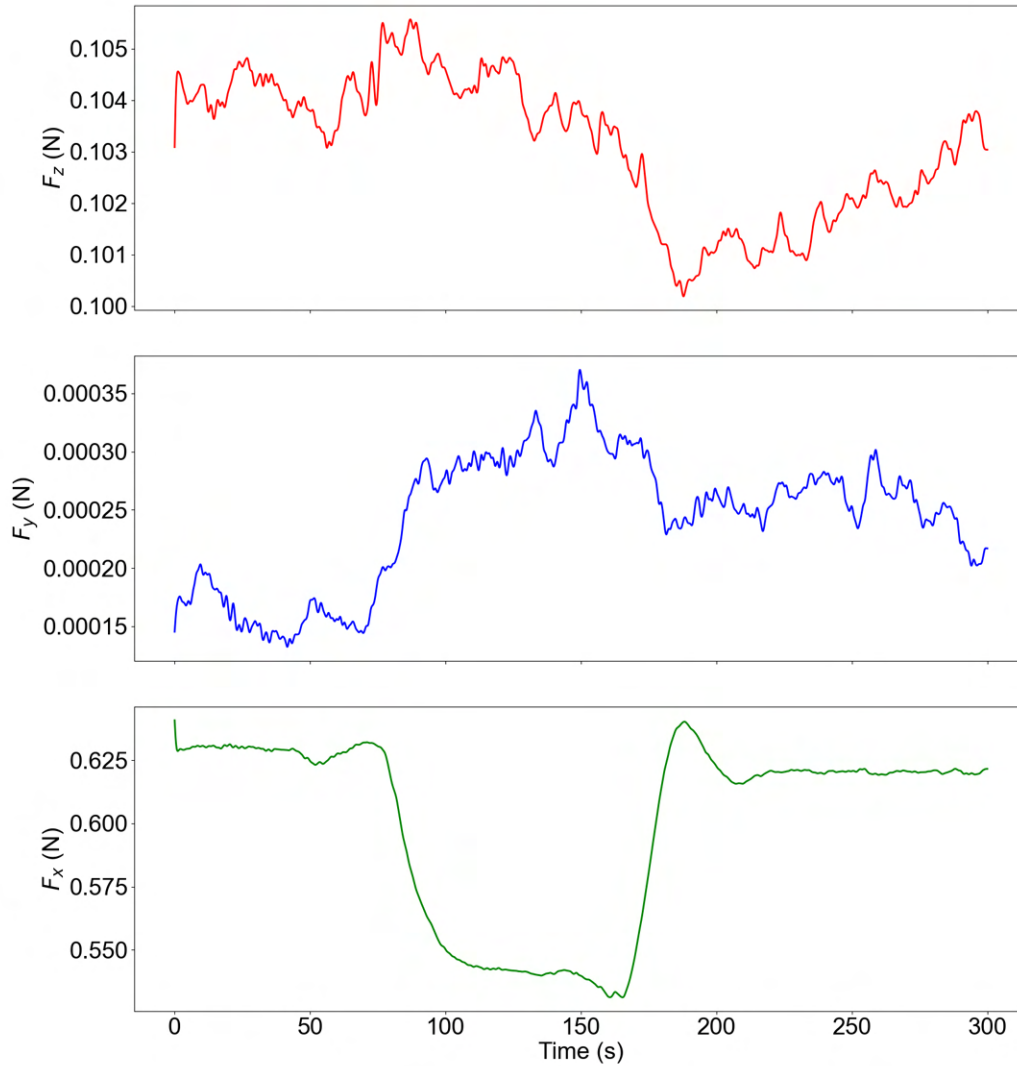


Figure 6.16: Forces measured in (top to bottom) z , y , x -direction during excitation with wave 3. Data filtered with a 3-pole low pass filter at $0.001 \times$ Nyquist frequency.

$$F_{line} = \sum F_i - F_{i,static} \cdot \cos(\theta_i) \quad (6.11)$$

As shown in Figure 6.17, the direction of F_{line} during excitation of the waves is within 1% for both methods in the displaced situation. This is motivated with the approximated calibration parameters B_0 and B_1 of the 3D-sensor. The sensitivity of the 3D-sensor relates to the change in voltages and also relates to the corresponding change in forces in each direction. All three individual sensors have a linear relation between applied force and output voltage, approximated by the slope with a linear regression. These slopes (sensitivity) for the 3D-sensor (B_1) are obtained with high accuracy ($\pm 0.36\%$ over the entire force range) due to the used amount of measurements in the calibration. The step size of the applied forces during the calibration is a factor 20 higher than the range of the measured mooring forces during this experiment. Hence, the approximated offset represented as B_0 in the calibration, has a big contribution to the calculated forces in the lower range of the 3D-sensor where the measurements do not result in a reliable approximation of F_{static} . The deviation in force from F_{static} during the runs is proportional to the (reliable determined) sensitivity of the sensors B_1 , and therefore F_{drift} is obtained within the same accuracy as the 3D-sensor $\pm 0.36\%$.

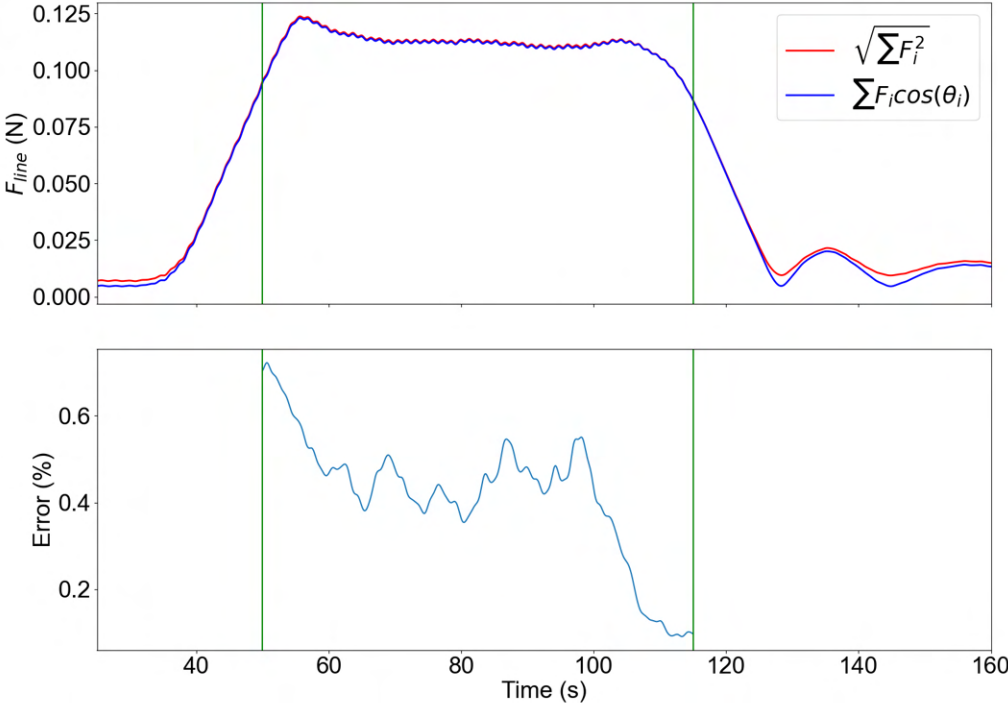


Figure 6.17: Mooring force F_{line} calculated using two methods (top), data filtered with 3-pole low pass filter at 0.001x Nyquist frequency. The relative error $\frac{\sum F_i \cos(\theta_i) - \sqrt{\sum F_i^2}}{\sum F_i \cos(\theta_i)}$ (bottom)

7

Results

The synchronization demonstrated for wave 4 in Chapter 6 is done for the other four waves as well. All the time shifts are initially calculated with the desired wave properties as stated in Table 5.6, to determine the stable interval for both the surface elevation and (horizontal) model position. Thereafter, the calculations are fine-tuned with the real wave properties based on the measured surface elevation at the wave probe.

7.1. Coupled hydrodynamic response

Figure 7.1 shows the surface elevation ζ together with the vertical displacement of the drum z_{drum} over the chosen stable interval. Figure 7.2 visualizes the two connection forces and is associated with the rotation over time, the surface elevation ζ is included as a reference.

The motions of the drum during excitation of waves 1, 2, 3 and 5 are not captured within the initial camera field of view. During wave 2 the camera positioned beside the towing tank is rotated to keep the drum within the view. The horizontal displacement can not be exactly determined anymore since the local coordinate system has a relative velocity with respect to the model motions during the rotation (similar to the Doppler effect on the measurement as discussed in Figure 6.9). During excitation of waves 1 and 5 the model moved out of the initial field of view. Hence, the camera is rotated to capture the stable interval where the structure has no resulting horizontal velocity over an oscillation. These recordings are still reliable since only the steady interval is of interest which is captured successfully. The local time t_{camera} is translated to t_{model} by the same procedure as described by Equation 6.4. The horizontal displacement is the last unknown required to be able to perform the measurement synchronization successfully. The roof-mounted camera captures the entire horizontal displacement within the camera field of view. The horizontal displacement is determined from those recordings by tracking a point on the drum with the same object tracking script used to track the markers at the side of the drum. It is not possible to track the markers of the recordings of wave 1 in the stable interval since the markers are not visible anymore. However, the few moments that the markers were visible during the drift process (due to the smaller distance to the camera) made it possible to use this interval to give an indication of the motions regarding wave 1. The frames were edited to cope with the faded markers to make the tracking possible as described in Section 6.1. During excitation of wave 3 the camera was still in the rotated position of the previous run (to capture the stable position of wave 5) and the model is only within the field of view for a limited interval, therefore, could be used for the analysis.

	a_{wp1} (m)	T (s)	ω (rad/s)	λ (m)	steepness (-)	c (m/s)	c_g (m/s)
wave 1	55.06	1.35	4.66	2.84	0.039	2.11	1.06
wave 2	24.99	0.90	6.97	1.27	0.039	1.41	0.70
wave 3	11.64	0.66	9.50	0.68	0.034	1.03	0.52
wave 4	12.78	0.57	10.98	0.51	0.050	0.89	0.45
wave 5	18.94	0.66	9.51	0.68	0.056	1.03	0.52

Table 7.1: Wave properties within the chosen interval with the use of sin fitting

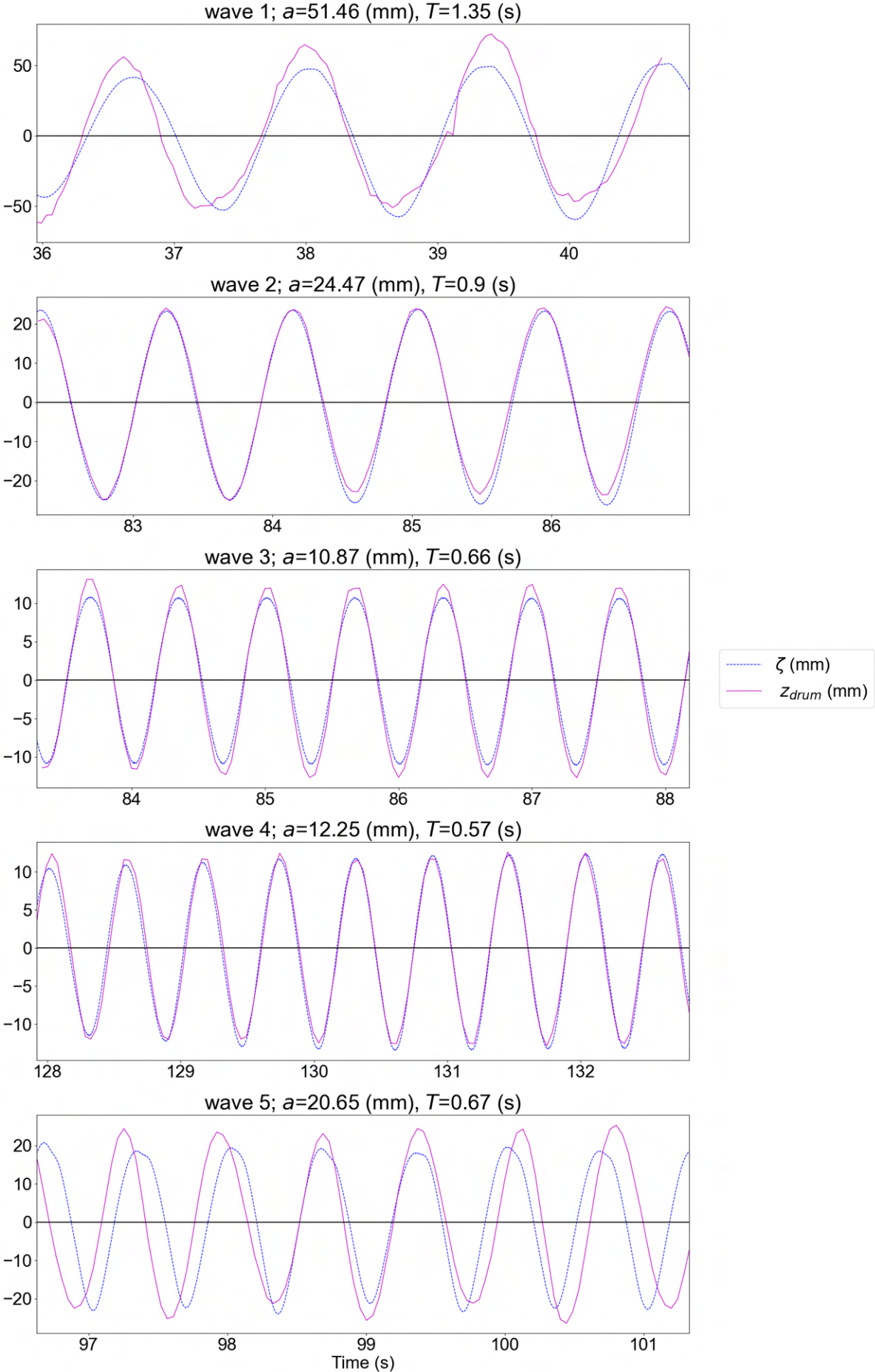


Figure 7.1: Vertical surface elevation ζ and the vertical drum motions z_{drum} of all waves.

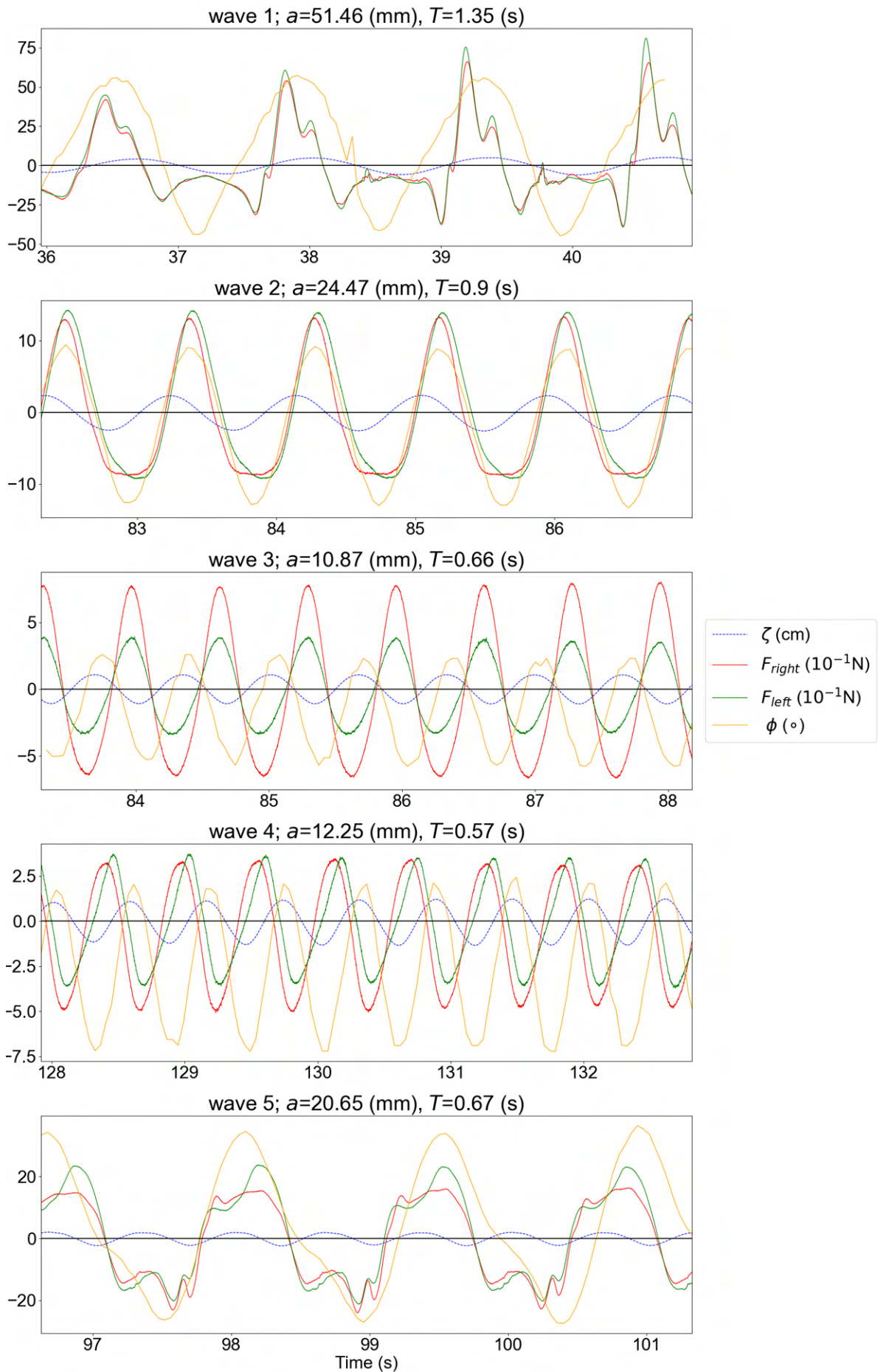


Figure 7.2: Rotation ϕ , connection force at both sides F_{left} , F_{right} and the surface elevation ζ is added as reference is

7.2. Mooring force

The static force can not be obtained from the measurements of the 3D-sensor but the pretension based on the elongation of the mooring lines is used as an approximation. The pretension is equal for all waves since this is determined based on the undisturbed situation. The model returns back to the undisturbed position after the excitation loading stopped. The static force present in the mooring line connected to the 3D-sensor $F_{static} = 0.10$ N as shown in Table 5.2.

The contribution in x -direction to the drift force F_{drift} is visualized for all waves in Figure 7.3. The measurements are averaged over the drifted interval indicated by the two inclinations to obtain F_{drift} for a wave condition. The average drift force is also determined for the interval where the motions are analyzed $F_{drift,plot}$ in Figure 7.2 and 7.1, bounded by the two orange lines. The mooring design is kept similar for both sides at the front and aft lines to assume the measured force with the 3D-sensor to be half of the total mooring force. Thereafter, the mooring force is multiplied by two, to estimate the total mooring force in Table 7.2. The measured forces are scaled to the real scale by $(\frac{1}{\alpha})^3$ which results in $F_{drift,real} = 5940$ N for the maximum measured force.

	F_{pre} (N)	F_{drift} (N)	$F_{drift,plot}$ (N)
wave 1	0.20	0.22	0.02
wave 2	0.20	0.10	0.10
wave 3	0.20	0.06	0.05
wave 4	0.20	0.12	0.12
wave 5	0.20	0.20	0.20

Table 7.2: Mooring force F_{drift} obtained from the experiment and $F_{drift,plot}$ is the averaged force during the analyzed interval in Figure 7.1 and 7.2.

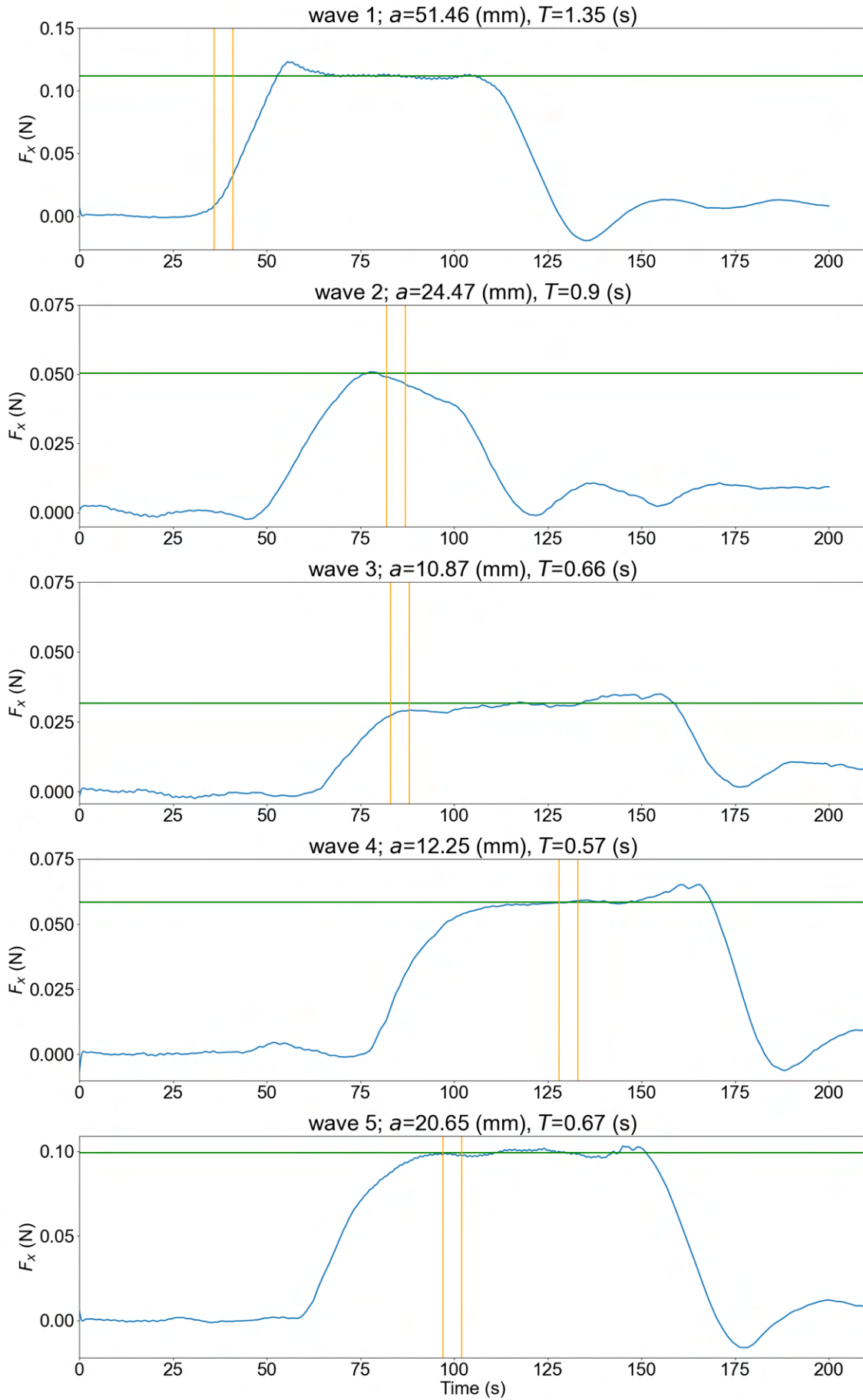
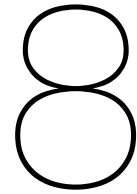


Figure 7.3: F_x contribution to F_{drift} of all waves during the runs with $F_{i,static}$ subtracted over the entire signal, filtered with a 3-pole low pass filter with $0.001 \times$ Nyquist frequency. The green line represents the mean value over the entire drifted interval, the orange lines bound the used interval for analyzing the motions in Section 6.2



Discussion

The designed concept on model scale is exposed to a variety of different waves, below some observations during the experiment:

- The model starts to pump water on the sheet if excited by the wave with the largest wavelength, this effects decreases for smaller wavelengths.
- The model starts to drift in positive horizontal direction at the start of the loading and moves toward a stable drifted horizontal location.
- The drum rotates heavily as response to the low frequency wave and mild rotations are observed for the higher frequency waves. These large rotations results in uplifting, followed by slamming of the thin sheet on the water around the vicinity of the connection.
- The heave motion of the drum mimics the wave elevation for all waves.

The vertical elevation of the drum z_{drum} , in comparison with the surface elevation ζ , indicates the amount of wave structure interaction. As shown in Figure 7.1, the z_{drum} almost mimics the surface elevation for all five waves and is in phase. Hence, for wave 5 the drum seems to have a bigger amplitude than the surface elevation. This can be ascribed to the nonlinear effects of the steeper wave, resulting in a change of wave characteristics over the traveled distance between the wave probe where ζ is measured and the model where z_{drum} is determined.

The surface elevation is measured at two locations during the calibration. Especially, for the high frequency waves, the deviation between the two wave probes could be up to 7 % without a clear trend according to the calibration. During the experiment only one wave probe is present and therefore the time signal can not be validated with another wave probe. The measured surface elevation at the probe is translated to the model location and used for the analysis. The real encountered surface elevation at the model location can differ from the used measurement of probe one due to nonlinearities of the wave. Adding an extra wave probe right before the structure during the runs tackles this uncertainty. The reflections of the model are expected to be small assuming that the structure follows the excitation motion and consequently the signal will be reliable. Nothing can be said about energy transfer to the structure because the wave properties are only measured at one location. In case the wave properties are measured at a location behind the model during the runs, these can be compared to the wave properties measured before the model. If the amplitude decays and the wavelength remain equal, this indicates the wave energy is reduced and transferred to the structure.

The motions show significant rotations during excitation which is in line with the observations. The rotations are the biggest for the longest and highest wave (wave 1). The rotations are in phase with the surface elevation for wave 1 and 4, where a slight phase difference occurs for waves 2 and 3 although all periods are similar to the excitation period. The steeper version of wave 3 (wave 5) shows a slower varying rotation ($\approx 2 T_{wave}$) than the excitation period and has a (five times) bigger amplitude than the observed rotation for the less steep wave. The structure is not able rotate in phase with the excitation motion of the waves. This contradicts the measurement of the vertical elevation where the structure is able to follow the excitation frequency. The rotation is not only influenced by the wavelength but also the combination of amplitude and wavelength, the steepness, seems to be important.

8.1. Understanding the coupled hydrodynamic behaviour

To understand and be able to explain the observed effects, the interaction around the connection is discussed. First, the contributions to the drum motions are evaluated and the corresponding effects while the sheet is connected. Thereafter, the measurements of each wave are evaluated at certain time steps. Finally, considered is how the motions can be modified by adjusting the design parameters.

8.1.1. Drum without the sheet

The equation of motion (EoM) of the drum without the sheet helps to understand the influence of the thin sheet on the combined motions. The structure is excited by the wave force F_{wave} . The terms influencing the heave and roll motions are determined and the additional terms due to the coupling of the sheet are discussed in the next section motivated by calculation methods to quantify the forces.

Heave

The similarity in amplitude, frequency and phase of the heave motion and surface elevation obtained from the measurements indicate that the model follows the wave motions. Hence, this states that the stiffness term is governing in the response and the heave natural frequency of the system is bigger than the excitation frequency. The hydrostatic restoring force is big enough to keep the system in position. This shows that the wavelength $\lambda_{min} = 0.51$ m is bigger than the structural length of the drum $D_{drum} = 0.16$ m which is in line with the rigid body motion shown in Figure 2.2. In case multiple wavelengths fit in the structural length, a rigid structure is not able to follow the excitation motions and significant wave energy will be transferred to the structure resulting in bigger loads.

The heave motion z_{drum} is limited by the restoring force $k_3 = A_{wl}\rho_w g$, where A_{wl} represents the waterplane area of the drum. The heave motion generates outgoing waves which represent the wave-making damping c_3 in the EoM and water must be displaced to move the drum vertically represented as the added mass a_3 . The EoM for heave of the drum is stated in Equation 8.1.

$$(m_{drum} + a_3)z_{drum}'' + c_3 \cdot z_{drum}' - k_3 \cdot z_{drum} = F_{wave} \quad (8.1)$$

Roll

The restoring moment of the roll motions depends on the change in horizontal distance of the CoG during a rotation and the mass of the structure. The horizontal shift depends on the rotation angle ϕ , and depends on the vertical distance between CoG and the point of rotation (metacentric height) indicated by GM . For a circular cross section, the rotation point is located in the circle center. Therefore, the metacentric height does not depend on the rotation angle and is determined by the vertical distance between CoG and the drum center. The change in horizontal distance of CoG is $GM \cdot \sin(\phi)$ which may be simplified to $GM \cdot \phi$ for small angles. The equation of motion describing the roll motion is formulated in Equation 8.2.

$$(I_{yy} + \delta I_{yy})\ddot{\phi} + c_4(\phi)\dot{\phi} + m_{drum}gGM\phi = \sum M \quad (8.2)$$

Where the sum of the moments is determined around CoG , $c_4(\phi)$ represents the damping, I_{yy} represents the roll moment of inertia and δI_{yy} the additional moment of inertia due to the surrounding fluid.

Both the mooring force and wave force contribute to the rotational moment. The resulting wave force points through the center of the drum (hydrostatic pressure works perpendicular to the circumference). The mooring line is connected at the center of the drum and the mooring force acts through the center. Both forces have a lever arm r with respect to CoG and contribute to the overturning moment. For a circular cross section no additional water should be displaced during the motion and the additional moment of inertia $\delta I_{yy} \approx 0$. The damping $c_4(\phi)$ due to resistance around the circumference of the surrounding water (and air) is negligible and no considerable wave-making damping is present for the roll motion. The roll structural moment of inertia I_{yy} provides resistance to angular accelerations of the model as shown in the EoM for roll in Equation 8.3.

$$I_{yy}\ddot{\phi} + c_4(\phi)\dot{\phi} + m_{drum}gGM\phi = F_{wave} \cdot r_{wave} + F_{mooring} \cdot r_{mooring} \quad (8.3)$$

8.1.2. Influence of the sheet

The influence of connecting the sheet to the drum is discussed in the section. In the undisturbed situation, the submerged part of the sheet results in a net buoyant force, proportional to the difference in density of the sheet and the water and the submerged length. The submerged length is determined by the initial horizontal CoG position compared to the position of the connector at the drum circumference. The upward force of the sheet introduces a moment around the center of the drum, which is balanced by a shift in horizontal CoG distance due to an initial rotation of the drum. This leads to an increase in the hydrostatic stiffness for heave k_3 due to the submerged sheet. Significant extra water around the sheet should be displaced to move vertically, leading to an increase in a_3 and wave-making damping c_3 too.

During excitation, the sheet is directly connected to the drum and a rotation of the drum must be followed by the sheet. This leads to a reaction force in the connection, which generates a moment with respect to the model CoG proportional to the connection location $r_{connection}$. The fluid around the submerged sheet should be displaced in order to follow the drum motions, represented as an increase of δI_{yy} and damping $c(\phi)$ [33]. The EoM for roll of the coupled system, with the sheet connected to the drum, must incorporate these effects.

$$(I_{yy} + \delta I_{yy})\ddot{\phi} + c_4(\phi)\dot{\phi} + \nabla GM\phi = F_{wave} \cdot r_{wave} + F_{mooring} \cdot r_{mooring} + (F_{connection}) \cdot r_{connection} \quad (8.4)$$

8.1.3. Evaluating effects on the motions

The terms of the coupled EoM for the roll and heave are known. Hence, the magnitude of the forces and the associated arm determine the influence of the motions. The reasoning behind the formation of the forces and effects is discussed to evaluate the contribution for each wave in the next Section where the measurements are analyzed. The connection force, mooring force, and wave forces are elaborated as well as the influence of damping.

Connection force

Hence, it is worth evaluating the directions of the forces since this will help to interpret the measured forces by the force transducer. In-plane forces are fully measured by the force transducer since the sheet is connected in a clamped way to the force transducer. The force transducer only measures the force in the inline direction and is not sensitive in the orthogonal direction. This is illustrated by the (upward) buoyancy force of the submerged part of the sheet in the undisturbed situation. Initially, the force transducer is almost fully horizontal oriented with an angle $\alpha = 85^\circ$ to the vertical buoyant force as shown in Figure 8.1. The measured part of the upward force F depends on the angle α as stated by Equation 8.5.

$$F_{measured} = F \cdot \cos(\alpha) \quad (8.5)$$

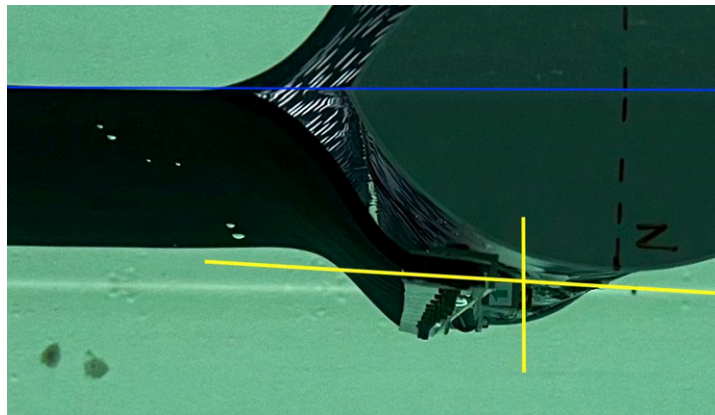


Figure 8.1: The initial angle of the force transducer without excitation. The blue line indicates the free water surface, added to identify mirror effects.

A rotation of the drum requires a change in the length of the sheet underwater. Therefore, the orientation (and measurement) direction of the force transducer changes continuously. The sheet can follow the rotation by in-plane elongation (dependent on the axial stiffness) and/or by submerging an additional length of the free-floating sheet. A positive rotation (left turning) requires an increase in the submerged length of the sheet and a negative rotation must decrease the submerged length. Figure 8.2 visualizes the submerged length of the sheet during a rotation for a large wavelength (wave 1) and for a shorter wavelength (wave 2) with equal wave steepness. A low axial stiffness EA would lead to small forces in the connection since the sheet hardly resists elongation. Hence, the thumbtack (indicated by the orange box) in Figure 8.2 shows significant horizontal displacement for both waves. This indicates that the sheet follows the rotation by submerging an additional length of the free-floating sheet Δl instead of elongating. This implies the thin sheet has a nonnegligible axial stiffness. However, both options are evaluated to be able to explain the measured connection force.

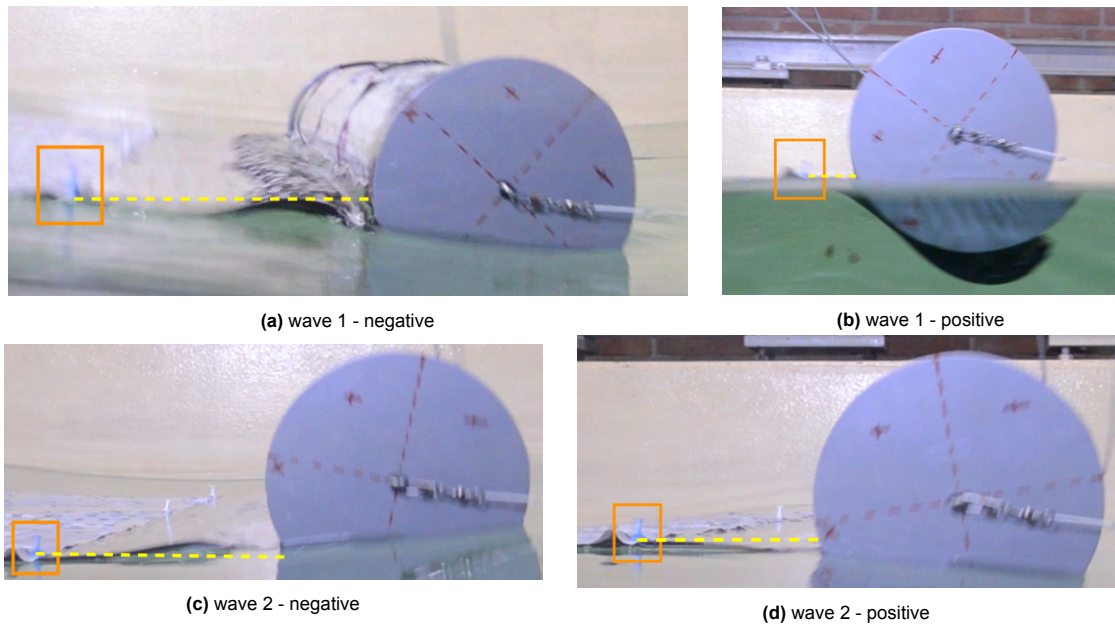


Figure 8.2: Change in submerged length of the sheet (dashed yellow line) indicates the maximum positive and negative rotation during excitation of wave 1 (a,b) and wave 2 (c,d)

Elongation

The increase in submerged length can be realized by an elongation of the sheet proportional to the axial bending stiffness $EA \approx 2800 \text{ N}$ with $E = 560 \text{ kPa}$ and $A = B \cdot h$. The increase in length Δl is proportional to $\epsilon = \frac{F}{EA}$, and the structural length $L = 4.95 \text{ m}$ as shown in Equation 8.6. This turns out 5.8 N axial force (in-plane direction) is required to elongate the sheet one centimeter in length.

$$F_{\text{elongation}} = \frac{\Delta l}{L} EA \quad (8.6)$$

Submergence

In order to submerge the additional length of the free-floating sheet, the model must overcome the buoyant force of the submerged sheet (upward), the force due to the acceleration of the free-floating sheet (in-plane) and the friction force (in-plane).

The buoyant pressure depends on the difference in density of the water $\rho_w = 1000 \text{ kg/m}^3$ and the sheet $\rho_{\text{sheet}} = 140 \text{ kg/m}^3$, the width of the sheet $B = 1.02 \text{ m}$ and the structural height $h = 0.005 \text{ m}$. A downward force of 0.422 N is required to increase the submerged length by one centimeter according to Equation 8.7.

$$F_{\text{buoyancy}} = h(\rho_w - \rho_{\text{sheet}})g \cdot \Delta l \cdot B \quad (8.7)$$

The increase in submerged length Δl requires the free-floating sheet to move horizontally. This movement results in an additional force $F_{a,sheet}$ proportional to the acceleration of the sheet. The added mass is negligible [12] due to the low draft and $h \ll B$. The acceleration of the sheet is assumed to equal the acceleration of the connection $a_{connection}$, which is approximated based on the second time derivative of the rotation ϕ stated in Equation 8.10.

$$F_{a,sheet} = (m_{sheet} + m_a) \cdot a_{connection} \quad (8.8)$$

$$m_{sheet} = B \cdot L \cdot h \cdot \rho_{sheet} \quad (8.9)$$

$$a_{connection} = r_{connection} \cdot \ddot{\phi} \quad (8.10)$$

$$\frac{\delta^2 \phi}{\delta t^2} = \frac{\delta^2}{\delta t^2} \zeta_\phi \cdot \sin(\omega t) = -\zeta_\phi \omega^2 \sin(\omega t) \quad (8.11)$$

Where ζ_ϕ represents the rotation amplitude and the double dot above ϕ represents the second time derivative resulting in the angular acceleration of the drum.

Froude scaling is chosen for this experiment with the trade-off that viscous effects are not scaled well. This implies that friction forces are bigger at model scale than at full scale. Due to the rotation, the entire floating sheet gets a horizontal velocity which leads to skin friction. Hence, frictional forces require time (and length) to develop and the motion in this experiment has an harmonic behaviour with small periods. Therefore, the velocity changes continuously and switches direction quickly which means that the boundary layer can not develop. Still an approximation based on the maximum velocity in the connection according to Equation 8.12, is relevant to determine the potential contribution to the connection force.

$$u = \frac{\delta \phi}{\delta t} = \frac{\delta}{\delta t} \zeta_\phi \cdot \sin(\omega t) = -\zeta_\phi \omega \cos(\omega t) \quad (8.12)$$

The maximum velocity is obtained at $t = 0$ s or $t = \frac{1}{2}T$ resulting in $u = \zeta_\phi \omega$ (m/s). It turns out wave 1 has the biggest velocity of all waves during the rotation $u = 0.37$ m/s based on the rotation shown in Figure 7.2. The friction force $F_{friction}$ is calculated using Equation 8.13.

$$F_{friction} = \int_A c_f \frac{u^2 \rho_w}{2}, dA \quad (8.13)$$

where u represents the flow velocity (m/s), $A = B \cdot L$ the horizontal surface and the friction coefficient c_f dependent on type of flow described by $Re = \frac{u \cdot L}{\nu} = \frac{0.36 \text{ m/s} \cdot 5.00 \text{ m}}{1.054 \times 10^{-6} \text{ m}^2/\text{s}} \approx 10^6$ with the kinematic viscosity of water $\nu = 1.054 \times 10^{-6} \text{ m}^2/\text{s}$ at a tank temperature of 18°C . Turbulent flow is expected where $c_f = 0.003$ which results in $F_{friction} = 1.08 \text{ N}$ [5] which is 7% of the measured force in the connection during wave 1 (14.6 N). The actual friction force will be lower since the boundary layer needs structural length to develop. This can not happen due to the oscillating motion where the velocity changes direction continuously. On full scale c_f will be even smaller due to the higher Reynolds number resulting in a smaller friction force. Hence, the friction force has minimal influence on the rotation on model scale and is therefore neglected.

Wave force

The model is excited by the wave force which is characterized by the wave properties represented in the surface elevation ζ described in Equation 8.14. The wave pressure generates a force around the drum circumference which initiates the heave motion (vertical direction) and rotation (moment around CoG). Pressure acts perpendicular to the drum circumference and points through the center of the circular drum. Hence, the moment generated around CoG is calculated by integrating the moment contributions around the circumference.

$$\zeta = \zeta_a \cos(kx - \omega t) \quad (8.14)$$

The wave pressure consists of a hydrostatic and a dynamic part. The hydrostatic part is equal over the horizontal drum diameter and does not generate a moment around CoG . The dynamic part of the wave pressure varies over time and generates a moment around CoG , which is visible as the inclination of the water surface. The wave pressure, based on the linearised Bernoulli equation with potential theory, is used to analyze the influence of the propagating wave shown in Equation 8.15 [22]. This is reasonable since the wave steepness is small and consequently the nonlinear contributions are negligible.

$$p(x, z) = -\rho_w g z + \rho_w g \zeta_a \frac{\cosh k(z_\zeta + z)}{\cosh k z_\zeta} \cos(kx - \omega t) \quad (8.15)$$

The wave force is determined by integrating the pressure over a surface and the moment follows from the force multiplied with the lever arm r_\perp . Integrating all the contributions over the wetted circumference of the drum results in the total moment.

$$\int_{S_{wetted}} p(x, z) r_\perp dA \quad (8.16)$$

However, integrating around the circular circumference is challenging. The x, z -coordinates at the circumference of a cylinder with radius $r = 0.08$ m are described by Equation 8.17.

$$r^2 = z^2 + x^2 \quad (8.17)$$

The horizontal drum coordinate ranges from $x = 0.08$ m to $x = -0.08$ m where $x = 0$ lays within the drum center. The corresponding z coordinate based on the x -position follows from Equation 8.17 as $z = -\sqrt{r^2 - x^2}$. All force contributions around the circumference act through the drum center $x = 0$. However, the lever arm varies with respect to CoG for each contribution. Since the perpendicular distance between the working direction of the force contribution and CoG determine the contribution to the moment. Based on the (absolute) x - and z - coordinates, the angle of the force with respect to the horizontal is known using $\alpha = \arctan \frac{x}{z}$. The directional force F can be split into the horizontal F_x and vertical F_z component.

$$\begin{aligned} F_x &= \sin(\alpha) \cdot F \\ F_z &= \cos(\alpha) \cdot F \end{aligned} \quad (8.18)$$

Both components have a lever arm to CoG and contribute to the resulting moment. The horizontal lever arm equals the difference in horizontal x -coordinate between CoG and the point of interest at the circumference x . The horizontal lever arm combined with the vertical component F_z determines the moment contribution. Equivalent for the moment of F_z with the difference in vertical coordinates.

$$\begin{aligned} M_x &= F_x \cdot (z - z_{CoG}) \\ M_z &= F_z \cdot (x - x_{CoG}) \end{aligned} \quad (8.19)$$

The coordinates of CoG depend on the rotation angle ϕ and are calculated based on the initial coordinates $x_{CoG,in}, z_{CoG,in}$ by using trigonometric relations.

$$\begin{aligned} x_{CoG} &= \cos(\phi) \cdot x_{CoG,in} - \sin(\phi) \cdot z_{CoG,in} \\ z_{CoG} &= \sin(\phi) \cdot x_{CoG,in} + \cos(\phi) \cdot z_{CoG,in} \end{aligned} \quad (8.20)$$

The integral is hard to solve directly and is therefore approximated by dividing the circumference in $n = 100$ panels. The total overturning moment is determined by the summation of the two contributions of all panels. The diameter of the drum along the x -axis is split in 100 equally spaced x_i -coordinates. A panel is determined by two successive x -coordinates (x_i, x_{i+1}) with corresponding z -coordinates via Equation 8.17. The pressure is determined at the middle point of the panel at ($x = \frac{x_i + x_{i+1}}{2}, z = \frac{z_i + z_{i+1}}{2}$). The force of each panel is determined by integration over the panel area as shown in Equation 8.21.

$$F = p\left(\frac{x_i + x_{i+1}}{2}, \frac{z_i + z_{i+1}}{2}\right) \cdot \sqrt{(x_{i+1} - x_i)^2 + (z_{i+1} - z_i)^2} \cdot B \quad (8.21)$$

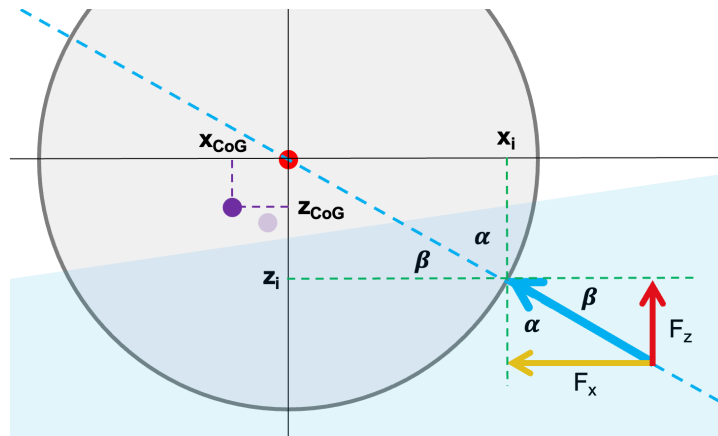


Figure 8.3: Force of one panel split into the horizontal F_x and vertical F_z component and visualization of the lever arm with respect to the shifted CoG represented as the purple dot (the shaded purple dot represents the initial CoG position)

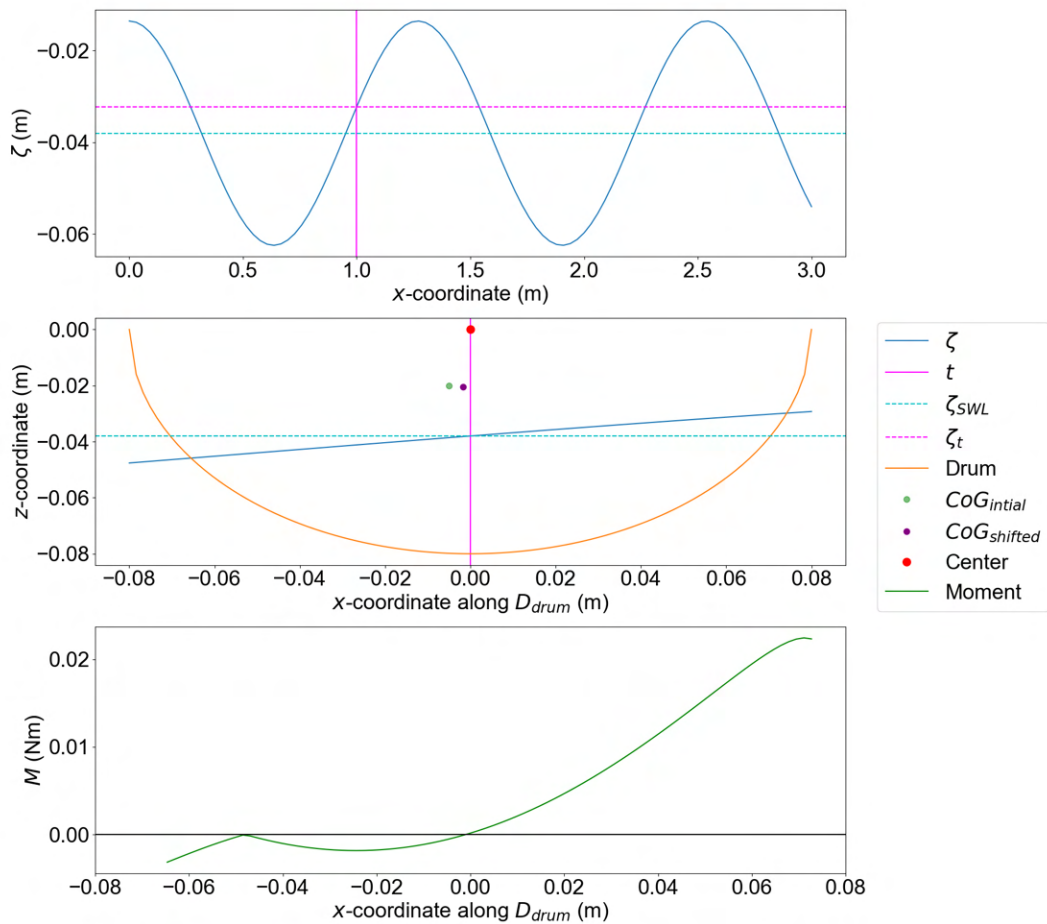


Figure 8.4: Determination of the moment contributions over the drum diameter based on the chosen point of the wave and the rotation from the measurements at that surface elevation.

The center of the drum has a constant vertical distance to the water surface during the excitation observed in the recordings. This is motivated by the surface elevation and vertical drum motion shown in Figure 7.1, which are in phase and equal in amplitude. Hence, the vertical distance between the center

and water level during excitation remains equal to the distance in the undisturbed situation. The drum is initially submerged for a vertical height of 0.042 m and the distance between drum center and water level is $0.08 \text{ m} - 0.042 \text{ m} = 0.038 \text{ m}$. The moment due to the dynamic wave pressure is proportional to the slope of the free surface ζ over the drum diameter at a certain time. The drum diameter is smaller than the wavelength and consequently, the free surface over the drum will look linear instead of curved. ζ is a harmonic motion described by Equation 8.14 and characterized by the wavelength and amplitude as shown in the top graph of Figure 8.4 for a fixed time $t = 0 \text{ s}$. With the use of the measurements influencing the rotation shown in Figure 7.2, the surface elevation can be linked to the rotation angle at a certain time t . For example, the surface elevation ζ indicated by the vertical magenta line in Figure 8.4 corresponds with a negative rotation of $\phi = -8^\circ$ obtained from the measurements. The rotation results in a shift in the position of CoG , according to Equation 8.20, which is visualized in the middle graph of Figure 5.6. The surface elevation at the chosen time is shifted to the mean water level ζ_{SWL} at the center of the drum since the drum mimics the vertical surface elevation. Thereafter, the dynamic pressure is calculated over the drum diameter with the use of Equation 8.15 based on the chosen point of the surface elevation. Integrating the moment contribution over the wetted drum circumference results in the total overturning moment. The moment contributions stated in Equation 8.19 over the diameter are plotted in the bottom graph of Figure 8.4. Note that only panels with a z -coordinate below the water surface have a contribution to the moment.

Mooring force

The static component is equal for all waves ($F_{pre} = 0.20 \text{ N}$). The drift contribution to the mooring force depends on the excitation characteristics. The total mooring force does not depend on the rotation, especially with elastic lines (small elongations hardly increase the line load). The connection location at the drum is important since the force remains tensile over time. Hence, the mooring force introduces a counteracting moment in one direction while increasing the rotation in the other direction.

Damping

Damping plays an important role around the natural frequency since the amplification is limited by the amount of damping. Excitation frequencies not located around the natural frequencies are less influenced by the damping. Damping is proportional to the angular velocity and is hard to determine for floating structures since there are different contributions such as wave making damping, eddy generation damping, lift damping and friction damping [7]. Hydrodynamic interaction of the components is unavoidable and therefore the damping coefficient over the frequencies is strongly nonlinear. For this case, the draft of the model is (negligible) small and therefore the eddy making damping is expected to be small. On the other hand, wave-making damping will have a considerable contribution due to the water displacement of the submerged sheet for both the roll and heave motion. Frictional damping is negligible since the velocities are low and therefore the influence will be even less for the real case because the Reynolds number is not scaled well as already mentioned. The same applies to the contribution of lift damping due to the low velocities.

8.2. Link with measurements

The measurements influencing the rotation according to the equation of motion stated in Equation 8.4, are discussed for each wave by evaluating force contributions at four time steps over one period. The time steps are chosen to visualize the maximum positive and negative rotations and two steps in between where $\phi = 0^\circ$. The pressure distribution around the circumference caused by the wave is the driving moment initiating the rotation, approximated with the described method in Section 8.1.3. The evaluation procedure is demonstrated for wave 2 and thereafter the analysis of the other waves is described in a more concise manner. Note that the motions of wave 1 are not reliably obtained due to the occlusion of the markers in the recordings. Therefore, the analysis of wave 1 is included last.

In the current configuration, the mooring line is connected to the center of the drum resulting in a small lever arm with respect to CoG . The mooring force does not change sign during the excitation and remains tensile. Therefore the mooring force counteracts a positive rotation and increases the rotating moment in the negative direction. The vertical distance between CoG and the center should be used since as discussed, only the (horizontal) x -component of the mooring force is relevant and evaluated for this experiment. The static mooring force is independent of the excitation and has a magnitude of

$F_{pre} = 0.20$ N. The dynamic contribution of all waves ranges between 0.15-0.3 N with a small lever arm (drum center to CoG), whereas the force in the connection ranges between 0.8-12 N with a much bigger arm (10 mm outside D_{drum} to CoG). Hence, the mooring force hardly influences the rotation in this experiment and is not included in this evaluation.

8.2.1. Wave 2

The measurements of wave 2 in the stable interval are plotted in Figure 8.5 with the four time steps indicated by the magenta line and the corresponding snapshots.

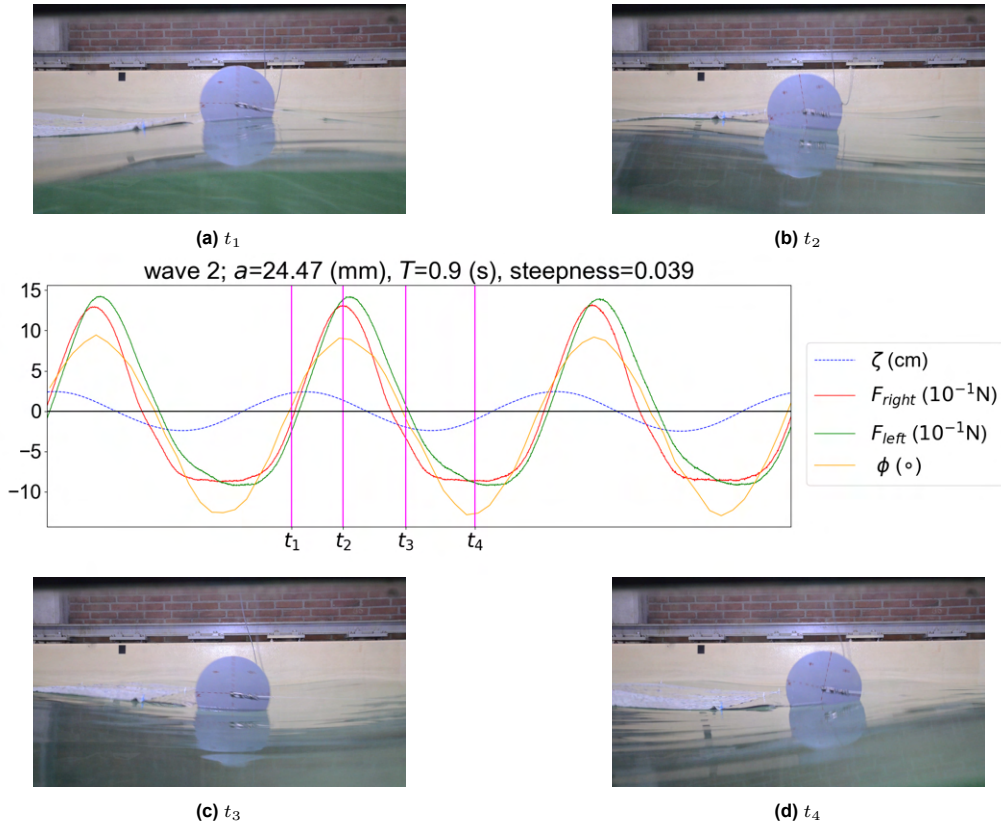


Figure 8.5: Measurements influencing the rotation during excitation of wave 2. Visualization of the four evaluated timesteps indicated by the magenta lines

It is visible from the measurements that first the maximum surface elevation ζ is observed and $\frac{T}{6}$ later the maximum positive rotation follows shown in Figure 8.5b. The same is observed for the minimum surface elevation in combination with the maximum negative rotation. The signal of the force transducers F_{right} , F_{left} are in phase with the rotation where maximum forces are measured at the maximum rotations. The maximum negative rotation $\phi = -12^\circ$ is bigger than the positive rotation $\phi = +9^\circ$. However, the measured force in the connection (sum of F_{right} and F_{left}) is bigger for the positive rotation $F_{connection} = 2.8$ N compared to the negative rotation $F_{connection} = -1.6$ N. A small phase shift between F_{right} and F_{left} is visible which indicates a slight rotation of the model.

Time step t_1

The rotation and connection force is zero and ζ is right before its maximum crest level. The moment is 0.5 Nm which initiates the positive rotation shown at t_2 .

Time step t_2

Both the connection force $F_{connection} = 2.8$ N and rotation $\phi = +8^\circ$ have their maximum magnitude, the resulting moment is -0.34 Nm. The measured connection force can either be caused by elongation or by submerging additional length of the sheet, as explained in the previous section. The drum is $\phi = +8^\circ$ rotated which corresponds to a traveled distance at the connection location with $r_{connection} = \frac{D_{drum}}{2} + 0.01$ m according to Equation 8.22 of 0.013 m.

$$distance = \frac{\phi}{360^\circ} \cdot 2\pi r_{connection} \quad (8.22)$$

This makes it unlikely that the sheet followed the rotation by elongation since the measured force of 2.8 N is smaller than the required force to elongate the sheet $F_{elongation} = 5.8 \times 10^3 \text{ N} \cdot 0.013 \text{ m} \approx 7.54 \text{ N}$. More reasonable is that 0.013 m length of the sheet is extra submerged. Hence, $F_{buoyancy} = 0.54 \text{ N}$ should be counteracted by the drum, however, only a part of this force is measured by the force transducer as shown in Equation 8.5. The initial angle of 85° is reduced by ϕ resulting in $F_{buoyancy,measured} = 0.03 \text{ N}$ with $\alpha = 93^\circ$ (almost horizontal). The force due to the sheet required sheet motions $F_{a,sheet}$, is approximated with the use of the acceleration at the connection determined with Equation 8.11 and added mass m_a :

$$\ddot{\theta} = \zeta_{phi} \omega^2 \sin(\omega t) = \frac{2\pi}{360^\circ} \frac{10^\circ}{0.9} \left(\frac{2\pi}{0.9}\right)^2 \sin\left(\omega \frac{T}{2}\right) \approx 6.78 \text{ rad/s}^2 \quad (8.23)$$

$$a_{connection} = r_{connection} \cdot \ddot{\theta} = \left(\frac{0.16 \text{ m}}{2} + 0.01 \text{ m}\right) \cdot 6.78 \text{ rad/s}^2 \approx 0.61 \text{ m/s}^2 \quad (8.24)$$

$$m_{sheet} = BLh\rho_{sheet} = 1.00 \text{ m} \cdot 5.00 \text{ m} \cdot 0.005 \text{ m} \cdot 140 \text{ kg/m}^3 = 3.5 \text{ kg} \quad (8.25)$$

$$F_{a,sheet} = (m_{sheet} + m_a) \cdot a_{connection} = (3.5 \text{ kg} + 0.0 \text{ kg}) \cdot 0.61 \text{ m/s}^2 \approx 2.14 \text{ N} \quad (8.26)$$

Both contributions of $F_{a,sheet}$ and $F_{buoyancy,measured}$ are measured by the force transducers and present in the measured connection force. The force of the combined effects is 2.17 N and the measured force is 2.8 N. However, still a difference is shown but the magnitude is correct and this motivates that the most governing effects are included in the evaluation. The difference can be ascribed to other effects, for example, the acceleration at the connection which is assumed to equal the acceleration of the free-floating sheet. This is based on the sheet moving towards the drum. However, the snapshots show that the drum displaces in horizontal direction toward the sheet as well due to oscillatory motion (influencing the acceleration of the sheet). In reality, first the deflection of the submerged sheet changes due to the axial loading before submerging additional length. This leads to an increase in additional mass since the surrounding water must be accelerated.

Time step t_3

ϕ and $F_{connection}$ are both zero and the overturning moment is -0.45 Nm .

Time step t_4

This time step is opposite to t_2 with a bigger maximum negative rotation $\phi = -12^\circ$ and a smaller force in the connection -1.6 N with an overturning moment of -0.24 N . The connection force is analyzed with the same procedure as for t_2 , resulting in a smaller connection force. The rotation is in the direction of the buoyancy force (upward) and this causes the contribution of $F_{buoyancy}$ to be smaller. At t_2 , the rotation was in the contradicting direction which resulted in bigger forces. The acceleration of the free-floating sheet is lower as well since the uplifting of the sheet is visible in the snapshot. Hence, the entire free-floating sheet should be less displaced in the horizontal direction since the length is 'stored' vertically right above the connection. The generation of the air gap is caused by the bending stiffness D of the sheet, the sheet can not follow the curvature which is required to remain connected to the free surface. The curvature generates local bending stresses in the sheet which were not measured by the lower positioned force transducer. This explains the 'plateau' which is visible in the measurements of $F_{connection}$. The local curvature of the sheet changes first and closes the air gap while the rotation direction changes (no change in force measurable in the force transducer).

8.2.2. Wave 3

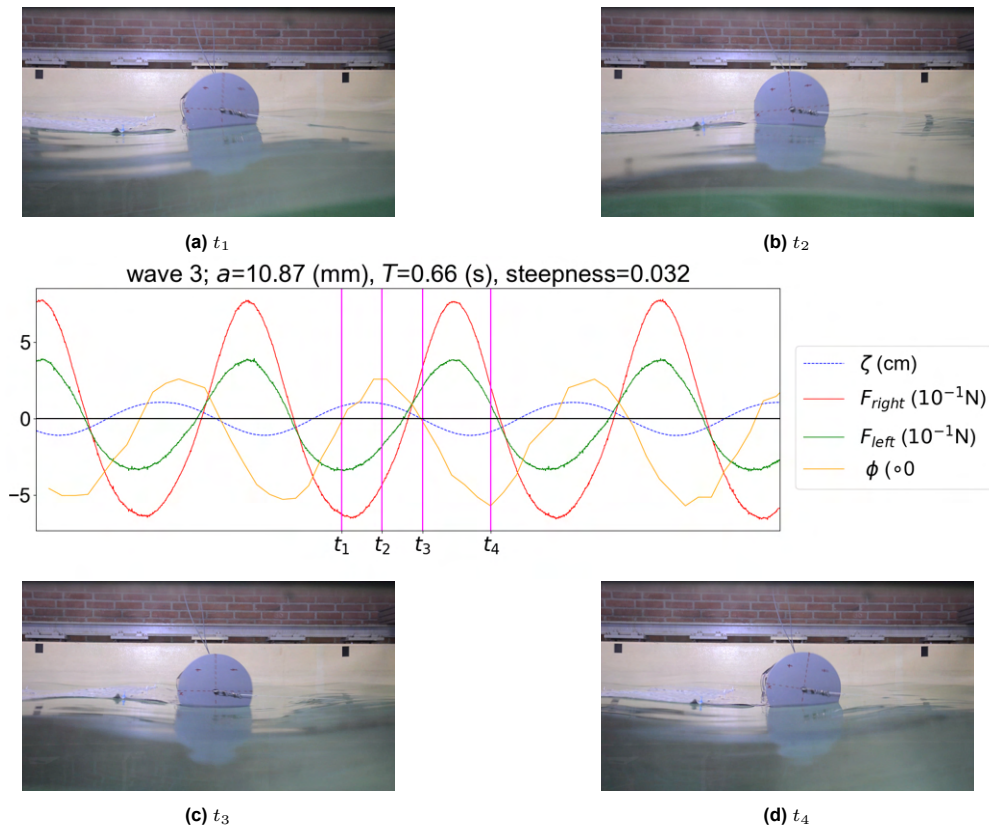


Figure 8.6: Measurements influencing the rotation during excitation of wave 3. Visualization of the four evaluated time steps indicated by the magenta lines

The rotation is almost in phase with the surface elevation, however, the connection force has $\frac{T}{2}$ phase difference as shown in Figure 8.6. The rotations are $\phi = -5^\circ$ in the negative direction and even smaller in the positive direction. As research showed, the free-floating sheet does not move horizontally during the rotation, therefore there is no contribution of $F_{a,sheet}$. The sheet follows the small motions by changing the deflection below the water surface where the initial submerged length determines the upward buoyant force. The rotation in the negative direction is in the direction of this buoyancy force and therefore the rotation is bigger than in the positive direction where the buoyancy force should be counteracted. When combined with the changing angle of the force transducer, relatively more of the vertical force is measured in the negative direction and less is measured in the positive direction while in reality, the force in the positive direction is bigger. The phase difference of the force transducers compared to the rotation is motivated by the negligible contribution of the horizontal sheet movement and only caused by the changing angle of the force transducer. Note that F_{right} measures almost double the force compared to F_{left} where a small rotation in the horizontal plane of the model can be the cause of this difference.

8.2.3. Wave 4

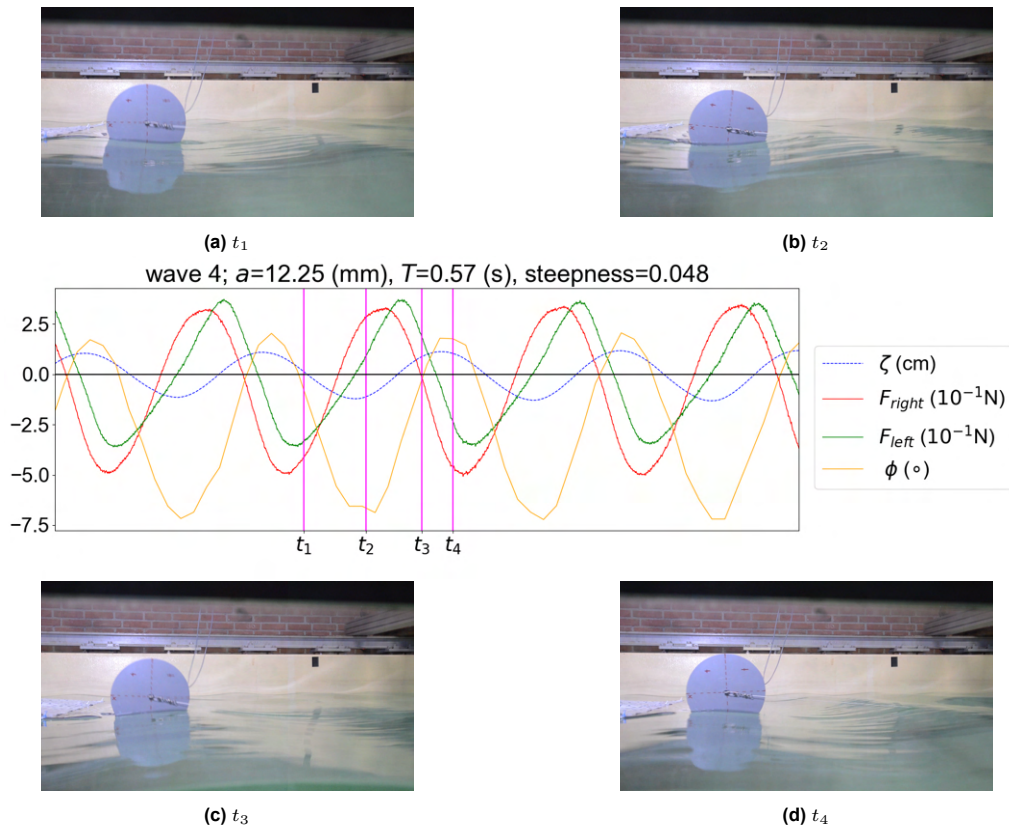


Figure 8.7: Measurements influencing the rotation during excitation of wave 4. Visualization of the four evaluated timesteps indicated by the magenta lines

The rotations for wave 4, the negative direction was bigger than the positive direction as shown in Figure 8.7. This is caused by the direction of the buoyant force of the submerged length as explained in the evaluation for wave 3. The moment for the four time steps are 0.18 N, -0.24 N, -0.45 N, 0.32 N and this matches the rotation direction over the time steps.

8.2.4. Wave 5

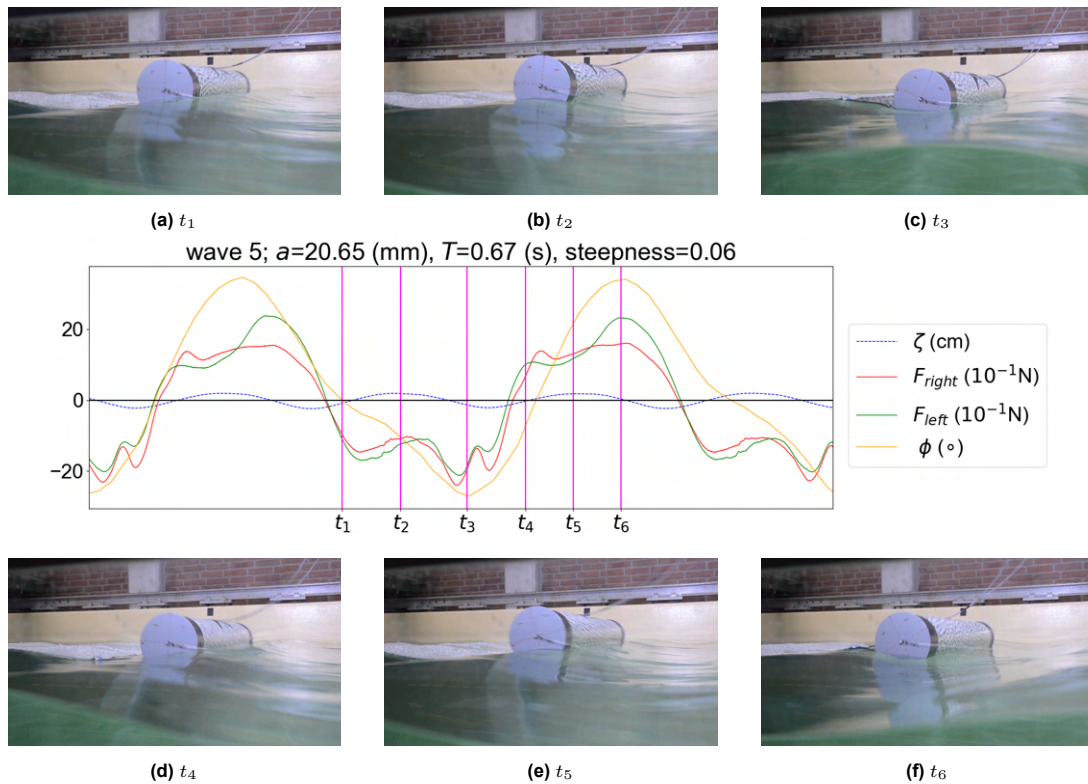


Figure 8.8: Measurements influencing the rotation during excitation of wave 5. Visualization of the six evaluated timesteps indicated by the magenta lines

The rotation is in phase with the connection force however the period was doubled when compared to the surface elevation. The natural frequency and the wave period are equal to wave 3 but for wave 5, the model can not follow the excitation motion. Hence, nonlinear effects of the wave due to the increased steepness influence the coupled motions. As shown in the snapshots in Figure 8.8, the rotation is not influenced by the wave crest present in t_2 which exerts a positive moment on the drum. The moment contribution of the connection force slightly lifts at t_2 and t_5 , while the rotation increases. It could be the wave steepness combined with the wavelength which exerts a counteracting moment at the submerged part of the thin sheet which is compared to the moment exerted at the front of the drum. This contribution is enough to prevent a change in direction of the rotation, while during the excitation of the next wave the overturning moment at the front of the drum is dominant initiating a change in the rotation direction.

8.2.5. Manually adjusted - wave 1

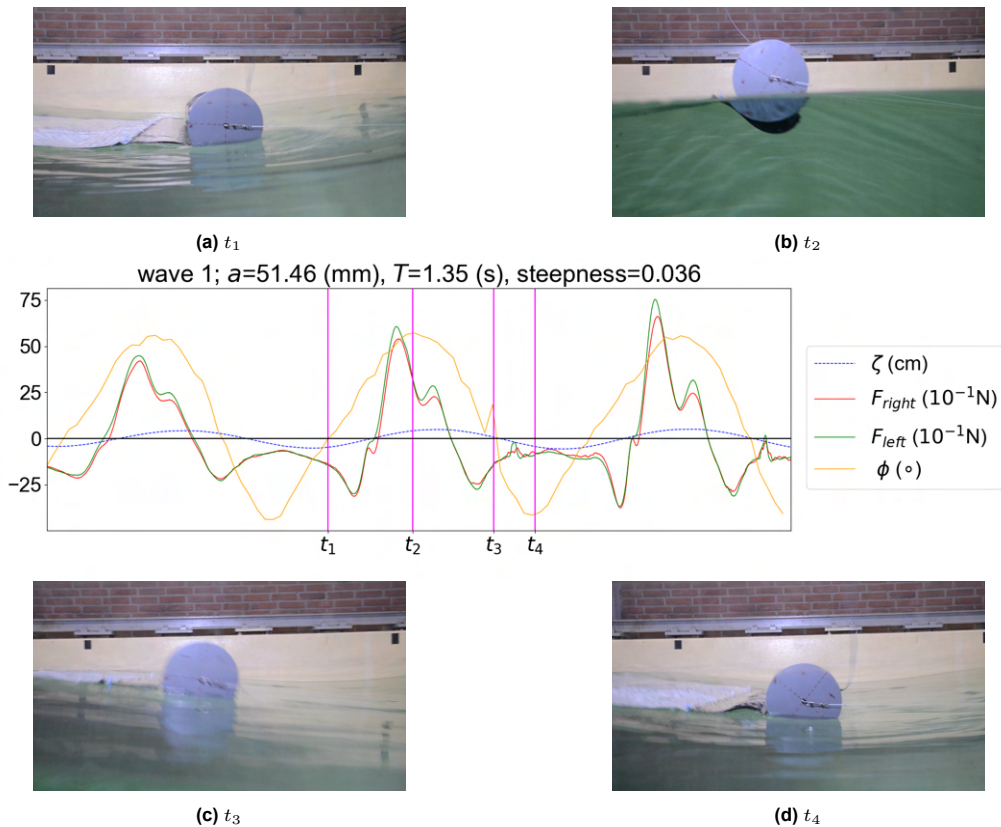


Figure 8.9: Measurements influencing the rotation during excitation of wave 1. Visualization of the four evaluated timesteps indicated by the magenta lines

The measurements during the longest wave used in the experiment are visualized in Figure 8.9. The rotations are big ranging from $+60^\circ$ to -35° . The horizontal sheet displaces significantly in the horizontal direction during the rotation and the acceleration is large $a_{connection} \approx 2.00 \text{ m/s}^2$ according to Equation 8.11 which results in $F_{a,sheet} \approx 8.60 \text{ N}$. However, the added mass of the surrounding fluid around the submerged sheet will be significant which is difficult to approximate based on empirical formulas. The contribution of $F_{buoyancy,measured}$ is hard to quantify since the sheet touches the drum as visible at t_2 , the upward force will be withstood by the drum. Uplifting of the sheet is visible at t_4 resulting in a reduction of measured connection force, similar to phenomena described for wave 2. The change in curvature of the sheet is governing until the rotation direction shifts and the air gap vanishes. The uplifting of the sheet at the maximum negative rotation results in the pumping of the water initially locked between the sheet and drum over the sheet. This water is spread over the sheet by the traveling waves.

8.3. Tuning the coupled hydrodynamic response

The reasoning behind the measurements is discussed for all five waves. However, especially the observations combined with the understanding of the influence of certain effects on the motions allow to tweak the response by adjusting the design parameters. The goal can be either to minimize or to maximize the rotations and thereafter could be looked into the different parameters and how they could be changed to reach the desired outcome. The wave force can not be influenced since this is the excitation force but what could be adjusted is the coupled response of the structure to the wave.

8.3.1. Connection

The moment due to the connection force can be influenced by either adjusting the lever arm related to the connection location or adjusting the connection force depending on the properties of the sheet. The

greater the counteracting moment of the connection force, the more the rotation is restricted. Changing the location of the connection results in a different arm, one option could be extending the clearance between the drum connection and increasing the arm which scales linearly with the moment. The connection force and the change in length of the submerged sheet stated in Equation 8.7 can be tweaked. Broadening the difference between ρ_w and ρ_{sheet} by constructing the sheet of more lightweight materials will increase the resistance to submerging the sheet. Increasing the thickness of the sheet increases the volume per meter submerged length, which decreases Δl .

When the rotations have to be limited, the sheet resistance must be increased as proposed above. If that is the case, the magnitude of the connection force will increase since it opposes the rotation. If big rotations are allowed, the resistance of the sheet can be lowered. The magnitude of the connection force could be reduced if the sheet does not resist the rotation and is dominated by the excitation moment of the wave.

8.3.2. Moment of inertia

Both the mass and division of mass over the structure (moment of inertia) can be adjusted to tune the type of hydrodynamic response, to either mimic the excitation frequency versus not being able to follow the motion. Increasing the structural mass lowers the heave natural frequency as stated in Equation A.16, and positioning the mass further from the drum center lowers the roll natural frequency as shown in Equation A.17. Nevertheless, in reality, both parameters are correlated and it is challenging to adjust both independently. An increase in I_{yy} provides more resistance to the angular accelerations.

8.3.3. Mooring

Adjusting the connection location of the mooring force changes the arm and the resulting moment. In case the rotation in one direction is bigger than in the other direction, the connection point could be either placed below or above CoG to reduce the rotation angle in one direction. This becomes relevant when the mooring forces are significant, resulting in a higher contribution to the resulting overturning moment. For example, if the natural heave frequency is lowered below the excitation frequency, the structure is not able to follow the excitation motion anymore and therefore the drift force will increase.

8.3.4. Metacentric height

To strengthen the general stability and the roll natural frequency, the distance between the rotation point (drum center) and the vertical CoG position could be increased according to Equation A.17. Improved stability will lower the rotation angle since the counteracting moment due to the horizontal shift in CoG position increases.

8.4. Feasibility of the designed concept

The feasibility of the designed concept is discussed for both the coupled hydrodynamic perspective as well as for the obtained mooring forces within this study.

8.4.1. Adjusting the coupled hydrodynamic response

The large rotations of the drum have a negative influence on the coupled hydrodynamic behaviour for HMC. The sheet is accelerated and water is spread over the structure at wave frequencies which are regularly expected during the operations of Sleipnir. The rotations can be reduced by lowering the natural roll frequency of the system. Within the designed concept, the drum is not able to follow the excitation motion anymore and remains stable. The drum turns out to be dominant in the coupled hydrodynamic behaviour due to its properties compared to the hydrostatic resistance of the sheet around the connection. Either the roll moment of inertia of the drum can be altered, while the dimensions remain unchanged, or the dimensions of the drum can be adjusted.

The structural moment of inertia in roll direction I_{yy} or the additional moment of inertia δI_{yy} can be adjusted by modifying the connection at the drum circumference. The structural roll moment of inertia can be increased by adjusting the shape of the drum to for example a more rectangular shape. The water displacement required for a rotation increases significantly represented in the additional moment of inertia δI_{yy} . To be more precise, a noncircular shape makes spooling the drum less convenient and influences the handling negatively. Variations to the chosen cylindrical shape might be more realistic,

for example opening up the drum during deployment to have two connected (horizontal) half-moon shapes instead of one circle. The connection is currently located below the water surface, shifting the connection to the waterline increases the additional moment of inertia. The entire sheet is initially freely floating which means that more water is required to be replaced to be able to submerge the sheet during a rotation. In line with this reasoning, HMC can increase the sheet thickness close to the connection to increase the contribution of the buoyancy force to the counteracting moment. However, increasing the sheet thickness will increase the bending stiffness which will result in a bigger characteristic length and an increase in wave structure interaction where the latter is not desired. The water pumping of the concept can be reduced by shifting the connection to the waterline. This prevents the water, which is initially locked between the drum and the sheet, is spread over the sheet due to the rotations. The rotations should be minimized which does not lead to submergence of the sheet during excitation and water can not flow onto the sheet.

Another option to reduce the rotations is to lower the drum diameter. Lowering the drum diameter will increase the influence of the sheet on the drum motions, which is similar to the desired effect of increasing the sheet thickness while keeping the drum properties unchanged mentioned earlier. From a structural point of view, due to the spooled thin sheet, the drum should be able to withstand the stresses. Since the diameter is not limited by the flexible PV, the curvature can have a radius up to 0.15 m. To be able to withstand the stress due to the bending moment, the limiting length for the drum design seems to be 30 m. Based on the chosen sheet and wall thickness $t_{drum} = 20$ mm, the drum diameter must have a minimum diameter of 1.4 m to prevent exceeding the steel yield stress of 235 N/mm² according to the reasoning stated in Appendix A. The material stress can be reduced by increasing the moment of inertia of the drum by stiffening the hollow cross section with struts or by using steel with higher strength.

Both options do not increase the mass of the system significantly. However, the hydrostatic stiffness is increased resulting in an even higher natural heave frequency. This is beneficial since the heave natural frequency should be higher than the excitation frequency to be able to mimic the wave motions and reduce the reflected energy. This is automatically obtained by a low draft of the drum.

8.4.2. Interpretation of the mooring force

It turns out the mooring force is small for the designed concept since the system mimics the wave motion. However, the mooring force remains an important parameter for the feasibility of the temporary deployment of the concept for HMC. The measured forces are scaled to full scale by $(\frac{1}{\alpha})^3$ which results in a maximum drift force of 5940 N as stated in Table 8.1. Combined with the static force contribution on real scale, the maximum expected mooring force is 11 757 N. A simple mooring system is able to withstand these small forces and therefore temporary deployment will not be an issue for HMC for this designed concept.

With the use of measured drift force on model scale, the reflected wave amplitude ζ_r can be calculated with the use of the Maruo Equation 2.1. It turns out that the model reflects a small amount of the incoming wave energy, which is in line with the expectations and observations that the structure follows the excitation motion. Research also showed that the reflected amount of energy increases with decreasing wavelengths, which is reasonable since the wave frequency tends towards the natural frequency of the model. Hence, the reflected energy becomes smaller towards the larger wavelengths where more energy is present in the workability spectrum of Sleipnir according to Figure 2.11.

	Model scale			Full scale			Reflected energy	
	F_{pre} (N)	F_{drift} (N)	$F_{mooring}$ (N)	F_{pre} (N)	F_{drift} (N)	$F_{mooring}$ (N)	ζ_r (mm)	$\frac{\zeta_r}{\zeta}$ (%)
wave 1	0.20	0.22	0.42	5563	6194	11757	3.01	5
wave 2	0.20	0.10	0.30	5563	2789	8352	2.02	9
wave 3	0.20	0.06	0.26	5563	1759	7323	1.60	13
wave 4	0.20	0.12	0.32	5563	3239	8803	2.17	23
wave 5	0.20	0.20	0.40	5563	5493	11056	2.83	14

Table 8.1: Contributions of the static F_{pre} and drift contribution F_{drift} to the total mooring force $F_{mooring}$ on model scale and scaled to full scale. ζ_r indicates the reflected wave height according to the Maruo formula

Note that this research only focuses on the wave loading where the perpendicular area to the wind direction is increased significantly in the deflected position of the system during excitation as motivated in this study. An estimation of the contribution to the mooring force is determined with Equation 8.27 [18].

$$F_{drag,wind} = \frac{1}{2} \rho_{air} u_{wind}^2 A C_d C_s \quad (8.27)$$

where A represents the perpendicular area to the wind direction, $\rho_{air} = 1.225 \text{ kg/m}^3$, $u_{wind} = 10 \text{ m/s}$ is the maximum wind velocity during operations of Sleipnir, $C_d = 0.7$ is the drag coefficient according to DNV [12], C_s represents the sheltering coefficient dependent on the number of waves in front. The structural deflection due to the first wave is the most influenced by $C_s = 1.0$ and $C_s = 0.5, 0.3, 0.2$ for the second, third, and onward sinusoidal deflections according to [36].

The biggest wave used in the experiment with $\lambda = 85 \text{ m}$ and $H = 3.4 \text{ m}$ has two deflections over the full scale structural length $L = 150 \text{ m}$ with $A = H \cdot B$ and results in:

$$F_{drag,wind} = \sum_{i=1}^2 \frac{1}{2} \cdot 1.225 \text{ kg/m}^3 \cdot 10^2 \cdot (3.4 \text{ m} \cdot 30 \text{ m}) \cdot 0.7 \cdot C_{s,i} \approx 6560 \text{ N}$$

The steepest wave with $\lambda = 20 \text{ m}$ and $H = 1.3 \text{ m}$ results in 8 deflections over the full scale structural length and results in:

$$F_{drag,wind} = \sum_{i=1}^8 \frac{1}{2} \cdot 1.225 \text{ kg/m}^3 \cdot 10^2 \cdot (1.3 \text{ m} \cdot 30 \text{ m}) \cdot 0.7 \cdot C_{s,i} \approx 6689 \text{ N}$$

This simple approximation illustrates that wind has a similar contribution to the mooring force as the wave loading has on full scale. Hence, wind loading is relevant to evaluate to obtain the total mooring force. This can be done with model tests or simulations as shown by Trapani [46].

9

Conclusion

Offshore projects of Sleipnir have a duration in the range of days and the savings in energy should outweigh the installation effort. This study demonstrates that OFPV can be a promising option for HMC as energy supply for Sleipnir during operations.

Considered from the perspective of the concept, HMC must be able to deploy the concept temporarily at the project location which requires easy handling and deployment. The availability of thin-film PV characterized by the low mass and low bending stiffness allows for a flexible supporting structure. A very flexible structure follows the wave motions with negligible wave structure interaction if the ratio between the characteristic length λ_c and the excitation wavelength λ satisfies $\frac{\lambda_c}{\lambda} \ll 1$. Interference of the structure and the waves should be limited since this leads to energy transfer resulting in forces. A flexible sheet with structural height of 236 mm composed of several layers (top to bottom: 0.5 mm HyET PV, 0.5 mm steel, 230 mm foam and 5 mm neoprene) is chosen as supporting structure, with horizontal dimensions of 150 m length and 30 m width. The sheet results in a negligible disturbance of the excitation waves motivated by the characteristic length of 5.51 m and the smallest wavelength expected in the reality of 15 m. The sheet cross section is composed of different material layers to modify the stress distribution over the structural height and to reduce the strain in the PV.

The sheet is spooled on a steel drum with a diameter of 4.8 m during transport with the mooring lines attached to the drum during deployment. The draft of the drum is low (21 % of the vertical height) resulting in a high natural heave frequency. Ideally, the heave natural frequency should be higher than the excitation frequencies present in the workable wave spectrum of Sleipnir to minimize the reflected energy (and drift force). To conclude, this study shows that the drum is able to follow the vertical surface elevation since the stiffness term dominates over the mass term during wave loading.

Secondly, considering the scaling, the goal is to determine the hydrodynamic response of the concept consisting of a sheet connected to the drum, to surface waves with model tests. Surface waves are gravity-driven and Froude scaling ensures that the gravity forces are well scaled. Hence, the properties are scaled with a geometric scaling factor $\alpha = \frac{1}{30}$ based on Froude. The terms in the hydroelastic dispersion relation should be scaled well related to the sheet in order to have a similar hydrodynamic response at model scale and at full scale. Therefore, the characteristic length in relation to the structural length and the draft in relation to the structural height should be scaled well. For the drum, the diameter, mass and moment of inertia are the most important parameters to scale. The diameter of the drum relates to the waterplane area and determines the draft combined with the mass. The distribution of mass along the three orthogonal axes determines the moment of inertia. The resistance to roll (moment of inertia along the centroidal axis) influences the rotations and is the most important part of this 2D setup.

When looking at the design parameters, the hydrodynamic behaviour of the concept is influenced by the mass and position of *CoG*. The drum rotates around its center where the stability increases if the vertical distance from the center to *CoG* is increased. The natural frequencies of the coupled system are ideally chosen outside the operating spectrum of Sleipnir and therefore higher natural frequencies are preferred. Several configurations with varying mass and *CoG* positions are experimentally tested

to determine the influence. Increasing the mass results in a slow system and lowers both natural frequencies (heave and roll). The connection location along the drum circumference in the undisturbed situation is directly related to the horizontal CoG position. Experiments showed that the connection location influences the submerged length (buoyant force) and the curvature of the submerged sheet. The curvature of the sheet indicates the bending moment which is present at that location which introduces damping and a counteracting moment to the roll motion. If the sheet has a horizontal departure angle, no counteracting moment and negligible damping are present at the connection. In case CoG lays close to the center, the connection is initially located at the waterline resulting in an air gap between the sheet and the water determined by the bending stiffness. The optimum lays in between the point where the sheet has a slight curvature at the connection ($\omega_{0,roll} \approx 7 \text{ rad/s}$, $\omega_{0,heave} \approx 11 \text{ rad/s}$), obtained by shifting the horizontal CoG 5 mm from the center (towards the sheet). To improve the stability, the vertical CoG position should be lowered. However, there is a trade-off since this requires additional mass at the bottom of the drum which results in an increase in the total mass of the system.

In light of the interaction of the coupled system, the drum follows the vertical surface elevation for all waves and the overturning moment is proportional to the slope of the free water surface over the drum diameter. And also the dynamic wave pressure is the driving force for the rotation and can be approximated by integrating the pressure over the wetted drum circumference while accounting for the orthogonal lever arm with respect to CoG . Experiments showed that the current chosen concept configuration results in water pumping over the sheet for the longer wavelengths. These waves are regularly present in the workability wave spectrum of Sleipnir. The spread of water over the sheet is problematic since the draft will increase and the PV production will be negatively affected. Consequently, the natural frequency of the sheet decreases, resulting in more wave structure interaction according to the hydroelastic dispersion relation. The water pumping is caused by the large (right turning) rotations. Large right-turning rotation leads to uplifting of the sheet which causes water pumping and this results in water that was initially located between the submerged sheet and the drum spreading over the sheet.

The force in the connection is a reaction force to the rotation since the rotation requires the sheet to follow. The sheet can either follow the motions by elongating or by submerging an additional length of the free-floating sheet. Experiments led to the conclusion that the measured connection force can not be ascribed to elongation since this would require a higher force (proportional to the axial stiffness). The rotation angle is followed by submerging extra length, which leads to an increase of the buoyant force and includes a force related to the required acceleration of the free-floating sheet. The magnitude of both contributes to the counteracting moment which depends on the rotation angle. For small rotations, the buoyancy force is governing and the horizontal sheet remains almost undisturbed. For large, rotations the contribution of the acceleration of the free-floating sheet is governing for the connection force.

Lastly, the mooring forces are determined with the use of the newly developed 3D-sensor with an accuracy of 0.36 % of the total capacity 34 N equal to 0.12 N. However, the direction of the static force in the undisturbed situation is not in line with the mooring line geometry. The estimated pretension based on the line elongation is 0.10 N. This is at the lower limit of the 3D-sensor within the noise and therefore the static force measurements can not be used. The measured drift contribution is reliable since this is depending on the sensitivity of the 3D-sensor. The sensitivity relates to the increase in measured voltage in (V) to force in (N) and is reliably obtained from the calibration due to the strong linear behaviour of the individual sensors present in the 3D-sensor. A force of 0.20 N is measured for the steep wave (steepness=0.065) with $\lambda = 0.68 \text{ m}$ and is compared to 0.06 N for the less steep variant. The drift force has maximum magnitude of 0.22 N for the low frequency wave ($\lambda = 2.84 \text{ m}$, steepness=0.039) which translates to 6194 N in the full scale case. Combined with the pretension, this results in a total mooring force of 11 757 N where a simple mooring design will suffice. Temporary deployment of the mooring will not be an issue for HMC considering the wave loading. However, the structural area perpendicular to the wind direction increases in the deflected position due to the wave motions. A simple approximation indicates a similar contribution, as the wave drift force to the total mooring force. This illustrates that wind loading becomes more relevant and should be evaluated to determine the total mooring force.

The feasibility of an OFPV concept for Sleipnir is demonstrated where research showed that the natural roll frequency has to be lowered by reducing the roll motions. Furthermore, as stated from

the obtained data, the drum dominates the coupled hydrodynamic behaviour compared to the small influence of the thin sheet. The roll motion of the OFPV concept can be lowered by reducing the diameter of the drum or by increasing the thickness of the sheet near the connection location. The latter is less favorable since this increases the characteristic length which will therefore increase the wave structure interaction. Therefore, the drum diameter should be as small as possible from a hydrodynamic perspective. However, from a structural point of view, the material stress decreases with increasing diameter. The influence of the hydrostatic stiffness of the sheet should become higher in relation to the drum, represented as the additional moment of inertia in the roll equation of motion. The total roll moment of inertia can be easily increased by changing the geometry of the drum to a more rectangular shape. However, this is a less suitable option due to the negative influence on the handling since spooling of the sheet will become harder. To conclude, the draft of the drum must remain low in order to have natural heave frequency that is bigger than the excitation frequency, otherwise, the reflected energy increase will result in a higher drift force.

10

Recommendations

The value for HMC depends on how well the system can be implemented within its day-to-day operations. The deployment and retrievability of a floating solar concept have a major influence on the business case for HMC. Hence, a thorough recommendation is presented relating to the possibilities of how such a system can be temporarily deployed and moored next to Sleipnir. For future recommendations, HMC can develop a model which predicts the electricity generation which is depending on the time of the year and the working location of Sleipnir. This will help to further determine the potential and business case of an OFPV concept.

10.1. Future research

This study illustrates the feasibility of an OFPV concept for Sleipnir from a hydrodynamic perspective. However, the rotations of the drum should be minimized to reduce fatigue loading of the sheet and water pumping over the sheet. Further research could dive into various options for the geometry of the front structure. These should be evaluated by HMC from a hydrodynamic perspective and the ease of use (handling, transport and deployment). Furthermore, a numeric model incorporating the hydrodynamic behaviour can help to determine the influence of adjusting the dimensions of the drum or changing the shape of the hydrodynamic response.

Something else HMC can look into the useable materials for the composition of the thin sheet. The lifetime of the structure is proportional to the durability of the used materials. The overall business case is strongly related to the lifetime of the structure since this relates to the total amount of generated electricity which should outweigh the investment.

The flexible structure is characterized by its lightweight design and therefore prone to uplifting. The perpendicular structural area to the wind direction is increased significantly in the deflected position due to the wave loading. Therefore, it is highly recommended to perform experiments in a wind tunnel to gain an understanding of the influence. This study focused on head waves to identify the response at certain frequencies. However, in reality, the excitation waves are multi-directional and a combination of the environmental forces (wind, waves and current). Tests with directional loading must be performed to identify the influence on the hydrodynamic behaviour to propose improvements for the design.

10.2. Model test improvements

From a more practical point of view, improvements can be made to the choice and use of the equipment. The mooring force was measured with the newly developed 3D-sensor and the calibration was performed under a predefined angle. A change in orientation results in a change in the relative sensitivities of the three sensors. Initially, the 3D-sensor was mounted to a camera ball head which could not be locked tightly, and therefore during the calibration the lock was released. Henceforth, the 3D-sensor

could be mounted to a rigid structure that remains stable to have a negligible change in orientation. Furthermore, the 3D-sensor was moved from the calibration location to the measurement location in the towing tank. The experiments showed that it was difficult to exactly mimic the angle in the tank as used in the calibration. Since small deviations in orientation have a significant influence on the measurements as proved within this study. In this experiment, due to the mentioned points above, the 3D-frame was rotated slightly in the tank. This could have been prevented by using a frame to ensure the orientation for both the calibration and measurement location is similar. The measured forces during this experiment were in the lower range of the load capacity of the 3D-sensor and the static mooring force was similar in magnitude to the measurement noise. Therefore, the pretension of the mooring force could not be obtained with this sensor. For the next time, this experiment will be done, this could be slightly improved by adding more steps at the lower range of the sensor in the calibration. Or by choosing a different sensor, where the expected forces are around the middle of the load capacity of the sensor.

Unfortunately, the camera used at the side of the towing tank was not able to sharply capture the high accelerations of wave 1. The result was that the markers at the drum lid were barely visible and therefore object tracking did not work. This was solved by manually drawing the markers, however since this reduces the accuracy of the measurements next time a better camera could be used. Capturing motions with a high-speed camera would have prevented this problem. Furthermore, an increase in the frames per second will also contribute to the quality and accuracy of the measurements. Besides the camera, also the starting time of the light trigger with the camera recordings can be determined with higher accuracy. This improved accuracy will be incorporated into the measurements as well since the measurement synchronization is performed based on the light trigger.

The motions of the sheet are recommended to measure during excitation to be able to fully answer the research question if the concept is feasible. The displacements of the entire sheet should be obtained with small distances between successive points to determine the motions of the flexible structure. Multiple measurement locations must be obtained over one wavelength to be able to reliably determine the motions in space to prevent aliasing. For example, Digital Image Correlation seems to be a promising method to determine the motions with two synchronized cameras. However, understanding the calibration procedure and parameters influencing the outcomes must be researched. Thereafter, these techniques can be successfully used in model tests to determine the motions of flexible structures.

10.3. The future success of OFPV

Sustainable energy technologies should be evaluated based on the total lifetime including construction, installation, maintenance, and decommissioning. A business case for OFPV is reliable to estimate since the location-dependent electricity generation of a floating solar field is accurate to predict. There is a trend toward more lightweight supporting structures due to the availability of thin-film PV which positively affects the business case. These concepts require less material, are easier to transport due to the flexibility and a simpler mooring system suffices due to the smaller mooring loads. Reducing the fixed (production, installation, and decommissioning) and the variable costs (maintenance) of a concept directly increases the profitability because the energy yield remains unchanged.

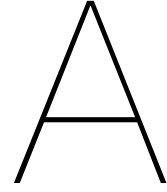
Upscaling the production and increasing the efficiency of flexible panels are related to costs. The development of both determines the future success of flexible OFPV. Further research is required to develop new OFPV concepts and the amount of financial incentives of the government is proportional to the acceleration of knowledge. Methods to determine the hydrodynamic (nonlinear) response to wave loading are required to determine the feasibility in offshore conditions. Therefore, new modeling techniques should be developed to efficiently evaluate new concepts. Besides the mathematical difficulty of flexible structures, the horizontal dimensions are much bigger than conventional ships which require more computer capacity to solve. These are all technical related challenges but the impact on marine life must be assessed as well. This heavily influences the adaptation of OFPV within society.

Bibliography

- [1] Meteonorm - <https://meteonorm.meteotest.ch/en/>.
- [2] E. Alexopoulos. Introduction to Multivariate Regression Analysis. 2010.
- [3] T. A. Beinema. Floating Solar A hydroelastic method. Technical report, 2020.
- [4] V. Bertram. Ship Seakeeping. In *Practical Ship Hydrodynamics*, pages 143–204. Elsevier, 1 2012.
- [5] Y. A. Cengel. *Fluid Mechanics*. Tata McGraw-Hill Education, 2010.
- [6] R. Cengiz Ertekin and J. Whan Kim. Hydroelastic Response of a Floating Mat-Type Structure in Oblique, Shallow-Water Waves. *Journal of Ship Research*, 43(4):241–254, 1999.
- [7] S. Chakrabarti. Empirical calculation of roll damping for ships and barges. Technical report, 2001.
- [8] X. J. Chen, Y. S. Wu, W. C. Cui, and J. J. Jensen. Review of hydroelasticity theories for global response of marine structures. *Ocean Engineering*, 33(3-4):439–457, 2006.
- [9] Cobouw. Scheveningen krijgt allereerste drijvende offshore zonnecentrale, 2018.
- [10] N. Da Dardagan, A. Br, D. Džigal, and A. Akagic. Multiple Object Trackers in OpenCV: A Benchmark. 2021.
- [11] A. Deduleasa. Introducing the 'Ikea of floating solar power', 2020.
- [12] DNV. Environmental conditions and environmental loads. *DNV*, pages 9–123, 2010.
- [13] DNV. Floating wind: the power to commercialize. *DNV*, 2020.
- [14] DNV GL. CG-0130 Wave loads. Technical report, 2018.
- [15] T. S. Hedges. Regions of validity of analytical wave theories. *Proceedings of the Institution of Civil Engineers: Water, Maritime and Energy*, 112(2):111–114, 1995.
- [16] L. H. Holthuijsen. *Waves in oceanic and coastal waters*. 2007.
- [17] M. G. Hudedmani, V. Soppimath, and C. Jambotkar. A Study of Materials for Solar PV Technology and Challenges. *European Journal of Applied Engineering and Scientific Research*, 5(1):1–13, 2017.
- [18] M. Ikhennicheu, B. Danglade, R. Pascal, V. Arramounet, Q. Trébaol, and F. Gorintin. Analytical method for loads determination on floating solar farms in three typical environments. *Solar Energy*, (June), 2021.
- [19] IMO. Third IMO Greenhouse Gas Study 2014. Technical report, 2015.
- [20] International Energy Agency. World Energy Outlook 2020, 2020.
- [21] J. J. Jensen. Second-order wave kinematics conditional on a given wave crest. *Applied Ocean Research IS*, pages 119–128, 1996.
- [22] J. Journée and W. W. Massie. Nonlinear Behavior. *Offshore Hydromechanics*, (January), 2001.
- [23] M. Kashiwagi. A B-spline Galerkin scheme for calculating the hydroelastic response of a very large floating structure in waves. *Journal of Marine Science and Technology*, 3:37–49, 1998.

- [24] S. Kida, T. Utsunomiya, S. Kida, and T. Utsunomiya. Analysis of the slowly varying drift force on a very large floating structure in multidirectional random seas. *Journal of Marine Science Technology*, 11:229–236, 2006.
- [25] D. C. Lay. *Linear Algebra and Its Applications*. Pearson, international edition, 2012.
- [26] B. Le Mehaute. *An Introduction to Hydrodynamics and Water Waves*. Springer Berlin Heidelberg, 1977.
- [27] B. Liu, D. Fu, Y. Zhang, and X. Chen. Experimental and numerical study on the wave force calculation of a partially immersed horizontal cylindrical float. *International Journal of Naval Architecture and Ocean Engineering*, 12:733–742, 1 2020.
- [28] A. Marchenko and S. Løset. Wave drift force on icebergs - Tank model tests. In *Proceedings of the 20th International Conference on Port and Ocean Engineering under Arctic Conditions*, 2009.
- [29] J. Mégel and J. Kliava. Metacenter and ship stability On the buoyancy force and the metacentre On the buoyancy force and the metacentre On the buoyancy force and the metacentre On the buoyancy force and the metacentre. *American Journal of Physics*, (7):738–747, 2010.
- [30] M. H. Meylan. Wave response of an ice floe of arbitrary geometry. *Journal of Geophysical Research*, 107(C1), 2002.
- [31] E. Monsalve. *Experimental study of water waves: nonlinear effects and absorption*. PhD thesis, 12 2017.
- [32] N. F. Morozov, A. K. Belyaev, P. E. Tovstik, and T. P. Tovstik. Applicability ranges for four approaches to determination of bending stiffness of multilayer plates. *Continuum Mech. Thermodyn*, 33:1659–1673, 2021.
- [33] E. Pesman, D. Bayraktar, and M. Taylan. Influence of damping on the roll motion of ships. 2013.
- [34] A. Philpot. *Mechanics of Materials*. 2011.
- [35] PV Magazine International. Floating solar PV gains global momentum – pv magazine International, 2020.
- [36] V. Roussinova and R. Balachandar. Open channel flow past a train of rib roughness. *Journal of Turbulence*, 12:28, 2011.
- [37] S. Schreier and G. Jacobi. Experimental investigation of wave interaction with a thin floating sheet. In *Proceedings of the International Offshore and Polar Engineering Conference*, volume 2020-October, pages 2479–2488, 2020.
- [38] S. Schreier and G. Jacobi. Experimental investigation of wave interaction with a thin floating sheet. In *Proceedings of the International Offshore and Polar Engineering Conference*, volume 2020-October, pages 2479–2488, 2020.
- [39] M. R. S. Shaikh. A Review Paper on Electricity Generation from Solar Energy. *International Journal for Research in Applied Science and Engineering Technology*, V(IX):1884–1889, 2017.
- [40] A. I. Shirkol and T. Nasar. Coupled boundary element method and finite element method for hydroelastic analysis of floating plate. *Journal of Ocean Engineering and Science*, 3:19–37, 2018.
- [41] H. Suzuki, T. A. Shugar, B. Bhattacharya, H. R. Riggs, H. Seto, D. A. Hudson, M. Fujikubo, Y. Yasuzawa, and H. Shin. Very large floating structures. *Proceedings of the International Conference on Offshore Mechanics and Arctic Engineering - OMAE*, 2(October):597–608, 2007.
- [42] H. Suzuki, K. Yoshida, and K. Iijima. A consideration of the structural design of a large-scale floating structure. *Journal of Marine Science and Technology*, 155(3770):1621, 1996.
- [43] M. Takaki and X. Gu. Motions of a Floating Elastic Plate in Waves. *Journal of The Society of Naval Architects of Japan*, 180, 1996.

- [44] P. E. Tovstik and T. M. Tovstik. Bending stiffness of a multilayered plate. *ECCOMAS Congress 2016 - Proceedings of the 7th European Congress on Computational Methods in Applied Sciences and Engineering*, 2:3423–3435, 2016.
- [45] K. Trapani. *Flexible floating thin film photovoltaic (PV) array concept for marine and lacustrine environments*. PhD thesis, 2014.
- [46] K. Trapani and D. Millar. Hydrodynamic Overview Of Flexible Floating Thin Film PV Arrays. *Conference Paper*, (4):3–6, 2016.
- [47] T. Tsubogo. On the dispersion relation of hydroelastic waves in a plate. *J Mar Sci Technol*, 4:76–83, 1999.
- [48] S. H. M. Van Der Voort. Development of an instrumented mooring system for VFFS model testing Focused on the sensor configuration and calibration procedure. Technical report, 2021.
- [49] E. van Druten and K. Kruit. Perspectieven elektriciteit uit water. Technical report, 2019.
- [50] C. D. Wang and M. H. Meylan. A higher-order-coupled boundary element and finite element method for the wave forcing of a floating elastic plate. *Journal of Fluids and Structures*, 19(4):557–572, 2004.
- [51] E. Watanabe, T. Utsunomiya, and C. M. Wang. Hydroelastic analysis of pontoon-type VLFS: A literature survey. *Engineering Structures*, 26(2):245–256, 2004.



Structural evaluation during transport

First the loading is evaluated and thereafter the resulting stress in the drum and thin sheet are evaluated based on chosen $\varnothing_{drum} = 4.8 \text{ m}$, $t_{drum} = 20 \text{ mm}$ and $B = 30 \text{ m}$. The drum is made of steel with $\rho_{steel} = 7850 \text{ kg/m}^3$ and $E_{steel} = 210 \times 10^9 \text{ N/m}^2$.

A.1. Loading

The drum should bear the mass of the thin sheet including PV foil m_{sheet} and own weight of the drum m_{drum} during transport.

$$m_{drum} = (2\pi \cdot t_{drum}) \cdot \rho_{steel} \cdot B \approx 8.4 \times 10^4 \text{ kg} \quad (\text{A.1})$$

$$m_{sheet} = B \cdot L \cdot h \cdot \rho_{sheet} \approx 9.4 \times 10^4 \text{ kg} \quad (\text{A.2})$$

Both masses are converted into a distributed line load q , assuming m_{drum} and m_{sheet} are equally spread over the drum length B .

$$q = \frac{m_{drum}}{B}g + \frac{m_{sheet}}{B}g \approx 4.2 \times 10^4 \text{ N/m} \quad (\text{A.3})$$

A.2. Stress in the drum

The loading results in bending stress within the drum. The maximum bending stress in the steel drum must not exceed the yield stress of steel $\sigma_{steel,yield} = 235 \text{ N/mm}^2$. The maximum bending moment M_{max} occurs at the midpoint of the drum length at $\frac{1}{2}B = 15 \text{ m}$, resulting in maximum stress at the outermost fiber of the drum at $z = \frac{1}{2}\varnothing$. The moment of inertia around the horizontal axis is perpendicular to the loading I_{yy} for a hollow cylinder and resists the bending moment, where $\varnothing_{drum,in} = \varnothing_{drum} - 2 \cdot t_{drum}$.

$$\sigma_{drum} = \frac{M_{max} \cdot z}{I_{xx}} \approx 27 \text{ N/mm}^2 < \sigma_{steel,yield} \quad (\text{A.4})$$

$$M_{max} = \frac{1}{8}qB^2$$

$$I_{yy} = \pi \left(\frac{\varnothing_{drum}^4 - \varnothing_{drum,in}^4}{64} \right)$$

The bending stress σ_{drum} does not exceed the yield stress and the expected deflection $w_{max} = 5 \text{ mm}$, according to Equation A.5, is negligible (0 %) compared to the structural length of the drum B .

$$w_{max} = \frac{5qB^4}{384E_{steel}I_{yy}} \quad (\text{A.5})$$

Stress in the thin sheet

The drum diameter determines the curvature of the thin sheet during transport. A $\varnothing_{drum} = 4.8$ m results in a bending radius ρ of 2.4 m for the first layer of the spooled thin sheet and increases for the successive layers. The strain ϵ in the thin sheet depends on the curvature and height from the neutral axis z , with $z = 0$ indicating the neutral axis. The total cross sectional height is 261.4 mm and the neutral axis is located at 260.4 mm from the cross section bottom.

$$\epsilon = \frac{z}{\rho} \quad (\text{A.6})$$

$$\sigma = E \cdot \epsilon \quad (\text{A.7})$$

The largest strains occur in the elastomers (neoprene and foam), which can cope well with large strains since the stiffer materials (steel and HyET PV) are exposed to smaller strains, and also have a relatively low yield strength. The layered cross section composition makes optimal use of the material characteristics. The strains are related to stresses using Equation A.7. The occurring stresses within the thin sheet during the maximum curvature are well below the yield stresses as indicated by $\frac{\sigma}{\sigma_{yield}} < 1$ in Table A.1.

		z (mm)	ϵ (-)	σ (N/mm ²)	σ_{yield} (N/mm ²)	$\frac{\sigma}{\sigma_{yield}}$ (-)
PV	<i>PEP</i>	1.0	4.52E-04	0.3	23.0	0.01
	<i>steel</i>	0.8	3.64E-04	76.5	235.0	0.33
	<i>PET</i>	0.8	3.62E-04	1.1	55.0	0.02
Substrate	<i>steel</i>	0.6	2.74E-04	57.6	235.0	0.25
	<i>foam</i>	-255.3	-1.12E-01	0.1	0.7	0.15
Core	<i>neoprene</i>	-259.8	-1.14E-01	0.3	10.0	0.03

Table A.1: Stresses generated in the thin sheet with maximum curvature $\rho = 2.4$ m during transport

A.3. Draft

The draft determines the displaced water volume by the structure. Integrating the hydrostatic pressure around the wetted circumference of the structure results in the buoyancy force $F_{buoyancy}$ and should equal the gravitational force F_g due to m_{drum} . The draft determines the waterplane area A_{wl} of the drum, which is proportional to the stiffness term for the natural heave frequency. Iterations are required to solve Equation A.11 for angle α . Thereafter, A_{wl} is determined with Equation A.9.

$$F_g = \rho_{steel} \cdot B \cdot 2\pi r \cdot t \cdot g \quad (\text{A.8})$$

The horizontal area of the drum is calculated by

$$A_{wl}(\alpha) = \frac{1}{2} r^2 (\alpha - \sin(\alpha)) \cdot B \approx \quad (\text{A.9})$$

$$F_{buoyancy} = A_{wl} \cdot B \cdot \rho_w \cdot g \quad (\text{A.10})$$

$$F_g = F_{buoyancy} \quad (\text{A.11})$$

The draft is calculated using the determined angle α

$$d_{0,drum} = \left(1 \cos\left(\frac{\alpha}{2}\right)\right) \frac{r^2}{2} \approx 1.01 \text{ m} \quad (\text{A.12})$$

A.4. Natural frequencies

The connection center is positioned below the drum center at $z_{connection} = 0.5\phi_{drum}$, resulting in a shift in CoG from the rotational center and $GM = CoG_z$ with $m_{connection} = B \cdot 2 \text{ m} \cdot 0.015 \text{ m} \cdot 7850 \text{ kg/m}^3 \approx 7065 \text{ kg}$. The enclosure of the drum at both sides is schematized as circular disc of 0.02 m steel with $m_{enclosure} = 2841 \text{ kg}$.

$$CoG_z = \frac{z_{connection} \cdot m_{connection}}{m_{connection} + m_{drum} + m_{enclosure}} = 0.23 \text{ m} \quad (\text{A.13})$$

The $I_{yy,connection}$ contribution to the moment of inertia of the connection is neglected due to the small height (thickness plate).

$$I_{yy} = I_{yy,drum} + \sqrt{CoG_z^2} \cdot m_{drum} + z_{connection}^2 \cdot m_{connection} + I_{yy,enclosure} + \sqrt{CoG_z^2} \cdot m_{enclosure} \approx 1.7 \times 10^6 \text{ kgm}^2 \quad (\text{A.14})$$

A.4.1. Heave

The added mass is determined by Equation A.15 [22].

$$a_3 = A_{wl} \cdot \rho_w \approx 8.4 \times 10^4 \text{ kg} \quad (\text{A.15})$$

$$\omega_{0,z_{drum}} = \sqrt{\frac{A_{wl} \rho_w g}{m_{drum} + m_{connection} + m_{enclosure} + a_3}} \approx 2.22 \text{ rad/s} \quad (\text{A.16})$$

A.4.2. Roll

The added moment of inertia δI_{yy} is negligible for a circular shape since the connection will lead to a small contribution in reality.

$$\omega_{0,\phi} = \sqrt{\frac{GM m_{drum} g}{I_{yy} + \delta I_{yy}}} \approx 18.9 \text{ rad/s} \quad (\text{A.17})$$

B

Experimental determination of structural properties

The Center of Gravity and the moment of inertia of the chosen scale model are determined experimentally in all three directions.

B.1. Center of Gravity

The CoG position is determined by balancing the drum on a ruler. The position along the centroidal axis (y) is according to the expectations situated in the middle at $y = \frac{1}{2}B$ since the structure is mirrored along the midplane. CoG_z, CoG_x should be slightly off the center towards the connection. The drum is positioned with the centroidal axis upward and balanced on a ruler with multiple orientations. In case the ruler goes through CoG , equal mass is present on both sides of the ruler and the structure remains upward. In case the ruler does not pass CoG , the structure will fall towards the side of the ruler with the greater mass. The balanced position is iterative determined and a line representing the ruler is drawn. This procedure is repeated for different orientations of the upward drum, and the intersection of the lines indicates the CoG position resulting in $CoG_x = -5.17\text{ mm}$, $CoG_z = -18.15\text{ mm}$ as shown in Figure B.1. Minimal two orientations are required to determine CoG however more orientations are used to reduce the error.

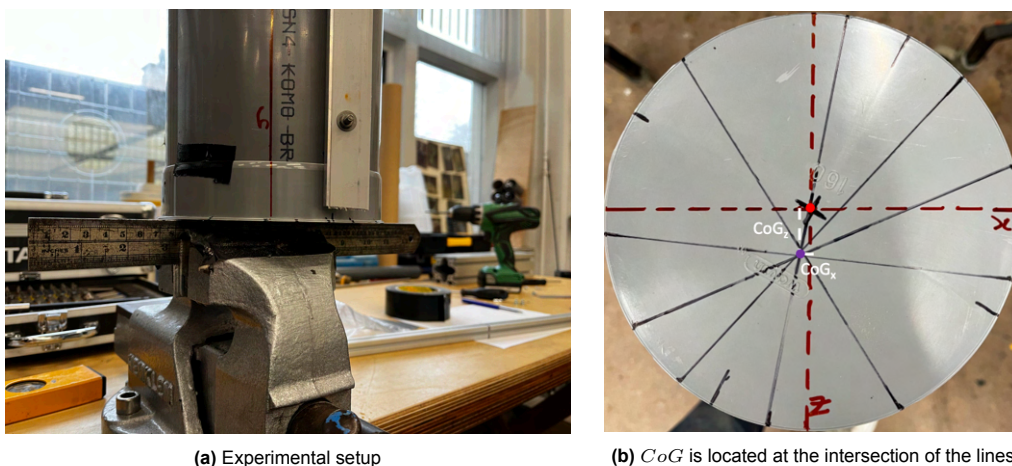


Figure B.1: Experimental determination of $CoG_{x,z}$ position

B.2. Moment of inertia

The experimental setup shown in Figure B.2 is used to determine the moment of inertia I of the scale model (drum with connection). The accuracy of the experimental method is determined with a simple

structure where I is known. Thereafter, I of the complex model scale structure is constructed of several components and is determined with the validated method.

B.2.1. Working principle experimental setup

Two vertical slings with initial length $l_{in} = 2.954$ m are spaced $b = 0.712$ m (m) horizontally from each other. The structure is connected to the slings with CoG positioned in the middle of the two slings at $\frac{1}{2}b$. The structure is rotated with angle θ and thereafter released to start rotating around CoG . The restoring moment is determined by the tension in the lines due to gravity $F_g = m \cdot g$. The equation of motion for the rotation θ at length l is stated in Equation B.1 where l is the actual line length accounted for elongation due to the structural mass.

$$I(l \cdot \ddot{\theta}) = \sum M = \frac{F_g}{2} \cdot \frac{b}{2} + \frac{F_g}{2} \cdot \frac{b}{2} = \frac{F_g}{2} \cdot b \quad (B.1)$$

The rotation has a harmonic form of $\theta = \hat{\theta} \sin(\omega t)$ with $\omega = \frac{2\pi}{T}$ where T represents the natural period in (s).

$$I = \frac{l \cdot b \cdot m \cdot g}{\omega^2} = \frac{l \cdot b \cdot m \cdot g \cdot T^2}{4\pi^2} \quad (B.2)$$

T is obtained during the experiment by averaging the time of 25 oscillations, repeated three times to reduce the error.

Note that the length of the cables is assumed to remain unchanged. This is reasonable since $l = 2.954$ m is relative long compared to the initial horizontal displacement of around 0.10 m leading to $\theta = 0.03^\circ$. This shows a difference in line length of $\cos(\theta) \approx 0.001\%$ in the displaced position which is negligible.

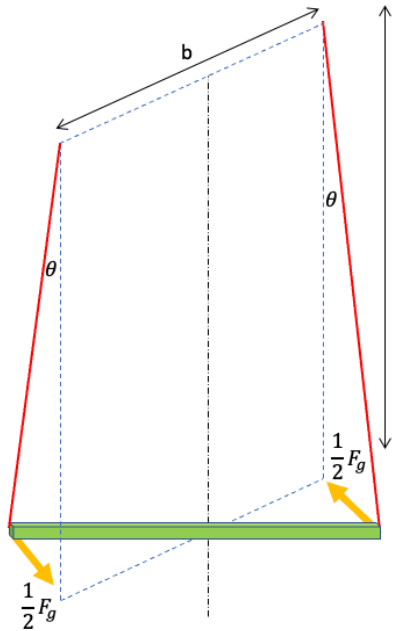


Figure B.2: Working principle of using an experimental setup to determine structural properties

B.2.2. Accuracy method

The accuracy of the method is obtained by comparing the moment of inertia determined theoretically I and experimentally \hat{I} for a simple structure. An I-Beam profile of width 20 mm and length equal to b is chosen, resulting in $m = 0.3364$ kg shown in Figure B.3a. The theoretical approach yields I_{zz} via Equation B.3.

$$I_{zz,Item} = \frac{m}{12}(width^2 + length^2) = \frac{0.3406}{12}(0.020^2 + 0.712^2) \approx 0.01414 \text{ kgm}^2 \quad (\text{B.3})$$

At both ends two bolts are screwed into the Item profile to be able to connect the slings, with $m_{bolt} = 0.0021 \text{ kg}$ and a (Steiner) contribution $I_{zz,bolt} = m_{bolt} \cdot (\frac{1}{2}b)^2 \approx 0.00027 \text{ kgm}^2$.

$$I_{zz,support} = I_{zz,Item} + I_{zz,bolt} \approx 0.01468 \text{ kgm}^2 \quad (\text{B.4})$$

The procedure is repeated six times to determine T and \hat{I}_{zz} with the use of Equation B.2. The results are shown in Table B.1 and the accuracy is within 0.72 %.

	1	2	3	4	5	6
Oscillations	25	30	20	25	25	25
Time (s)	50.44	60.24	40.34	50.18	50.2	50.08
T (s)	2.0176	2.008	2.017	2.0072	2.008	2.0032
\hat{I}_{zz} (kgm ²)	0.01478	0.01464	0.01477	0.01463	0.01464	0.01457
$\frac{\hat{I}_{zz} - I_{zz}}{I_{zz}}$	0.72%	-0.23%	0.66%	-0.31%	-0.23%	-0.71%

Table B.1: Experimental determined \hat{I}_{zz} compared to the theoretical I_{zz}

Combined structures

The described Item profile with width 20 mm is used as supporting structure and another structure is connected to it where the moment of inertia must be determined of $I_{structure}$. The moment of inertia of the supporting structure $I_{zz,support}$, should be subtracted from the total obtained I from the experiment to determine $I_{structure}$.

$$I_{structure} = I - I_{zz,support} \quad (\text{B.5})$$

An Item profile of 80, 80, 400 mm with $m = 5.2114 \text{ kg}$ is chosen as structure, connected horizontally to the supporting Item profile as shown in Figure B.3b. The theoretical approach yields $I_{zz,structure} = 0.04425 \text{ kgm}^2$ according to Equation B.3. The experimental results are shown in Table B.2.

	1	2	3	4	5
Oscillations	30	25	25	25	25
Time (s)	38.7	32.19	32.28	32.04	32.09
T (s)	1.29	1.2876	1.2912	1.2816	1.2836
\hat{I}_{zz} (kgm ²)	0.04389	0.04372	0.04397	0.04332	0.04345
$\frac{\hat{I}_{zz} - I_{zz}}{I_{zz}}$	-0.83%	-1.21%	-0.64%	-2.16%	-1.84%

Table B.2: Experimental determined \hat{I}_{zz} compared to the theoretical I_{zz} for Item profile 80, 80, 400 mm

The same Item profile is connected in the vertical direction to the supporting profile as shown in Figure B.3c to determine \hat{I}_{yy} and compare to $I_{yy} = 0.02199 \text{ kgm}^2$ according to Equation B.3 as shown in Table B.3.

	1	2	3	4	5
Oscillations	50	50	50	50	51
Time (s)	30.35	30.43	30.42	30.48	30.88
T (s)	0.607	0.6086	0.6084	0.6096	0.6054
\hat{I}_{yy} (kgm ²)	0.02211	0.02223	0.02221	0.02230	0.02200
$\frac{\hat{I}_{yy} - I_{yy}}{I_{yy}}$	0.56%	1.08%	1.02%	1.41%	0.07%

Table B.3: Experimental determined \hat{I}_{yy} compared to the theoretical I_{yy} for Item profile 80, 80, 400 mm

Note that the moment of inertia of the structure of interest should be measurable with respect to $I_{zz,support}$. $I_{structure}$ can not be obtained if the magnitude is within the accuracy of the total I (of around 2 %).

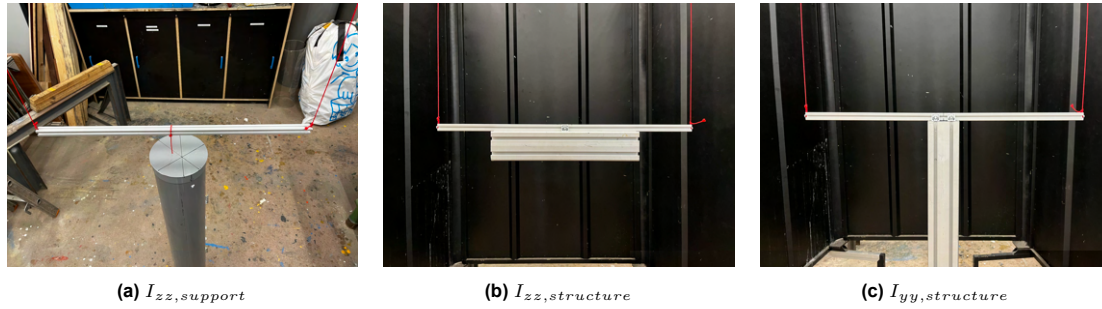


Figure B.3: Visualization of the used structural orientations to determine the accuracy of the experimental method

B.3. Moment of inertia of model scale

The moment of inertia of the model scale concept is experimentally determined with the use of the described experimental method, results are shown in Table B.4. Dummy force transducers (3D printed) are used during the preparation in the workshop and these are replaced by the real force transducers before deploying the model in the tank to prevent overloading the transducers. Three runs per I are performed to be able to spot potential outliers caused by manual errors.

I is in all three directions theoretically determined with software 'Rhino - Rhino 7' (Rhino) as a comparison. First, a technical drawing of the scale model is made including all the different elements. Thereafter, the contribution to I of each element consists of the moment of inertia around $CoG_{element}$ which is indicated by $I_{element}$ where the Steiner term in each direction is proportional to the distance to CoG , squared and the mass for example, as shown in Equation B.6 for the roll moment of inertia I_{yy} . The area moment of inertia determined with 'Rhino' multiplied with the material density ρ results in $I_{element}$. ρ is obtained by measuring the real mass and then dividing by the volume determined with 'Rhino'. The sum of all contributions results in the total moment of inertia which is compared to the experimental determined \hat{I} in Table B.4. The theoretical approach is in all cases bigger than the experimental determination with a maximum deviation of -3.6% . However, in this study a 2D-case is assessed implying the roll moment of inertia is the most important which shows a maximum deviation of -0.59% .

$$I_{yy} = I_{yy,element} + m_{item} \cdot (\sqrt{(z - CoG_z)^2 + (x - CoG_x)^2})^2 \quad (B.6)$$

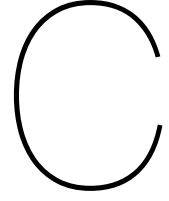
	I_{zz}			I_{xx}			I_{yy}		
	1	2	3	1	2	3	1	2	3
Oscillations	25	25	25	25	24	25	50	50	50
Time (s)	70.96	71.06	70.84	70.54	68.07	70.59	40.79	40.86	40.81
T (s)	2.8384	2.8424	2.8336	2.8216	2.83625	2.8236	0.8158	0.8172	0.8162
\hat{I} (kg mm ²)	3.95E+05	3.96E+05	3.94E+05	3.90E+05	3.94E+05	3.91E+05	2.18E+04	2.20E+04	2.19E+04
$\frac{\hat{I}-I}{\hat{I}}$	-2.56%	-2.27%	-2.90%	-3.75%	-2.68%	-3.60%	-0.59%	-0.02%	-0.43%

Table B.4: Experimental determination of I in all three directions and compared to the theoretical calculation.

The real force transducers are made of aluminium ($m = 19.1$ g) instead of plastic ($m = 8.9$ g). The influence on I should be assessed. The location of the force transducers F is described by coordinates $x = 21.3$ mm, $z = -87.5$ mm, $y = 250$ mm with respect to the drum center. The contribution to I for both the dummy and real force transducers is calculated using the approach described by Equation B.6. I increases slightly in all three directions as shown in Table B.5. Note that these experimental determined I are obtained with an accuracy of 2 %.

	Force transducer		Total (kg mm ²)	ΔI (%)
	Plastic (kg mm ²)	Aluminium (kg mm ²)		
I_{zz}	1.52E+03	3.26E+03	3.97E+05	0.44
I_{xx}	1.65E+03	3.53E+03	3.94E+05	0.48
I_{yy}	1.45E+02	3.11E+02	2.21E+04	0.76

Table B.5: Influence of real force transducers vs used dummies on I



Calibration sensors

C.1. 3D-sensor

The mooring force sensor consists of three orthogonal placed load sensors, similar to the ones used for the connection force ZEMIC 1R1-K with 20N capacity (linearly dependent and sensitive in one direction). This implies that the combination of output voltages of the three sensors represents the loading in a certain direction. The orientation (angle) of the 3D-frame influences the correlation between the sensors. The sensor is calibrated in a fixed orientation, changing the orientation will change the dependencies of each sensor and requires a new calibration. The applied load can be decomposed into force contributions in the chosen (orthogonal) coordinate system. The voltage output of the three sensors (1, 2, 3) depends on the force contribution in the three directions ($i = x, y, z$) indicated by β_1 and the nondependent offset β_0 .

$$\begin{aligned} U_1 &= F_z\beta_{z,1} + F_y\beta_{y,1} + F_x\beta_{x,1} + \beta_{0,1} \\ U_2 &= F_z\beta_{z,2} + F_y\beta_{y,2} + F_x\beta_{x,2} + \beta_{0,2} \\ U_3 &= F_z\beta_{z,3} + F_y\beta_{y,3} + F_x\beta_{x,3} + \beta_{0,3} \end{aligned}$$

Multiple measurements n can be represented in matrix notation where $Y_i = y_{i,1}, y_{i,2}, y_{i,3}$ represents the measured voltages in (V), and $X_i = x_{i,1}, x_{i,2}, x_{i,3}$ represents the applied force (N), β_1 represents the slope regression parameters and β_0 represent the offset for each sensor.

$$\begin{bmatrix} y_{1,1} & y_{1,2} & y_{1,3} \\ y_{2,1} & y_{2,2} & y_{2,3} \\ \vdots & \vdots & \vdots \\ y_{n,1} & y_{n,2} & y_{n,3} \end{bmatrix} = \begin{bmatrix} x_{1,1} & x_{1,2} & x_{1,3} \\ x_{2,1} & x_{2,2} & x_{2,3} \\ \vdots & \vdots & \vdots \\ x_{n,1} & x_{n,2} & x_{n,3} \end{bmatrix} \cdot \begin{pmatrix} \beta_{1,1} & \beta_{1,2} & \beta_{1,3} \\ \beta_{2,1} & \beta_{2,2} & \beta_{2,3} \\ \beta_{3,1} & \beta_{3,2} & \beta_{3,3} \end{pmatrix} + \begin{bmatrix} \beta_{0,0} & \beta_{0,1} & \beta_{0,3} \\ \beta_{0,0} & \beta_{0,1} & \beta_{0,3} \\ \vdots & \vdots & \vdots \\ \beta_{0,0} & \beta_{0,1} & \beta_{0,3} \end{bmatrix} \quad (\text{C.1})$$

A calibration procedure is performed with n load combinations and split over the three-axis to obtain the corresponding output voltages. With the use of multivariate linear regression, the sensitivity of the load sensors is represented in β_1 and β_0 [25]. There are two problems with solving Equation C.1 as stated, since matrix X is not squared and the offset β_0 should be removed from the equation. The latter is obtained by centering both the measured forces and voltages by subtracting the mean value indicated by a bar where β_0 is obtained by solving $Y - \bar{Y} = (X - \bar{X})\beta_1$.

$$\begin{bmatrix} y_{1,1} - \bar{y}_1 & y_{1,2} - \bar{y}_2 & y_{1,3} - \bar{y}_3 \\ y_{2,1} - \bar{y}_1 & y_{2,2} - \bar{y}_2 & y_{2,3} - \bar{y}_3 \\ \vdots & \vdots & \vdots \\ y_{n,1} - \bar{y}_1 & y_{n,2} - \bar{y}_2 & y_{n,3} - \bar{y}_3 \end{bmatrix} = \begin{bmatrix} x_{1,1} - \bar{x}_1 & x_{1,2} - \bar{x}_2 & x_{1,3} - \bar{x}_3 \\ x_{2,1} - \bar{x}_1 & x_{2,2} - \bar{x}_2 & x_{2,3} - \bar{x}_3 \\ \vdots & \vdots & \vdots \\ x_{n,1} - \bar{x}_1 & x_{n,2} - \bar{x}_2 & x_{n,3} - \bar{x}_3 \end{bmatrix} \cdot \begin{pmatrix} \beta_{1,1} & \beta_{1,2} & \beta_{1,3} \\ \beta_{2,1} & \beta_{2,2} & \beta_{2,3} \\ \beta_{3,1} & \beta_{3,2} & \beta_{3,3} \end{pmatrix} \quad (\text{C.2})$$

The equation is still not solvable due to the nonsquare matrix X , which is solved by multiplying both sides of the equation with the transposed matrix X' . The least-squares method is used for the

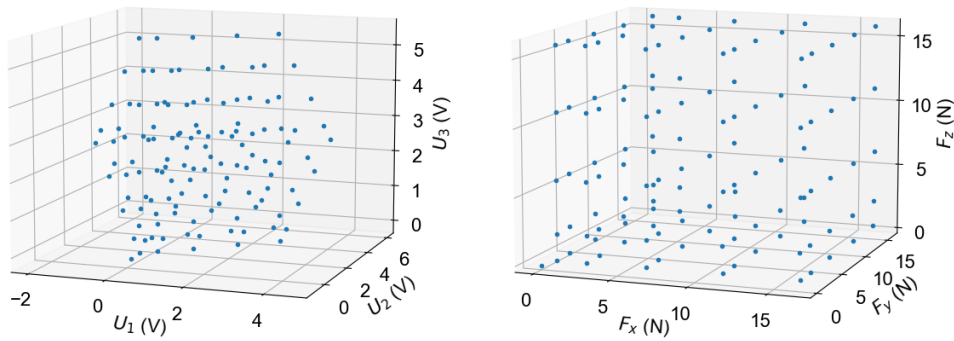


Figure C.1: Measured voltages (left) and corresponding forces (right) in 3D

regression based on the principle of minimizing the sum of the squared residuals where residuals ϵ are calculated as $\epsilon = \mathbf{Y} - \mathbf{X}\beta_1$.

$$\sum \epsilon_i^2 = [\epsilon_1, \epsilon_2 \dots \epsilon_n] \cdot \begin{bmatrix} \epsilon_1 \\ \epsilon_2 \\ \vdots \\ \epsilon_n \end{bmatrix} = \epsilon' \epsilon \quad (\text{C.3})$$

The squared residuals will be minimized if $\frac{\delta}{\delta \beta} (\mathbf{Y} - \mathbf{X}\beta_1)' (\mathbf{Y} - \mathbf{X}\beta_1) = 0$. This leads to the following equation [2]:

$$\mathbf{X}'\mathbf{Y} = \mathbf{X}'\mathbf{X}\beta_1 \quad (\text{C.4})$$

$$\beta_1 = (\mathbf{X}\mathbf{X}')^{-1} \mathbf{X}'\mathbf{Y} \quad (\text{C.5})$$

β_0 is obtained by performing the following procedure with the determined β_1 :

$$\beta_0 = \bar{Y} - \bar{X}\beta_1 \quad (\text{C.6})$$

This calibration translates a known force into a set of predicted voltages of the three sensors and has unity (V/N). The opposite relation (N/V) is required to evaluate the experiment since the voltages of the sensors are measured while the corresponding forces have to be calculated. The required procedure is illustrated for inverting the equation for a single variable linear regression:

$$\begin{aligned} y &= x\beta_1 + \beta_0 \\ x &= \frac{y}{\beta_1} - \frac{\beta_0}{\beta_1} \\ x &= yB_1 + B_0 \end{aligned}$$

For the multivariate case, B_1 is the inverse of β_1 and B_0 is obtained by multiplying β_0 with the inverse of β_1 :

$$B_0 = \beta_0 \beta_1^{-1} \quad (\text{C.7})$$

$$B_1 = \beta_1^{-1} \quad (\text{C.8})$$

Translating the measured voltages U in (V) of the three sensors into forces into the three orthogonal axes $F_{z,y,z}$ in (N) requires the following procedure.

$$[F_z \ F_y \ F_x] = [U_1 \ U_2 \ U_3] \begin{pmatrix} \beta_{1,1} & \beta_{1,2} & \beta_{1,3} \\ \beta_{2,1} & \beta_{2,2} & \beta_{2,3} \\ \beta_{3,1} & \beta_{3,2} & \beta_{3,3} \end{pmatrix}^{-1} + (\beta_{0,0} \ \beta_{0,1} \ \beta_{0,3}) \begin{pmatrix} \beta_{1,1} & \beta_{1,2} & \beta_{1,3} \\ \beta_{2,1} & \beta_{2,2} & \beta_{2,3} \\ \beta_{3,1} & \beta_{3,2} & \beta_{3,3} \end{pmatrix}^{-1} \quad (\text{C.9})$$

C.1.1. Calibration setup

It is important to be sure to apply loads in the three orthogonal directions. The z -axis is always straight due to gravity and the lengths L_{axis} of the x - and y -axis are as long as the carriage car allows, to minimize the error. A frame is constructed to be able to adjust the position of the pulleys both vertically and horizontally. Large pulleys are used to minimize the rotational resistance which is recommended by Van der Voort in [48].

First, a reference line at equal vertical height along the carriage car is drawn by using a laser level. To get the z -axis perpendicular to the other two axes, the vertical height of x - and y - is aligned with the vertical height of the orange line-connector of the 3D-sensor. Orthogonality of the x - and y - axis is obtained if Pythagoras stated in Equation C.10 is satisfied. The x, y -pulleys are shifted horizontally until all three lengths meet the condition which requires $L_{xz} = 554.6$ mm and $L_{yz} = 205.2$ mm. The lengths are determined using a tape measure where an accuracy of 1 mm is reasonable, resulting in an error in angle of $90^\circ - \arccos(\frac{1\text{mm}}{L_{axis}})$. The maximum error of 0.03° occurs along the y - axis due to the smallest length and therefore the axis can be assumed to be orthogonal in the developed setup.

$$L_{xy}^2 = L_{yz}^2 + L_{xz}^2 \quad (\text{C.10})$$

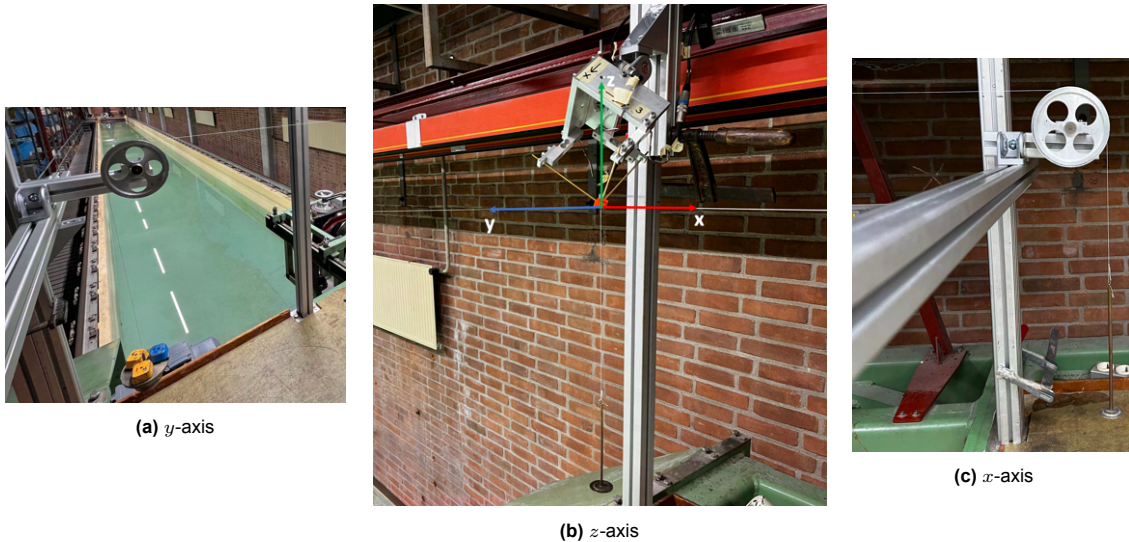


Figure C.2: Overview of the calibration setup for the 3D-sensor

C.1.2. Calibration procedure

Loads are applied in three orthogonal directions and step-wise increased along each axis as shown in Table C.1. Five steps in each direction come down to $n = 5 \cdot 5 \cdot 5 = 125$ unique combinations of applied forces plus one zero-measurement without any load before the start. Loads are applied by staggung disks with a known mass onto the 'table' at each axis. A run is started with a certain load combination at the x - and y - axis and the five load steps for the z -axis are measured during the run. An interval of 30 s is used before additional loading for the next step is added, and the used output voltage is averaged over the stable interval of 15 s. The performed calibration results in B_0 stated in Matrix C.11 and B_1 stated in Matrix C.12.

step	F_z (N)	F_y (N)	F_x (N)
1	-0.30	0.49	0.83
2	-1.96	1.96	1.96
3	-5.89	5.89	5.89
4	-10.79	10.79	10.79
5	-15.57	15.57	15.57

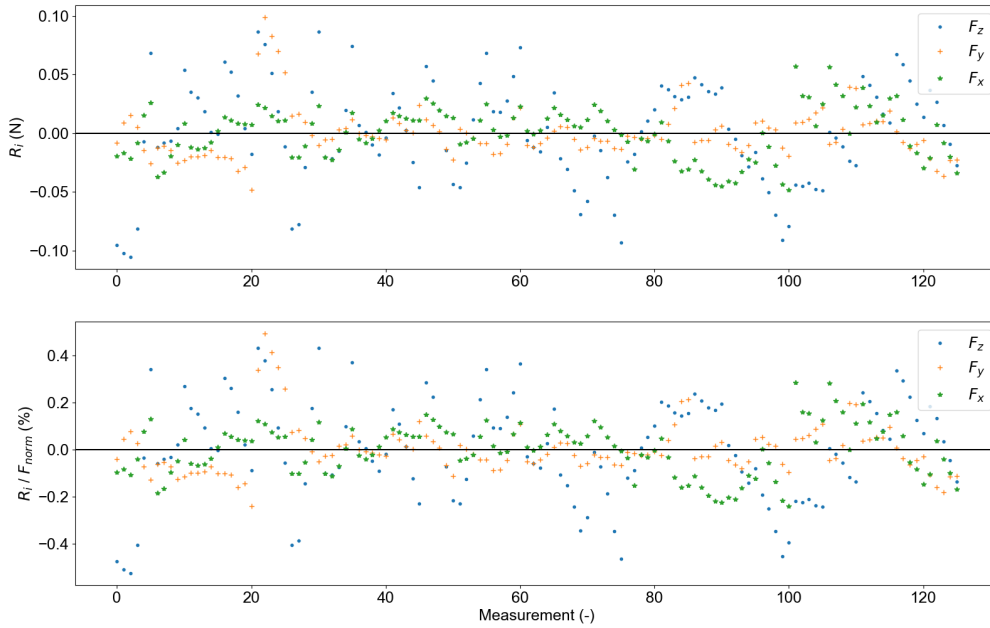
Table C.1: Applied loads in each direction

$$\mathbf{B}_0 = \begin{pmatrix} -0.8174 & 1.6879 & -1.2349 \end{pmatrix} \quad (\text{C.11})$$

$$\mathbf{B}_1 = \begin{pmatrix} 2.4382 & 2.9596 & -0.1637 \\ 2.0912 & -1.4830 & 2.5995 \\ -2.3374 & 1.8679 & 2.7536 \end{pmatrix} \quad (\text{C.12})$$

C.1.3. Accuracy

The accuracy is estimated by determining the absolute residuals based on the difference in predicted force in the three directions with the known applied forces, for instance, the absolute residual in x -direction is calculated using $R_{i,x} = \hat{F}_{i,x} - F_{i,x}$. The normalized residuals are obtained by dividing by the maximum load capacity of each sensor 20 N, resulting in an accuracy of $\pm 0.56\%$.

Figure C.3: The absolute (top) and normalized (bottom) residuals of each measurement i during the calibration procedure

The stated residuals are split into the three directions in Figure C.3. However, the residuals of these three force contributions are the actual measured force in the mooring line. The accuracy of this force is obtained by taking the square root of the sum of the squared absolute residuals of each direction.

$$R_i = \sqrt{R_{i,x}^2 + R_{i,y}^2 + R_{i,z}^2} \quad (\text{C.13})$$

The Euclidean distance R_i is an indication of the residual of the total force, which is normalized by division with the maximum theoretical line force of the combined identical sensors F_{norm} where $F_{i,max}$ represents the maximum capacity of one sensor 20 N.

$$F_{norm} = \sqrt{\sum_{n=1}^3 F_{i,max}} \quad (C.14)$$

The maximum normalized residual R_i is 0.36 % and plotted in Figure C.4 which is used as the error range for the interpretation of the calculated forces with the 3D sensor.

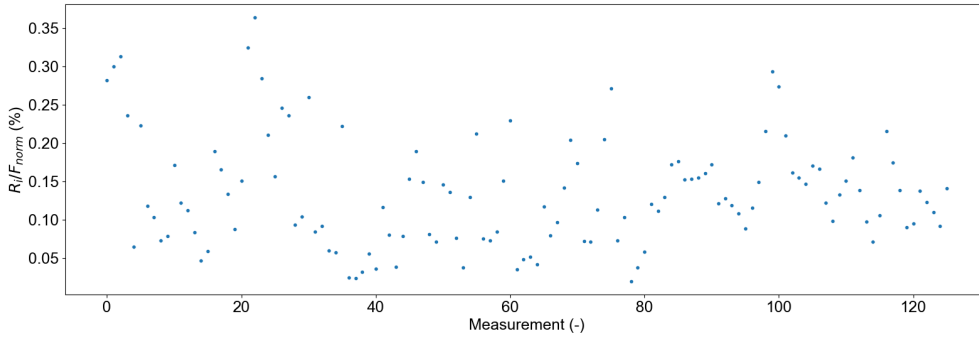


Figure C.4: The normalized residuals of the line force based on the Euclidean distance with respect to the maximum theoretical force F_{norm}

C.2. Connection force

The connection force is measured with load sensor ZEMIC 1R1-K with 20 N capacity, similar to the ones used in the 3D-sensor. The force transducers are designed to be sensitive in one direction, by making use of the principle of the bridge of Wheatstone. The force transducers have a linear relation between the output voltage and applied load,

$$y = \beta_1 \cdot x + \beta_0 \quad (C.15)$$

where y represents the measured voltage (V), x represents the applied force (N), β_1 represents the slope (V/N) and β_0 represents the intercept at $x = 0$ (V). To obtain the calibration factor β_1 in (N/V), the equation is inverted, no centering is required as used in the calibration for the 3D-sensor since β_0 is a square matrix (1x1) in this case.

$$x = \frac{y}{\beta_1} - \frac{\beta_0}{\beta_1} \quad (C.16)$$

Linear regression is used to determine the calibration matrix β of the force transducer by calculating the intercept $\frac{\beta_0}{\beta_1}$ and slope β_1 based on n measurements.

$$\begin{pmatrix} x_1 \\ x_2 \\ \vdots \\ x_n \end{pmatrix} = \begin{bmatrix} 1 & y_1 \\ 1 & y_2 \\ \vdots & \vdots \\ 1 & y_n \end{bmatrix} \cdot \begin{pmatrix} -\frac{\beta_0}{\beta_1} \\ \frac{1}{\beta_1} \end{pmatrix} ; \quad \mathbf{X} = \mathbf{Y} \cdot \beta$$

The regression parameter β is approximated by performing a similar procedure as described in Matrix C.1 based on minimizing the squared residuals.

$$\hat{\beta} = (\mathbf{Y}'\mathbf{Y})^{-1}\mathbf{Y}'\mathbf{X} \quad (C.17)$$

C.2.1. Calibration setup

The force transducers are screwed to a rigid frame, leveled, and clamped to a table. A line attached to a screw is connected to the force transducer. A 'table' of 0.055 kg is connected to the line to be able to apply loads to the sensor. The line may be a few degrees off with respect to the vertical axis of the force transducer, resulting in a negligible cosine error ($2^\circ \approx 0.25\%$).

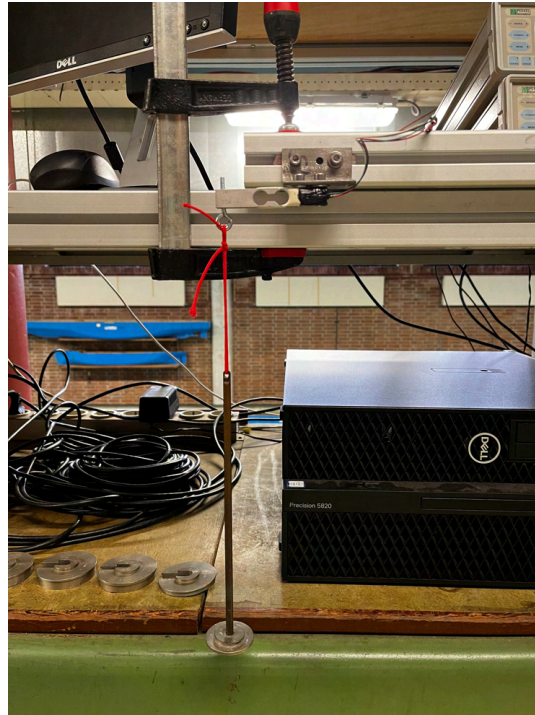


Figure C.5: Visualization of the used calibration setup of the force transducer

During the calibration procedure, a known load F is applied, step-wise increased to the maximum load capacity 20 N and in similar steps decreased to zero again. The calibration is performed in the positive and negative directions of the sensor to validate the sensitivity in both directions.

C.2.2. Accuracy

The normalized residuals R_{norm} are determined by dividing the absolute residuals $R = \hat{F} - F$ by the maximum capacity 20 N. All four fitted regressions have a correlation value $R = 1$ indicating an accurate regression with maximum deviations of 0.02 % for both sensors as shown in Figure C.6 and C.7. Force transducer F_{right} does not show any hysteresis since the residuals almost overlay each other for calibration in the positive and negative directions. Some hysteresis is visible for F_{left} , since R_{norm} shows a maximum gap of 0.025 % between the positive and negative residuals at the same step. Hence, the forces measured with the two load sensors should be obtained with an accuracy of 0.025 %. This is in line with the accuracy stated by the manufacturer of 0.03 %.

step	Positive					Negative					
	F (N)	U (V)	\hat{F} (N)	R (-)	R_{norm} (%)	F (N)	U (V)	\hat{F} (N)	R (-)	R_{norm} (%)	
1	0,53	0,00	0,53	-0,002	-0,009	-0,53	0,00	-0,53	0,000	0,000	
2	1,51	-0,29	1,51	-0,001	-0,006	-1,51	0,29	-1,51	0,001	0,005	
3	3,47	-0,87	3,47	0,001	0,003	-3,47	0,87	-3,47	0,001	0,004	
4	5,44	-1,46	5,44	0,002	0,008	-5,44	1,46	-5,43	0,001	0,007	
5	7,40	-2,04	7,40	0,002	0,011	-7,40	2,04	-7,40	-0,001	-0,004	
6	11,32	-3,20	11,32	0,002	0,008	-11,32	3,21	-11,32	0,001	0,003	
7	15,25	-4,37	15,25	0,001	0,004	-15,25	4,37	-15,25	-0,001	-0,005	
8	20,15	-5,82	20,15	-0,005	-0,025	-20,15	5,83	-20,15	0,001	0,006	
9	15,25	-4,37	15,25	0,001	0,007	-15,25	4,37	-15,25	0,000	0,000	
10	11,32	-3,20	11,32	0,002	0,009	-11,32	3,21	-11,32	-0,002	-0,009	
11	7,40	-2,04	7,40	0,001	0,005	-7,40	2,04	-7,40	0,000	-0,001	
12	5,44	-1,46	5,44	0,000	0,001	-5,44	1,46	-5,44	0,000	0,002	
13	3,47	-0,87	3,47	0,000	0,002	-3,47	0,87	-3,47	0,000	0,001	
14	1,51	-0,29	1,51	-0,002	-0,008	-1,51	0,29	-1,51	-0,001	-0,005	
15	0,53	0,00	0,53	-0,002	-0,010	-0,53	0,00	-0,53	-0,001	-0,004	
	<i>Slope (N/V)</i> <i>Intercept (N)</i>		-3,371 0,528				<i>Slope (N/V)</i> <i>Intercept (N)</i>		-3,366 -0,530		

Table C.2: Overview of the applied loads F during the calibration of the force transducer F_{right} and the approximated values \hat{F} using the determined slope and intercept

step	Positive					Negative					
	F (N)	U (V)	\hat{F} (N)	R (-)	R_{norm} (%)	F (N)	U (V)	\hat{F} (N)	R (-)	R_{norm} (%)	
1	0,53	0,00	0,53	-0,002	-0,0103	-0,53	0,00	-0,53	-0,002	-0,01	
2	1,51	-0,30	1,51	-0,002	-0,0082	-1,51	0,30	-1,51	-0,002	-0,01	
3	3,47	-0,89	3,47	0,000	-0,0012	-3,47	0,89	-3,48	-0,003	-0,02	
4	5,44	-1,48	5,44	0,001	0,0038	-5,44	1,48	-5,44	-0,003	-0,02	
5	7,40	-2,07	7,40	0,002	0,0092	-7,40	2,07	-7,40	-0,003	-0,01	
6	11,32	-3,25	11,33	0,002	0,0116	-11,32	3,25	-11,33	-0,003	-0,01	
7	15,25	-4,44	15,25	0,002	0,0078	-15,25	4,44	-15,25	-0,002	-0,01	
8	20,15	-5,91	20,15	-0,004	-0,0212	-20,15	5,92	-20,15	0,003	0,02	
9	15,25	-4,43	15,25	0,000	0,0021	-15,25	4,44	-15,25	0,000	0,00	
10	11,32	-3,25	11,32	0,001	0,0040	-11,32	3,25	-11,32	0,001	0,00	
11	7,40	-2,07	7,40	0,001	0,0028	-7,40	2,07	-7,40	0,002	0,01	
12	5,44	-1,48	5,44	0,000	0,0023	-5,44	1,48	-5,43	0,003	0,01	
13	3,47	-0,89	3,47	0,000	0,0013	-3,47	0,89	-3,47	0,003	0,01	
14	1,51	-0,30	1,51	-0,001	-0,0028	-1,51	0,29	-1,51	0,004	0,02	
15	0,53	0,00	0,53	0,000	-0,0013	-0,53	0,00	-0,53	0,004	0,02	
	<i>Slope (N/V)</i> <i>Intercept (N)</i>		-3,319 0,528				<i>Slope (N/V)</i> <i>Intercept (N)</i>		-3,316 -0,532		

Table C.3: Overview of the applied loads F during the calibration of the force transducer F_{left} and the approximated values \hat{F} using the determined slope and intercept

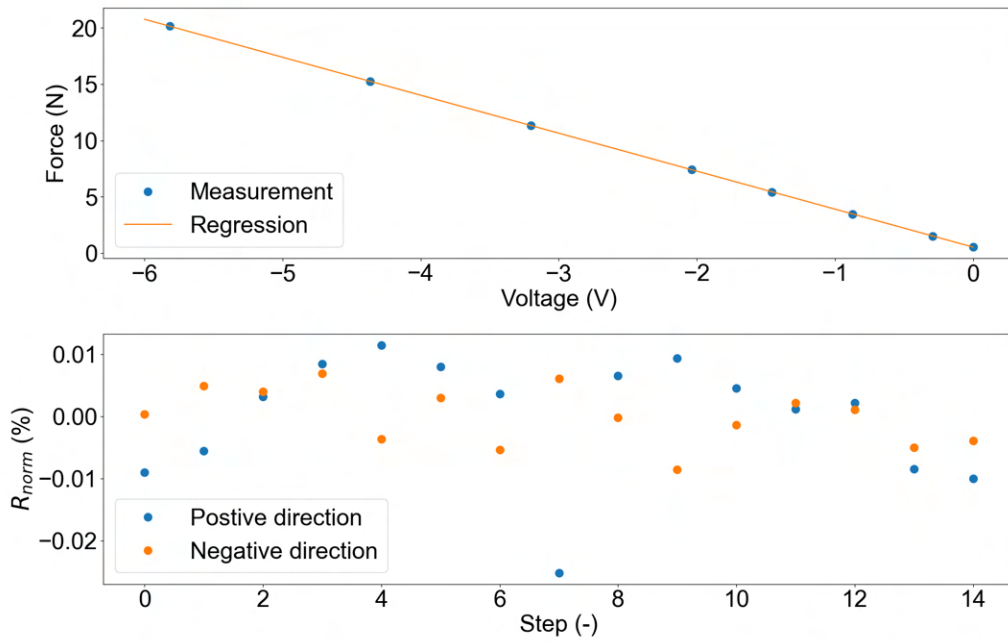


Figure C.6: The top figure shows the measurements and the approximated relation using regression in the positive direction of force transducer F_{right} . The bottom figure shows the normalized residuals R_{norm} for the calibration in the positive and negative directions.

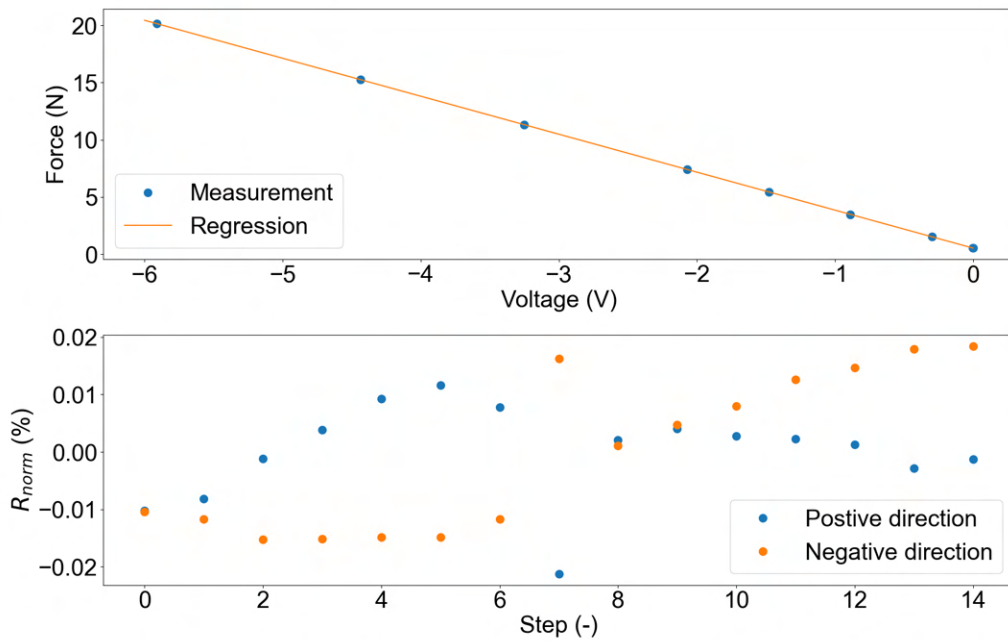


Figure C.7: The top figure shows the measurements and the approximated relation using regression in the positive direction of force transducer F_{left} . The bottom figure shows the normalized residuals R_{norm} for the calibration in the positive and negative directions.